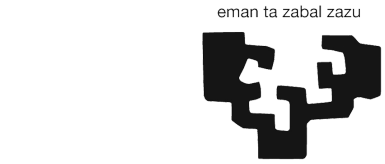

Topological Materials From a Symmetry Perspective

A thesis submitted to the
University of the Basque Country
by

Iñigo Robredo Magro

Supervised by

Prof. Maia G. Vergniory
Prof. Aitor Bergara

October 2021

Contents

Introduction **2**

1 Fundamentals of Topological Band Theory **7**
1.1 Fundamentals of Electronic Band Theory 7
1.2 Periodic Crystal Potential and Bloch theorem 9
1.2.1 Crystal lattice: Real and Reciprocal Spaces 9
1.2.2 Bloch Theorem 10
1.3 Computing Methods 13
1.3.1 Density Functional Theory 13
1.3.2 Tight Binding 15
1.4 Wannier functions 16
1.5 Topology: Zak phase, Chern number and Wilson loop 18
1.6 Su-Schrieffer-Heeger model 22

2 Topological Quantum Chemistry **26**
2.1 Hexagonal lattice 28
2.1.1 Orbits for the different q points 31
2.1.2 Adding orbitals 33
2.2 Adding p orbitals at 2b positions 34
2.2.1 Spinless p orbitals 34
2.2.2 Spinful p orbitals 36
2.3 Inducing a Band Representation 37
2.4 Little groups at **k**-points in the first BZ 38
2.5 Example of band representation 39
2.5.1 Spinful graphene 40
2.5.2 Spinless graphene 43
2.6 Subducing the Band Representation 44
2.6.1 Γ point 44
2.6.2 K point 45
2.6.3 M point 46

2.6.4 High-symmetry lines . . . 46
2.7 Conclusions . . . 48

3 Mirror Chern insulator PbTe **49**
3.1 Symmetry Indicators . . . 49
3.2 Effective Tight Binding model . . . 50
3.3 Topological properties . . . 54
3.4 Ab initio results . . . 57
3.5 Conclusions . . . 60

4 Time Reversal symmetry breaking: CoS_2 **62**
4.1 Introduction . . . 62
4.2 Topological properties of Weyl nodes and Nodal lines . . . 64
4.3 Crystal and electronic structures . . . 66
4.3.1 Symmetries and structure . . . 66
4.3.2 Electronic structures . . . 66
4.4 Effective 4-fold $\mathbf{k} \cdot \mathbf{p}$ model . . . 67
4.5 Topological analysis: Nodal lines and Weyl nodes . . . 69
4.6 Experimental results . . . 73
4.7 Conclusions . . . 77

5 Breaking symmetries with strain: Hall viscosity **79**
5.1 Introduction . . . 79
5.2 Properties of Point Group 23 . . . 81
5.3 Threefold $\mathbf{k} \cdot \mathbf{p}$ model from Group Theory . . . 84
5.4 $k \cdot p$ Hamiltonian: First Order Approximation . . . 85
5.5 Hall viscosity with cubic symmetry . . . 86
5.6 Tight Binding model . . . 88
5.6.1 Symmetry . . . 90
5.6.2 Threefold at the Γ point: energies and states . . . 91
5.7 Stress Response . . . 92
5.7.1 Phonon Stress Tensor . . . 93
5.7.2 Momentum Continuity Stress Tensor . . . 95
5.8 Hall Viscosity . . . 97
5.8.1 PHV and MHV . . . 97
5.8.2 Lattice Viscosity . . . 99
5.9 Conclusions . . . 100

6 Concluding thoughts **102**

Acknowledgements

List of Publications

A Definitions

B Proof that the site symmetry groups for the 3c Wyckoff positions are isomorphic to C_{3v}

B.1 Site-symmetry group of $q = \left(\frac{1}{3}, \frac{1}{3}\right)$ . . . . . .

B.2 Site-symmetry group of positions in the same orbit . . . . . .

C Wannier function transformation properties

D Elementary Band Representation

List of Figures

Bibliography

Introduction

One of the main aims of condensed matter physics is the description of different phases of matter. During the 1930s, Landau developed a successful theory that explained phase transitions in terms of symmetry breaking [1]. Within his framework, phase transitions can be monitored by an order parameter which acquires an expectation value that breaks some symmetry and distinguishes both phases. Taking a ferromagnet as an example, a non-zero value of magnetization implies that there is a preferred direction in space, thus, breaking full spin rotation SU(2) symmetry. The only setback of the theory is that it only distinguishes phases of matter in terms of symmetry breaking; it is thus blind to different phases of matter that preserve the same symmetries.

However, in the decade of 1980, Von Klitzing's work on the 2D electron gas under large magnetic fields defied the Landau theory [2]. He discovered those systems displayed plateaus of quantized Hall resistance in units of h/e^2 as a function of the applied magnetic field. The system, however, did not go through a phase transition as described by Landau theory, so a new framework had to be developed. In 1982, Thouless *et al* derived a Kubo formula for the Hall conductivity in a 2D electron gas [3]. They related the Hall conductivity to a change in phase of the wavefunctions in a loop around the BZ. Due to gauge symmetry, the change in phase has to be of the form $2\pi C$, with C an integer number, named Chern number, a topological quantity. They also proved that this number could not change unless gaps are closed, thus explaining the robustness of the plateaus in von Kitzing's experiment.

The field of topological insulators (TI) took off when Haldane realized that the QHE in a 2D electron gas under high magnetic fields could arise on lattice systems in the absence of an external magnetic field [4]. Based on a simple hexagonal lattice system with first nearest neighbors hopping, he added a time reversal symmetry (TRS) breaking, second nearest-negihbors complex hopping that drives the system from having Chern number 0 to Chern number 1. This model is a lattice realization of the QHE, with C boundary modes (edge states) that are protected against backscattering due to the chiral nature of the states (they are forced to move on a definite direction in the edge).

Based on this model, Kane and Mele [5] derived a TRS-preserving model by coupling two copies of the topological Haldane model in each spin sector with opposite Chern numbers. Because TRS prevents TRS-related partners to mix, their model realized a spin Chern insulator, in the boundary of which TRS-related partners would propagate as do electrons in the QHE. Thus, they named this effect as quantum spin Hall effect (QSHE). The main advantage of this model is that the hopping driving the topological transition can be assigned to a physical effect, the spin-orbit coupling (SOC). This model, though, cannot have indefinitely many edge states. Due to TRS, there cannot be a net current; states have to move on opposing directions in the boundary. States with opppsite spin polarization have opposite Chern numbers, so there will be a net spin current, and states with different spin polarizations cannot backscatter. However, if we add an extra edge state (one of each spin polarization, so as not to break TRS), states that have the same polarization can scatter between themselves and open a gap in the surface. This is why the topological classification of the Kane-Mele model is twofold; it can either be topologically trivial (even number of edge states) or topologically non-trivial (odd number of edge states. This can be encoded in a new topological invariant, the $\nu_{\mathbb{Z}_2} = 0$ invariant, which represents the parity of the number of edge states. Later on, Fu and Kane [6] developed a method for computing this topological invariant by means of the Pfaffian[1].

In 2007, Fu and Kane [7] proved that the topological properties observed in 2D systems could be promoted to 3D. Analogous to 2D TIs that have gapped bulk and conducting edge states, they found a type of 3D insulators that have conduction states in the 2D boundary. Similarly to the results in 2D QSHE, 3D TIs' surface states are robust and protected against backscattering by TRS. However, these states live on a much larger surface, making them good conductors that could be exploited for electronic applications [8]. Moreover, since the desired electronic properties are linked to a topological invariant, they will be robust against (a certain amount of) disorder, such as doping or temperature.

The computation of the topological invariants by means of the Pfaffian proved to be hard in general, since it is necessary to have a smooth continuous gauge in the whole BZ. However, in the presence of inversion symmetry, they were able to map the topological invariant to the inversion symmetry eigenvalues. For the particular case of a 3D TI, it is sufficient to compute the inversion symmetry eigenvalues of the filled bands. If there is an odd number of bands with eigenvalue -1, then the bands have an odd (non-trivial) $\mathbb{Z}_2$ topological invariant.

Apart from being useful to diagnose, crystal symmetries can also create (and protect) different topological phases of matter. This work was started by Fu in 2011 [9]. He extended the notion of TIs to topological crystalline insulators (TCIs),

[1]Defining $w_{mn}(\mathbf{k}) = \langle u_{m,-\mathbf{k}} | \, \Theta \, | u_{n,\mathbf{k}} \rangle$, the topological invariant is defined as $\delta_i = \frac{\sqrt{\det(w(\Gamma_i)}}{\mathrm{Pf}(w(\Gamma_i))}$

systems in which crystalline symmetries stabilize topology. These systems would be rendered trivial without the protection of crystal symmetries, thus, topological surface states can only exist in facets where the symmetries are preserved. As a paradigmatic example, take the mirror Chern insulator. This system has topological bands in the different subspaces of mirror symmetry, namely Chern number $C = n$ and $C = -n$, with n an integer number. Then, in facets where the mirror symmetry is preserved, there will be two counterpropagating states, belonging to the two different eigenvalue subspaces of the mirror symmetry. However, in facets that do not preserve the mirror symmetry, bands will not be distinguished and the total Chern number will add up to 0 ($C = 0$).

The connection between topology and symmetry has been elucidated by the recently formulated theory of topological quantum chemistry (TQC) [10–13] and symmetry indicator formalism [14, 15]. It maps the symmetry properties of Bloch wavefunctions in reciprocal space to real space Wannier functions, which are localized around the atoms. The topological properties of an occupied set of bands can be characterized by the localization properties of those Wannier functions. A topologically trivial set of bands arises from exponentially localized, symemtry preserving Wannier functions. On the other hand, a set of bands arising from Wannier functions that do no satisfy one of these two properties must be topologically non-trivial. The set of bands that arise from exponentially localized, symmetric Wannier functions transforms under a representation of the symmetry space group called band representation (BR). Following the works of Zak *et al* [16–19], they showed that all BRs can be formed as a stacking of elementary band representations (EBR), which form a basis of trivial insulators. Thus, following TQC, a topological insulator is one whose BR cannot be decomposed as a sum of EBRs. TQC has also allowed for the discovery of new topological phases of matter, such as higher order TIs (d-dimensional systems with anomalous states in d-2, d-3 boundaries) and fragile topological phases (can be trivialized by the addition of topologically trivial bands). In this thesis, we will review the basic aspects of the theory solving step by step a very well known material, graphene. It will also be used to diagnose a mirror Chern insulator phase in PbTe, based on an old tight binding model [20–22]. There are few material realizations of the diverse topological phases of matter that have been theoretically predicted. The lack of materials is due to the expensive calculations required to diagnose them. However, the application of TQC has allowed for high-throughput searches of topological materials, rising the number of known topological insulators from hundreds to thousands [23, 24].

At the same time, there has been an increased interest in semimetallic systems. These systems, which lay in the boundary of metals and insulators, got under the spotlight after the synthesis of graphene, a 2D, one atom thick semimetal wherein electrons have a linear energy-momentum dispersion and behave as if they were mass-

less. The interest in this type of materials grew when the first Weyl semimetal was both predicted and confirmed experimentally in the TaAs family [25–28]. In Weyl semimetals conduction and valence bands meet at a finite number of points (Weyl nodes) inside the Brillouin Zone (BZ). Unlike TIs, they do not have a gap in the whole BZ, but, like TIs, they have non-trivial topological properties. In fact, Weyl nodes act as sources of Berry curvature, which translate into anomalous open surface states connecting their projection onto a surface. These are so-called *Fermi arcs*, and have a wide variety of properties [29–37] and promising applications [38–40]. Remarkably, any system with broken inversion or TRS can host these crossings, with no extra symmetry needed. In 2016, Bradlyn et al [32] proved that when non-symmorphic crystal symmetries are taken into account, Weyl nodes can be generalized. Instead of 2-band crossings, 3, 6 and 8-band degeneracies can be stabilized. These multifold fermions, display larger Berry curvatures, with a larger number of Fermi arcs too. As an important remark, these multifold fermions do not have an analogue in high energy physics, being only present in condensed matter systems where the symmetries are lowered with respect to vacuum. We will present our work on CoS_2, a ferromagnetic metal in which we found Weyl nodes and Fermi arcs, as well as a magnetic 4-fold fermion. We also found Nodal lines, the 1-dimensional generalization of crossings, that also have protected surface states. As aforementioned, the lack of symmetries has implications in topology too. We explore this issue by studying the response of a chiral magnet to time dependent strain. We find a new, purely 3-dimensional Hall viscosity, which gives rise to a dissipationless force. This viscosity has implications in the phonon spectrum of magnetic materials in tetrahedral point group, such as the family of Mn_3IrSi chiral magnets.

This thesis is focused on the role of symmetries in topological materials. It is divided in six chapters. In the first chapter, we review basic aspects of electronic band theory and topology. In the second chapter, we describe the recently introduced formalism of Topological Quantum Chemistry (TQC), [41] that generalizes the relation between topology and crystal symmetry. We use it to solve the well known example of graphene. We apply the described method of TQC and symmetry indicators to PbTe in the third chapter, a material that was predicted to host Dirac fermions in an anti-phase boundary in 1986, which translates to a mirror Chern insulator in modern terms. Next we study the role of TRS breaking in our recent discovery of Weyl nodes and Nodal lines on ferromagnetic pyrite CoS_2 in chapter four. We also found surface drumhead states and Fermi arcs. At the end of the chapter, we show the results of the collaboration with the experimental team that found the Fermi arcs using ARPES. In the last chapter, we show the effect that strain has on a topological chiral metal. Apart from breaking crystal symmetries and TRS, we find a novel, non-dissipative viscosity coefficient in 3D, the first pure 3D Hall viscosity. We also compute its numeric value on a toy model, as a proxy for chiral magnetic metals.

Finally, we summarize the main results of this thesis and the future work.

Chapter 1

Fundamentals of Topological Band Theory

1.1 Fundamentals of Electronic Band Theory

To study the macroscopical properties of solids from first principles (ab initio), we solve the microscopic Schrödinger equation of the crystal. As a first approach, we can think of solids as being formed by small units of repetition, where the relevant unit of measure is Angstrom, with atoms sitting inside. This unit cell is then repeated many[1] times in 1, 2 or 3 dimensions. Looking away from the boundaries, in the bulk, there is translational symmetry, which we will exploit to simplify the problem. If we focus on the bulk region, we have a system that can be solved; the nuclei of the atoms will create a periodic Coulomb potential in which we will insert electrons. We can then write the Hamiltonian of the system:

$$\begin{aligned} H = &- \sum_{i}^{N_n} \frac{\hbar^2}{2M_i} \nabla^2_{\mathbf{R}_i} - \sum_{i}^{N_e} \frac{\hbar^2}{2m_e} \nabla^2_{\mathbf{r}_i} + \sum_{i \neq j} \frac{Z_i Z_j}{|\mathbf{R}_i - \mathbf{R}_j|} \\ &- \sum_{i \neq j} \frac{Z_i}{|\mathbf{R}_i - \mathbf{r}_j|} + \sum_{i \neq j} \frac{1}{|\mathbf{r}_i - \mathbf{r}_j|} + V_{\mathrm{SOC}} + V_{\mathrm{F}}(\vec{B}, \vec{E}...) \end{aligned} \tag{1.1}$$

where N_n, N_e represent the number of nuclei and electrons. The first two terms correspond to the kinetic energy of nuclei and electrons, while the next three represent the Coulomb interaction between nuclei, electron-nuclei and electron-electron respectively. V_{SOC}, represents the Spin-Orbit Coupling, a relativistic effect that will have

[1] Macroscopic systems are formed by $\sim 10^{23}$ unit cells

important consequences. The last term, V_F, represents different external fields (magnetic, electric) and internal ones, such as spin polarization (intrinsic magnetization). This last term will be very important in the particular physics of magnets as we will see later on.

In a system with N_e electrons and N_n nuclei in 3D, we will have $3(N_e+N_n)$ degrees of freedom, which for real materials is an untractable big number. As a consequence, we need to make approximations to solve the problem. The first simplification one can apply is the Born-Oppenheimer approximation [42], in which we assume that the nuclei and electron description can be separated. This follows from the big difference in mass between nuclei and electrons. We thus neglect the many-body nature of the first two Coulomb terms, namely $V_{nn} = \sum_{i\neq j} \frac{Z_i Z_j}{|\mathbf{R}_i - \mathbf{R}_j|}$ and $V_{ne} = -\sum_{i\neq j} \frac{Z_i}{|\mathbf{R}_i - \mathbf{r}_j|}$. It is also standard to work in the limit of lowest temperature, $T \to 0$, named frozen nuclei approximation. Considering these two approximations, V_{nn} reduces to a constant while V_{ne} can be treated as a background (periodic) Coulomb potential. These approximations allows for a decoupling of the degrees of freedom $\Psi(R_i, r_j, t) = \psi(\{R_i\}, t)\phi(\{r_j\})$. V_{SOC} and V_{F} are not many-body terms, so the we will now focus our attention on the $V_{ee} = \sum_{i\neq j} \frac{1}{|\mathbf{r}_i - \mathbf{r}_j|}$ term.

The assumptions we made so far have been based on the real physical problem; nuclei are really close to their equilibrium position (when cold) and they are much heavier than electrons, so they move much slower. If we want to transform V_{ee} to a one-body operator, though, we will have to make further assumptions. The most straightforward way to tackle this is to do a mean-field approximation. In this scenario, we treat the interaction between electrons as if there was a background effective potential created by $N_e - 1$ electrons in which the remaining electron moves.

We can now rewrite the Hamiltonian of a single particle as follows:

$$H_{1p} = \frac{1}{2m}\nabla_r^2 + V_{\mathrm{eff}}(r) + V_{\mathrm{SOC}} + V_{\mathrm{F}} \tag{1.2}$$

where V_{nn} and V_{ne} have been absorbed in V_{eff}, as well as the approximated V_{ee}. Notice that we dropped the subindex 'e' from the mass in the kinetic term; we are dealing with an effective theory now, so the particles that are described this way aren't electrons anymore. We will see that in some cases the theory is successful enough to make the parallelism between these quasiparticles and real electrons. We have now reduced the many-body problem to many one body problems, which consists on solving the following eigensystem:

$$H_{1p} \left|\varphi_i\right\rangle = E_i \left|\varphi_i\right\rangle . \tag{1.3}$$

If we neglect the V_{SOC} term, wavefunctions $\varphi_i(\mathbf{r}) = \langle \mathbf{r}|\varphi_i\rangle$ are scalar functions. However, the addition of V_{SOC} makes it necessary to introduce spinors, vectors of

2-components in the spin Hilbert space, $(\varphi_i(\mathbf{r}), \chi_i(\mathbf{r}))^T$. This way, all terms other than V_{SOC} act the same on both spins (proportional to the identity Pauli matrix in spin space, σ_0), while $V_{SOC} \propto \boldsymbol{\sigma} \cdot (\boldsymbol{\nabla} V_{\text{eff}}(r)) \times \mathbf{p}$ manifestly mixes spins.

1.2 Periodic Crystal Potential and Bloch theorem

We have greatly reduced the difficulty of solving our problem, but we have done it so far in a very general way. We will now exploit the translational symmetry crystals to find general results.

1.2.1 Crystal lattice: Real and Reciprocal Spaces

Crystals are formed by a periodic repetition of identical unit cells in 3 space direction. Then, $\mathbf{R}_n$ labels the position of all each unit cell. The $\mathbf{R}_n$ points form a lattice, which can be described by means of some basis vectors, $\mathbf{a}_i$, in the following way[2]:

$$\mathbf{R}_n = n_1\mathbf{a}_1 + n_2\mathbf{a}_2 + n_3\mathbf{a}_3 \tag{1.4}$$

where $\mathbf{a}_i$ are 3 vectors that serve as a basis for the lattice (not all co-planar) and n_i are integer numbers. The set of all $\mathbf{R}$ vectors (n_1, n_2, n_3) is defined as *Bravais lattice*.

When dealing with periodic lattices, the standard way to exploit translational symmetry is by means of Fourier analysis, working on reciprocal space. Then, the periodicity of the lattice in real space transforms into periodicity in reciprocal space. The basis vectors of this reciprocal lattice $(\mathbf{b}_j)$ are defined through real space lattice vectors as

$$\mathbf{a}_i \cdot \mathbf{b}_j = 2\pi\delta_{ij} \tag{1.5}$$

where δ_{ij} is Kronecker's delta, which is 1 when $i = j$ and 0 otherwise. In 3 space dimensions, the standard way to define the $\mathbf{b_j}$ basis vectors is the following:

$$\begin{aligned}
\mathbf{b}_1 &= 2\pi \frac{\mathbf{a}_2 \times \mathbf{a}_3}{\mathbf{a}_1 \cdot \mathbf{a}_2 \times \mathbf{a}_3} \\
\mathbf{b}_2 &= 2\pi \frac{\mathbf{a}_3 \times \mathbf{a}_1}{\mathbf{a}_1 \cdot \mathbf{a}_2 \times \mathbf{a}_3} \\
\mathbf{b}_3 &= 2\pi \frac{\mathbf{a}_1 \times \mathbf{a}_2}{\mathbf{a}_1 \cdot \mathbf{a}_2 \times \mathbf{a}_3}.
\end{aligned} \tag{1.6}$$

Thus, the reciprocal lattice is defined as

[2] In 3 space dimensions.

$$\mathbf{G}_m = m_1\mathbf{b}_1 + m_2\mathbf{b}_2 + m_3\mathbf{b}_3. \tag{1.7}$$

From Fourier analysis we know that we can always express real space periodic functions as reciprocal space periodic functions via the relation:

$$f(\mathbf{r}+\mathbf{R}) = f(\mathbf{r}) \quad \rightarrow \quad f(\mathbf{r}) = \sum_{\mathbf{G}} e^{i\mathbf{G}\cdot\mathbf{r}}\hat{f}(\mathbf{G}). \tag{1.8}$$

Then, we can apply it to the space-dependent functions relevant to our problem; the Hamiltonian and its eigenvectors.

1.2.2 Bloch Theorem

Even though the effective potential can have a complicated structure, it follows from the periodicity of the system that it must display the same translational symmetry. Let's forget for the time being about the external field term V_{F}[3] so that the only remaining potential is the Coulomb potential created by the ions, which must have the same periodicity as the lattice. Let's start by reviewing the properties of the translation operator.

We define the translation operator $\hat{T}$ as the one that has the following action on a space-dependent function:

$$\hat{T}(\mathbf{R})f(\mathbf{r}) = f(\mathbf{r}+\mathbf{R}). \tag{1.9}$$

Notice that it doesn't matter the order in which translations are applied, since

$$\begin{aligned}\hat{T}_{\mathbf{R}}\hat{T}_{\mathbf{R}'}f(\mathbf{r}) = \hat{T}_{\mathbf{R}}f(\mathbf{r}+\mathbf{R}') = f(\mathbf{r}+\mathbf{R}'+\mathbf{R}) = \\ = f(\mathbf{r}+\mathbf{R}+\mathbf{R}') = \hat{T}_{\mathbf{R}'}f(\mathbf{r}+\mathbf{R}) = \hat{T}_{\mathbf{R}'}\hat{T}_{\mathbf{R}}f(\mathbf{r})\end{aligned} \tag{1.10}$$

so the composition of translations is commutative. If translations form a group, we can apply the group theory to simplify the underlaying problem. We will now check if the translation operator also satisfies the properties of a group:

- *Identity*

$$\hat{T}_{\mathbf{0}}f(\mathbf{r}) = f(\mathbf{r}+\mathbf{0}) = f(\mathbf{r}), \tag{1.11}$$

  so $\hat{T}_{\mathbf{0}}$ leaves f invariant and, thus, is the identity element.

[3] We will include it later, without lose of generality.

- *Inverse*
$$\hat{T}_{-\mathbf{R}}\hat{T}_{\mathbf{R}}f(\mathbf{r}) = \hat{T}_{-\mathbf{R}}f(\mathbf{r}+\mathbf{R}) = f(\mathbf{r}+\mathbf{R}-\mathbf{R}) = f(\mathbf{r}), \tag{1.12}$$
so $\hat{T}_{-\mathbf{R}}$ is the inverse element for each $\hat{T}_{\mathbf{R}}$.

- *Associative*
$$\hat{T}_{\mathbf{R}}\left(\hat{T}_{\mathbf{R}'}\hat{T}_{\mathbf{R}''}f(\mathbf{r})\right) = f(\mathbf{r}+\mathbf{R}+\mathbf{R}'+\mathbf{R}'') = \left(\hat{T}_{\mathbf{R}}\hat{T}_{\mathbf{R}'}\right)\hat{T}_{\mathbf{R}''}f(\mathbf{r}) \tag{1.13}$$

- *Closed*
$$\hat{T}_{\mathbf{R}}\hat{T}_{\mathbf{R}'} = \hat{T}_{\mathbf{R}''}, \tag{1.14}$$
with $\mathbf{R}'' = \mathbf{R}+\mathbf{R}'$ also a Bravais lattice vector.

This operation satisfies all properties of a group, plus commutativity, so that translations form an *Abelian group*. In group theory, these groups have the special property that all of its irreducible representations are 1 dimensional. Thus, we can assign a 1x1 matrix to each translation such that these matrices (or matrix representations, matrix representatives) satisfy the algebra of the group.

From group theory, we know that the representation for such groups are complex exponentials [43]. Let's define our representation as

$$\rho^{\mathbf{k}}(\hat{T}_{\mathbf{R}}) = e^{i\mathbf{k}\cdot\mathbf{R}}. \tag{1.15}$$

where $\mathbf{k}$ is a vector that, for the moment, labels the different irreducible representations of the translation group. It is straightforward to see that this representation complies with all the requirements aforementioned. Let us now apply these group theory tools to our problem.

Since the Hamiltonian H_{1p} is periodic, we conclude that

$$\hat{T}_{\mathbf{R}}\left(H_{1p}(\mathbf{r})\Psi(\mathbf{r})\right) = H_{1p}(\mathbf{r}+\mathbf{R})\Psi(\mathbf{r}+\mathbf{R}) = H_{1p}(\mathbf{r})\Psi(\mathbf{r}+\mathbf{R}) = H_{1p}(\mathbf{r})\hat{T}_{\mathbf{R}}\Psi(\mathbf{r}), \tag{1.16}$$

so that $[\hat{T}_{\mathbf{R}}, H] = 0$. Thus, we can diagonalize at the same time the translation and Hamiltonian operators. In the group theory, this implies the eigenstates of the Hamiltonian will transform under the irreducible representations of the translation group. Then, if $\Psi_{\mathbf{k}}(\mathbf{r})$ is an eigenstate of the Hamiltonian, under translation operator the eigenstate will transform according to an irreducible representation $\rho^{\mathbf{k}}$ of the translation group:

$$\hat{T}_{\mathbf{R}}\Psi_{\mathbf{k}}(\mathbf{r}) = \Psi_{\mathbf{k}}(\mathbf{r}+\mathbf{R}) = \rho^{\mathbf{k}}\left(\hat{T}_{\mathbf{R}}\right)\Psi_{\mathbf{k}}(\mathbf{r}) = e^{i\mathbf{k}\cdot\mathbf{R}}\Psi_{\mathbf{k}}(\mathbf{r}) \tag{1.17}$$

which is the definition of Bloch's theorem from a group theory perspective. Following this result, we can further decompose the eigenstate of the Hamiltonian in the following form

$$\Psi_{\mathbf{k}}(\mathbf{r}) = e^{i\mathbf{k}\cdot\mathbf{r}} u_{\mathbf{k}}(\mathbf{r}), \text{ with } u_{\mathbf{k}}(\mathbf{r}+\mathbf{R}) = u_{\mathbf{k}}(\mathbf{r}), \tag{1.18}$$

whith $\Psi_{\mathbf{k}}(\mathbf{r})$ being the Bloch wavefunction.

We will now apply periodic boundary conditions[4] in the direction of the lattice vectors:

$$\Psi_{\mathbf{k}}(\mathbf{r} + N_i\mathbf{a}_i) = \Psi_{\mathbf{k}}(\mathbf{r}). \tag{1.19}$$

where N_i is the number of unit cells in the i$^{\text{th}}$ direction.

Following previous derivations, we get:

$$\Psi_{\mathbf{k}}(\mathbf{r} + N_i\mathbf{a}_i) = e^{i\mathbf{k}\cdot(\mathbf{r}+N_i\mathbf{a}_i)} u_{\mathbf{k}}(\mathbf{r} + N_i\mathbf{a}_i) = e^{i\mathbf{k}\cdot(\mathbf{r}+N_i\mathbf{a}_i)} u_{\mathbf{k}}(\mathbf{r}) = e^{i\mathbf{k}\cdot\mathbf{r}} u_{\mathbf{k}}(\mathbf{r}) = \Psi_{\mathbf{k}}(\mathbf{r}). \tag{1.20}$$

If we write $\mathbf{k} = \sum_i x_i \mathbf{b}_i$, then:

$$e^{i\mathbf{k}\cdot(N_i\mathbf{a}_i)} = 1, \quad \rightarrow \quad e^{i(x_j\mathbf{b}_j)\cdot(N_i\mathbf{a}_i)} = e^{2\pi i N_i x_j \delta_{ij}} = e^{2\pi i N_i x_i} = 1. \tag{1.21}$$

From here we extract that the only allowed values for $\mathbf{k}$ are $x_i = \frac{m}{N_i}$, with m an integer number in $\{0, N_i - 1\}$[5]. Notice that there are exactly as many different values of $\mathbf{k}$ as there are unit cells in real space $N_1 N_2 N_3$, so we haven't lost any information in the process. All values of $\mathbf{k}$ lie within the cell created by reciprocal basis vectors which is called First Brillouin Zone (FBZ or BZ when the context is clear), and it will be of great importance through the work, since all bulk properties come from the information that we can extract from this region[6].

So far we have showed that the vector $\mathbf{k}$ can be used to label states that diagonalize simultaneously both the Hamiltonian and translation operator, but we haven't given any physical interpretation. If we compute the expected value of momentum operator $-i\hbar\boldsymbol{\nabla}$ on a Bloch wavefunction, we get

$$-i\hbar\boldsymbol{\nabla}\Psi_{\mathbf{k}}(\mathbf{r}) = -i\hbar\boldsymbol{\nabla} e^{i\mathbf{k}\cdot\mathbf{r}} u_{\mathbf{k}}(\mathbf{r}) = \hbar\mathbf{k}\Psi(\mathbf{r}) + e^{i\mathbf{k}\cdot\mathbf{r}}\boldsymbol{\nabla} u_{\mathbf{k}}(\mathbf{r}). \tag{1.22}$$

[4]This is the standard way to describe bulk periodic systems, we will have to revisit the point when discussing finite systems.

[5]Notice that the case where $m = N_i$ is the same as the $m = 0$ case.

[6]The rest of Brillouin zones are copies of the first, due to periodicity, that's why we only study the first one.

We can see here that the vector $\mathbf{k}$ behaves in the same way as the wavevector of wavefunctions, so that the $\hbar\mathbf{k}$ term seems to be the linear momentum of a wavefunction. However, there is an extra term, $e^{i\mathbf{k}\cdot\mathbf{r}}\boldsymbol{\nabla}u_{\mathbf{k}}(\mathbf{r})$, which does not vanish and breaks the analogy. The standard procedure is then to interpret it as the electron *crystal momentum*.

Taking into account all this, we can rewrite the Hamiltonian eigenproblem in the new basis to find

$$\left[\frac{\hbar^2}{2m}\left(-i\boldsymbol{\nabla}+\mathbf{k}\right)^2+V_{\text{eff}}(\mathbf{r})\right]u_{\mathbf{k}}(\mathbf{r})=E_{\mathbf{k}}u_{\mathbf{k}}(\mathbf{r}) \tag{1.23}$$

where V_{SOC} is included inside V_{eff}.

When we solve the eigensystem, the resulting energies come in packages; densely populated groups of energies that are split between themselves by a finite amount. Each level has a finite width in energy and is called a *band* [44]. Although a good visualization of the energy states, this gives us very limited information on the system. We can choose, however, to plot the energy bands as a function of momentum. This gives further information that, as we will see later, will be of crucial importance in terms of symmetry and, in general, in terms of topology.

1.3 Computing Methods

In this section we will review the two main methods employed in this thesis to solve the electronic structure of materials: Density Functional Theory (DFT) and tight binding (TB) method.

1.3.1 Density Functional Theory

Simplifying the many-body problem Hamiltonian to a single particle picture has been a drastic approximation, especially the mean-field treatment of V_{ee}. However, in 1964, Hohenberg and Kohn [45] proved that the exact energy E of the ground state system can be written as a functional of the exact electron density n, $E[n]$. The power of this result is that the electron density doesn't understand about many-body or single-body physics; Kohn and Sham then proposed [46] that we can choose a single-body problem that has the exact same density as the many-body one and get the exact energy.

The only thing left to find is the auxiliary system that mimics the properties of the real many-body system. However Hohenberg and Kohn only proved that such functional *exists*, not its actual functional form. The exact Hamiltonian reads

$$H = T + V_{\text{ee}} = T + V_{\text{H}} + V_{\text{xc}}, \tag{1.24}$$

with $T = -\sum_i^{N_e} \frac{\hbar^2}{2m_e}\nabla_{r_i}^2$ describing the kinetic term, $V_{\text{H}} = \frac{e^2}{2}\int d\mathbf{r}d\mathbf{r}' \frac{n(\mathbf{r})n(\mathbf{r}')}{|\mathbf{r}-\mathbf{r}'|}$ the Hartree term and the last term, the exchange correlation functional, which is the exact term minus the Hartree one, $V_{\text{ee}} - V_{\text{H}}$.

We can then write the expected value of the ground state energy as a functional of the electron density. If we denote by ϕ_i the occupied states (and $n = \sum_i \phi_i^*\phi_i$), then the energy functional takes the following form:

$$E[n] = \sum_i \int d\mathbf{r}\phi_i^* \left(-\frac{\hbar^2}{2m_e}\nabla^2\right)\phi_i + \frac{e^2}{2}\int d\mathbf{r}d\mathbf{r}' \frac{n(\mathbf{r})n(\mathbf{r}')}{|\mathbf{r}-\mathbf{r}'|} + E_{\text{xc}}[n]. \tag{1.25}$$

Following the Kohn Sham scheme mentioned earlier, we can rewrite the equations in terms of an effective potential, v_{eff}, that encodes all the interactions:

$$v_{\text{eff}} = e^2 \int d\mathbf{r}' \frac{n(\mathbf{r}')}{|\mathbf{r}-\mathbf{r}'|} + \frac{\delta E_{\text{xc}}[n]}{\delta n}. \tag{1.26}$$

From here we get the Kohn-Sham equations,

$$\left(-\frac{\hbar^2}{2m_e}\nabla^2 + v_{\text{eff}}[n_0]\right)\phi_i = \epsilon_i\phi_i. \tag{1.27}$$

Thus, the many-body problem has been reduced to a 1-body problem that has the same exact electron density and ground state energy. There are several approximation schemes one can use that perform well at describing real materials though. Local (Spin) Density Approximation (L(S)DA) [46], which uses the exact exchange correlation term for the free electron gas, has succeeded in predicting the electronic properties of materials where electrons are mostly free, such as graphene, with very delocalized electrons coming from carbon p_z orbitals. The General Gradient Approximation (GGA) [47] and its generalizations (MBJ) [48] have succeeded in accurately predicting the value of the gap for several insulators. As we will see explicitly in the case of PbTe, the correct prediction of the gap can drastically change the properties of a material, especially the topological ones.

DFT is the standard method to compute electronic structures of materials. There is a numerical algorithmic procedure that, starting from an initial guess, finally converges in an iterative way. In what follows, we describe the procedure of numerically solving the equations.

- We start with an initial guess for the electron density, n_0. There are many schemes to choose the first electron density, such as a random combination of

atomic orbitals or the most common one in electronic bandstructure codes (such as VASP), which is based on a superposition of spheric atomic densities.

- Then, we choose the E_{xc} and construct the effective potential $v_{\text{eff}}[n]$.
- We now solve the Kohn Sham equation (see Eq. 1.27) and find the eigenstates ϕ_i^1.
- From these eigenstates, we construct the new electronic density, $n_1 = \sum_i \phi_i^{1*}\phi_i^1$.
- We now compare n_0 and n_1. If the difference is below a certain threshold, then we decide that the process converged and we take n_1 as the electronic density solution. In case this condiciton is not satisfied, we will go to the second step and solve the Kohn-Sham equation again until it converges.

Throughout this thesis, we will mainly use the Vienna ab initio simulation package (VASP) [49–52] and Quantum Espresso (QE) [53–55].

Before finishing this part, we will introduce a technique that is widely used as a simplification for faster convergence, the Pseudopotential approximation. Since the main properties of solids stem from the states close to the Fermi level, it is safe to integrate out the electrons that are very low in energy, the core electrons. Then, we consider the core electrons to be frozen, and we neglect them. We are left with valence electrons then. The ab initio codes we use in this thesis are plane-wave based; they expand the Kohn-Sham orbitals in terms of planes waves with a fixed cutoff energy. When considering valence electrons, they are from high atomic levels, so they oscillate rapidly near the origin (this is in order to satisfy the orthogonality relations of atomic orbitals). These functions are numerically expensive to represent in terms of plane-waves, due to the large cutoff required. Then, by using pseudopotentials we can regularize the highly oscillating functions near the origin while keeping it exact beyond some specific distance called the cutoff radius.

The effectiveness of the pseudopotentials is also affected by the surrounding crystal structure, thus there is no a unique choice of pseudopotential that works for a particular atom in all situations, and we must be careful to check different ones and compare the results.

1.3.2 Tight Binding

Other than ab initio methods, we can also think of other ways to get energy bands that reproduce key properties of the systems we want to study at a qualitative level. This proves to be a good approach for topological phases, which are equivalent to simpler

systems if they are adiabatically connected[7]. This is the reason why the tight binding method is extensively used throughout all topology literature as an easy method to visualize complex topological non-trivial systems. In this section, we review the main aspects of the method.

First, we assume that atoms have a finite set of orbitals sitting at the atomic positions that are mainly decoupled from the orbitals in other sites (atomic insulator limit) and we start considering all possible tunnelings between neighboring sites. Let us analyze the case where we have n_o atomic orbitals per atom, and n_s atomic sites per unit cell. For simplicity of notation, we denote by n the tuple (n_o, n_s), which labels all states inside a unit cell.

At first glance, a sensible choice of basis for the crystal would be to consider $N_1N_2N_3n$ atomic orbitals sitting at the different unit cells of the crystal, $\phi^n_{\mathbf{R}}(\mathbf{r}) = \phi^n(\mathbf{r}-\mathbf{R})$ (due to periodicity). However, the basis functions are not eigenstates of the translation operator or the Hamiltonian. This can be solved by constructing Bloch wavefunctions out of these localized orbitals in the following way:

$$\Phi^n_{\mathbf{k}}(\mathbf{r}) = \sum_{\mathbf{R}} e^{i\mathbf{k}\cdot(\mathbf{R}+\mathbf{r}_n)}\phi^n(\mathbf{r}-(\mathbf{R}+\mathbf{r}_n)) = \langle \mathbf{r}|n\mathbf{k}\rangle \tag{1.28}$$

where $\mathbf{r}_n$ denotes the position of the orbital with respect to the origin of the cell. In what follows, as introduced in the last step, we will use Dirac notation. We can now express the tight binding Hamiltonian as a $n\times n$, k-dependent matrix in the following way

$$H_{\mathrm{TB}}(\mathbf{k})_{mn} = \langle m\mathbf{k}|\, H\, |n\mathbf{k}\rangle \tag{1.29}$$

Notice that we haven't lost any degree of freedom. We went from a Hamiltonian, which in the basis of localized functions was a $N_1N_2N_3n \times N_1N_2N_3n$ matrix to a $\mathbf{k}$ dependent ($N_1N_2N_3$ $\mathbf{k}$ values) $n\times n$ matrix. As you can see, the problem just became more easily treatable. We will see examples of tight binding models in following sections and chapters.

1.4 Wannier functions

So far, to solve the problem we have exploited translational symmetry in reciprocal space rather than in real space. In that case, we got a basis of Bloch wavefunctions $\Psi_n(\mathbf{k})$ that are eigenstates of the Hamiltonian both with definite energy $E_n(\mathbf{k})$ and

[7]Two systems are topologically equivalent if it can be found an adiabatic deformation that turns one into the other. In the context of topological insulators, preserving the gap is standardly what is referred to as adiabatic deformation.

crystal momentum $\mathbf{k}$. These wavefunctions, however, are poorly localized in real space (they are plane waves). So we can try to find another basis that describes the same physics, but that is localized in real space. As we will see later, this basis will have important prediction capabilities for topological phases.

The standard way to construct a basis in real space out of a basis on reciprocal space is to Fourier antitransform (the opposite way we did when defining Bloch wavefunctions for the tight binding basis):

$$|\mathbf{R}n\rangle = \int d\mathbf{k} e^{-i\mathbf{k}\cdot\mathbf{R}} |\mathbf{k}n\rangle \,. \tag{1.30}$$

As we can infer from Eq. 1.30, after the transformation we will have a basis of functions such that we get n functions per real space unit cell $\mathbf{R}$.

An important property of Wannier functions is that they are not unique. Wavefunctions are defined up to a phase factor $e^{i\theta}$, which does not change the energies. This is the definition of a gauge symmetry, which we can exploit. In the particular case of m occupied bands, we can apply any $U(n)$ unitary transformation to $\Psi_m(\mathbf{k})$, at any $\mathbf{k}$, such that the energy spectrum of the m bands remains unchanged. This gauge choice translates into a different set of Wannier functions that will have different properties, in particular, with respect to localization. Then, the accurate definition of Wannier functions would be:

$$|\mathbf{R}n\rangle = \int d\mathbf{k} e^{-i\mathbf{k}\cdot\mathbf{R}} U_{nm}(\mathbf{k}) |\mathbf{k}m\rangle \,, \tag{1.31}$$

where $U_{nm}(\mathbf{k})$ is a unitary $n \times n$ matrix, that can be written as a function of $\mathbf{k}$.

It is known from Fourier analysis that a necessary condition for a function to be localized in real space is that the function has to be smooth in reciprocal space. In fact, the smoother the function in reciprocal space, the more localized it will be in real space. This is how we can exploit the gauge symmetry. Through a procedure nowadays named as "Wannierization" [56], we can choose the $U_{nm}(\mathbf{k})$ matrices to make the Bloch wavefunctions as smooth as possible, making the Wannier functions, thus, maximally localized[8].

Throughout this thesis, we will make use of the Wannierization procedure to construct maximally localized Wannier functions out of Bloch wavefunctions, to then obtain an effective TB model that reproduces the electronic properties the systems. Even though ab initio calculations are computationally expensive, from a coarse grained grid of k-points in the Brillouin zone we can interpolate the Hamiltonian to a finer grid through the Wannierization process as follows.

[8] In this context, maximally localized implies that the tail of the Wannier functions has to decay exponentially with the distance, instead of polynomially.

Once obtained the $|\mathbf{R}n\rangle$ Wannier functions out of the $|\mathbf{k}n\rangle$ Bloch wavefunctions, we can construct Bloch wavefunctions out of those Wannier functions again,

$$|\mathbf{k}n\rangle = \sum_{\mathbf{R}} e^{i\mathbf{k}\cdot\mathbf{R}} |\mathbf{R}n\rangle , \tag{1.32}$$

and write the interpolated Hamiltonian in the Wannier basis:

$$H^W_{nm}(\mathbf{k}) = \langle \mathbf{k}n| H |\mathbf{k}m\rangle = \sum_{\mathbf{R}} e^{i\mathbf{k}\cdot\mathbf{R}} \langle \mathbf{0}n| H |\mathbf{R}m\rangle , \tag{1.33}$$

where there are as many $\mathbf{R}$ terms as k-points in the original ab initio calculation. This is however computationally inexpensive, and, given that the Wannierization process is accurate, will give us the possibility to explore the electronic bands in very fine meshes of momentum space.

To end the section, it is important to mention that there is an intermediate step between Bloch wavefunctions and Wannier functions. We can define the so called Hybrid Wannier functions; wavefunctions that are localized on one direction but still Bloch wavefunctions in the other directions:

$$\left|\mathbf{R}_\parallel \mathbf{k}_\perp n\right\rangle = \int d\mathbf{k}_\parallel e^{-i\mathbf{k}_\parallel\cdot\mathbf{R}_\parallel} \left|\mathbf{k}_\parallel, \mathbf{k}_\perp n\right\rangle . \tag{1.34}$$

These functions are called Hybrid Wannier functions and will have an important role in diagnosing topology.

1.5 Topology: Zak phase, Chern number and Wilson loop

In periodic systems that can be described by the previosuly introduced machinery, there is a special quantity one can compute that is related to topology: the Zak phase[9]. In the following section, we will derive the main results regarding Zak phase and its generalizations, the Wilson Loops.

Let us start with the simplest case; a system that is periodic on 1 direction and has 1 band. Then, the eigenstates of the system can be denoted by the crystal momentum k (not a vector, but a number). We define the Berry connection as

[9]For the sake of clarity, we will keep the name of Zak phase during the whole section. In the topological physics field, however, it is customary to interchange Zak's and Berry's name when referring to this and related quantities. That is why in following chapters we will refer to these quantities as Berry phase.

$$A(k) = i \langle k| \frac{d}{dk} |k\rangle . \tag{1.35}$$

Notice that this quantity is not a gauge invariant quantity. In fact, if we change $|k\rangle \rightarrow e^{i\theta(k)} |k\rangle$, we get that the Berry connection changes by a total derivative, $A(k) \rightarrow A(k) + \frac{d\theta}{dk}$, which means that it is gauge covariant. However, if we integrate it along the whole BZ

$$\int_0^{2\pi} dk A(k) = \phi. \tag{1.36}$$

we get a gauge invariant quantity ϕ which is known as Berry phase, or Zak phase in the context of band theory. Because it is gauge invariant, this quantity can have physically measurable consequences.

Actually, in 1D systems, ϕ is related to the expected value for the position of the Wannier function of the band in real space, in other words, the center of charge. Notice that the operator inside the bracket is the definition of the position operator in momentum space (with a missing 2π factor). Then, the relationship between Zak phase and Wannier Charge Center (WCC) is the following

$$x_0 = \frac{\phi}{2\pi}. \tag{1.37}$$

There is a huge variety of Wannier functions that we can construct depending on the gauge we choose. All of them, though, share the same center, since the Zak phase is gauge invariant. Then, if we can relate physical properties to the WCCs, we won't need to go through the whole computation of Wannier functions. As we will see in following sections/chapters, the WCCs are intimately related to the topology of the bands.

The values of this phase can be constrained by symmetries. As an example, if we have a symmetry that takes k to $-k$ (inversion, mirror, C_2...), it will take ϕ to $-\phi$. Since the phase ϕ is only defined modulo 2π, this symmetry forces the Berry phase to be either 0 or π. This particular result will be useful when we study the Su-Schrieffer-Heeger model and Nodal line semimetals.

The Berry connection can be easily generalized to a set of more bands, realizing the so called Non-Abelian Berry connection

$$A_{mn}(k) = i \langle mk| \frac{d}{dk} |nk\rangle , \tag{1.38}$$

and non-abelian Zak phases,

$$\phi_{mn} = \frac{1}{2\pi} \int_0^{2\pi} dk A_{mn}(k), \tag{1.39}$$

which are the eigenvalues of the ϕ_{mn} matrix.

We can also generalize it to the case of greater dimension and construct another important object for topology: the Berry curvature. In 2D, starting as before, we can construct the non-Abelian Berry connection:

$$\boldsymbol{A}_{mn}(\mathbf{k}) = i \langle mk| \boldsymbol{\nabla}_{\mathbf{k}} |nk\rangle . \tag{1.40}$$

We can also define a Zak phase with the path of integration being any closed loop in the 2D BZ:

$$\phi_{mn} = \frac{1}{2\pi} \oint_{\delta S} d\mathbf{k} \cdot \boldsymbol{A}_{mn}(\mathbf{k}). \tag{1.41}$$

Applying Stokes' theorem:

$$\phi_{mn} = \frac{1}{2\pi} \oint d\mathbf{k} \cdot \boldsymbol{A}_{mn}(\mathbf{k}) = \frac{1}{2\pi} \int_S dS \boldsymbol{\nabla}_{\mathbf{k}} \times \boldsymbol{A}_{mn}(\mathbf{k}). \tag{1.42}$$

We translated the computation of the phase along the line to the computation of the flux of $\boldsymbol{\nabla}_{\mathbf{k}} \times \boldsymbol{A}_{mn}(\mathbf{k})$ to the enclosing surface S. This tensor is called Berry curvature:

$$\Omega_{mn}(\mathbf{k}) = \boldsymbol{\nabla}_{\mathbf{k}} \times \boldsymbol{A}_{mn}(\mathbf{k}). \tag{1.43}$$

One interesting calculation would be to compute the Zak phase by integrating the Berry curvature on the whole 2D BZ. For the case of one band we have:

$$\phi = \frac{1}{2\pi} \int_S dS\, \Omega(\mathbf{k}) = 2\pi C, \tag{1.44}$$

where C is a well known quantity in topology; the first Chern number. If we generalize it to multiple bands it will read:

$$C = \frac{1}{2\pi} \mathrm{Tr} \left(\int_S dS\, \Omega_{mn}(\mathbf{k}) \right). \tag{1.45}$$

Since the 2D BZ has no boundary (it is a 2-Torus), applying Stokes' theorem the other way round, the Berry phase vanishes as the boundary vanishes. This would mean that the Berry phase of all 2D periodic systems had to vanish, which we know not to be true (Topological Insulators). The problem, then, has to lie in the applicability of Stokes' theorem. In other words, *a non-zero Chern number is an obstruction to apply Stokes' theorem*, which cannot be applied if we cannot build a smooth gauge in the whole region of integration, in this case, the BZ. So the Chern number is *an obstruction to find a smooth gauge on the 2D BZ.*

In terms of Wannier functions, this has a very interesting consequence; in order to find maximally localized Wannier functions it is necessary to find a smooth gauge in the whole BZ. Then, since having a non-zero Chern number forbids the construction of such gauge, *having a non-zero Chern number is an obstruction to find maximally localized Wannier functions*. This is the first example of how topology obstructs the construction of maximally localized Wannier functions, and why the Wannier function formalism is useful to diagnose topology, as we will see later in the description of the theory of Topological Quantum Chemistry [41].

Apart from computing the Chern number by integrating the Berry curvature to the whole BZ, we can compute the Wilson Loops, which are computationally more efficient and have a close relation to the bulk-boundary correspondence of Topological Insulators. In this context, we can define the Wilson loop as the calculation of Zak phases integrating on one momentum direction as a function of the other momentum direction:

$$\phi_1(k_2) = \frac{1}{2\pi}\int_0^{2\pi} dk_1 A_1(k_1, k_2). \tag{1.46}$$

As it shown in Fig. 1.1 (a), starting from k_1^0 point, we compute the Berry phase integrating on k_2. We then plot the resulting phases as a function of momentum k_1. Notice that the spectrum of the Zak phase ϕ is periodic both in ϕ (because phases are only defined $\mod 2\pi$) and k_1 (the BZ is periodic in both k_1 and k_2). Then, we can have two qualitatively different plots, as shown in Figs. 1.1 (b-c). In Fig. 1.1 (b), the phase ϕ always stays close to 0. We can adiabatically deform that path to be always exactly at 0. As we argued in Sec. 1.4, the Berry phase is related to the expected value of the center of Wannier functions. If we only localize on one direction (as in this case, integrating only on k_2), we get Hybrid Wannier Charge Centers (HWCCs). Then, a flat Wilson Loop spectrum ($\phi_1(k_2) = 0$) translates into a Hybrid Wannier function being located at the origin for every value of k_1.

On Fig. 1.1 (c) we have a qualitatively different case. Now we cannot deform the Wilson loop spectrum to be exactly at 0. Starting at the origin, as k_1 varies, it moves from the origin of one unit cell to the origin of the next one. Thus, when trying to compute the center of the Wannier function on the other direction (k_1) we would meet an obstruction. Indeed, as k_1 goes over a whole cycle, the Zak phase changes an integer number of times 2π, one in this case. This is another way to compute the Chern number; *the winding of the HWCCs is the Chern number*. Connecting with the definition of Chern number, the winding of HWCCs represents an obstruction to computing maximally localized Wannier functions.

This can be generalized to the multiband case. We can plot the partial phases, i.e., the eigenvalues of the phase matrix in Eq. 1.41 to see the partial windings, with

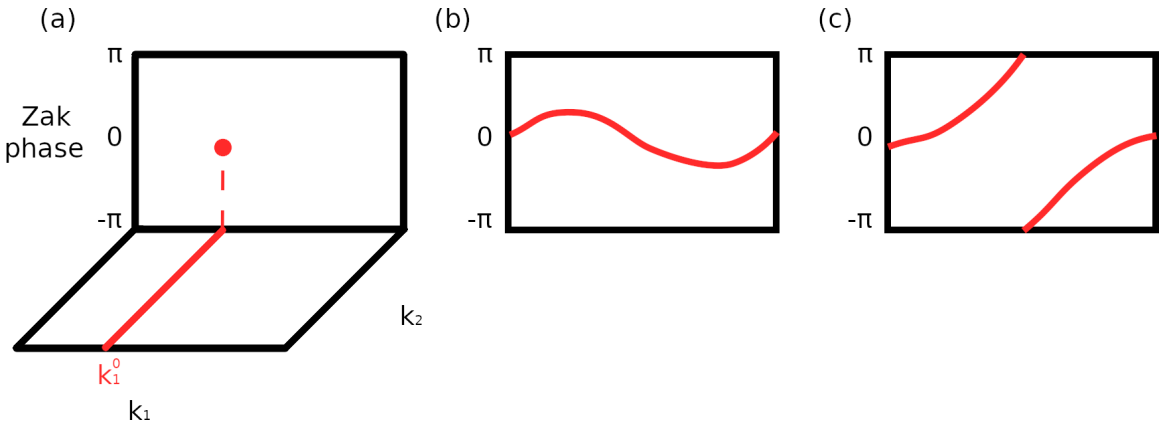

Figure 1.1: Wilson loop in the case of a single band. (a) Zak phase integration in the k_2 direction, as a function of k_1^0. (b) and (c) Wilson Loop calculation. (b) Chern number $C = 0$ Wilson Loop. (c) Chern number $C = 1$ Wilson loop.

the net Chern number being the sum of all partial phases, i.e., the trace of the Zak phase matrix.

In the next section we will see examples of how these quantities are computed in real models and the consequences on the surface spectrum.

1.6 Su-Schrieffer-Heeger model

In this section we will solve the Su-Schrieffer–Heeger (SSH) model, the simplest model with edge states in 1D. We start by defining the system as shown in Fig. 1.2. The lattice is formed by two s orbitals placed at the 2c Wyckoff position, in the coordinates $-x$ and x, which we denote as sites A and B, and the orbitals at the nth unit cell as $|n_A\rangle$ and $|n_B\rangle$. We choose $a = 1$ for simplicity. Then, following the tight binding procedure described in Sec. 1.3.2 we construct the basis of Bloch wavefunctions:

$$\begin{aligned} |k_A\rangle &= \frac{1}{\sqrt{N}} \sum_n e^{-ik(n-x)} |n_A\rangle \\ |k_B\rangle &= \frac{1}{\sqrt{N}} \sum_n e^{-ik(n+x)} |n_B\rangle \,, \end{aligned} \tag{1.47}$$

with N the number of unit cells.

Setting the on-site energies to 0, the only energetic terms are the nearest neighbors (NN) hopings t and t', which are defined as:

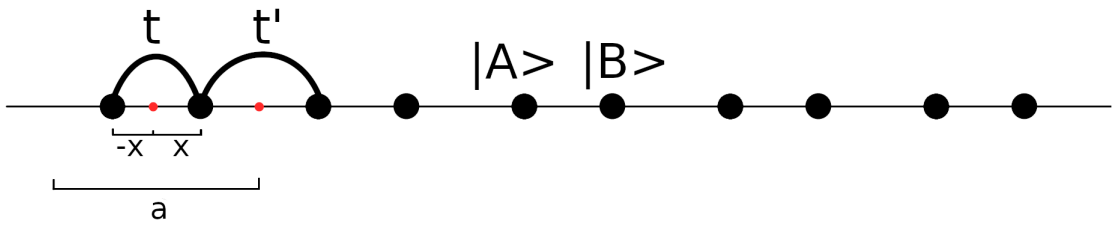

Figure 1.2: Crystal structure of the SSH model. Solid points represent orbital positions and solid lines represent tight binding hopping parameters. Red points represent the location of inversion symmetry centers.

$$\langle n_A| H |m_B\rangle = t\delta_{n,m} + t'\delta_{n+1,m}. \tag{1.48}$$

The hopping t will be referred to as intracell hopping (connects two sites in the same unit cell) and t' as intercell hopping (connects sites at two different unit cells). The Hamiltonian in reciprocal space then will be off-diagonal, with components

$$\begin{gathered}\langle k_A| H |k_B\rangle = \frac{1}{N}\sum_{n,m} e^{ik(n-x)}e^{-ik(m+x)} \langle n_A| H |m_B\rangle = \\ \frac{1}{N}\sum_{n,m} e^{ik(n-m-2x)}(t\delta_{n,m} + t'\delta_{n+1,m}) = \frac{1}{N}\sum_{n} t + t'e^{-ik(2x+1)} = t + t'e^{-ik(2x+1)},\end{gathered} \tag{1.49}$$

so, the resulting Hamiltonian in momentum space reads

$$H(k) = \begin{pmatrix} 0 & t + t'e^{-ik(2x+1)} \\ t + t'e^{ik(2x+1)} & 0 \end{pmatrix}. \tag{1.50}$$

We now diagonalize it following standard methods and we obtain the eigenvalues

$$E_{\pm}(k) = \pm\sqrt{t^2 + t'^2 + 2tt'\cos(k)}, \tag{1.51}$$

and eigenvectors

$$|k_{\pm}\rangle = \frac{1}{\sqrt{2}}\left(e^{-ikx}, \frac{t + t'e^{ik(1+x)}}{E_{\pm}}\right). \tag{1.52}$$

The spectrum becomes gapless at $k = \frac{1}{2}$ for $t = t'$. We will now study analytically two limits; $t' = 0$ and $t = 0$.

In the case of $t' = 0$, the eigenvalues and eigenstates become

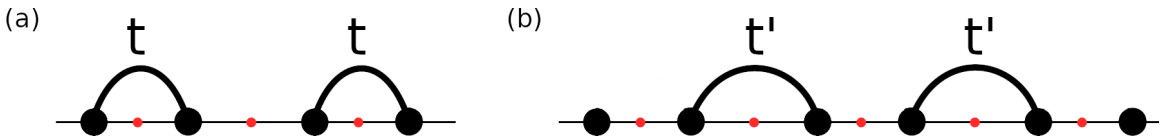

Figure 1.3: Limit cases of the SSH model. (a) Trivial case. The crystal becomes a succession of isolated dimers. (b) Non-trivial case. The dimers connect neighboring cells, so there will be an edge state when making the model finite. Notice that a redefinition of the origin would reverse the definition of trivial and non-trivial.

$$\begin{aligned} E_{\pm} &= t \\ |k_{\pm}\rangle &= \frac{1}{\sqrt{2}}\left(e^{-ikx}, \pm e^{ikx}\right). \end{aligned} \tag{1.53}$$

Considering the system at half-filling (one occupied band), we compute the Zak phase as described in Sec. 1.5

$$\phi = i\int_0^{2\pi} dk\, \langle k_-| \frac{d}{dk} |k_-\rangle = i\int_0^{2\pi} dk(-ix + ix) = 0. \tag{1.54}$$

Remember that the Zak phase in 1D was equivalent to the center of charge of the Wannier function. This implies that, in this case, the center of the charge would be in the bond of the dimer depicted in Fig. 1.3 (a), which coincides with an inversion symmetry center and is the origin of the unit cell. This was the physically expected result. If we cut the model following the unit cell definition of Fig. 1.2, there would not be edge states, since all orbitals would be dimerized.

In the case of $t = 0$, the eigenvalues and eigenstates become

$$\begin{aligned} E_{\pm} &= t' \\ |k_{\pm}\rangle &= \frac{1}{\sqrt{2}}\left(e^{-ikx}, \pm e^{ik(x+1)}\right). \end{aligned} \tag{1.55}$$

Considering the system at half-filling as before, we compute the Zak phase

$$\phi = -i\int_0^{2\pi} dk\, \langle k_-| \frac{d}{dk} |k_-\rangle = \frac{-i}{2}\int_0^{2\pi} dk(i(-x + x + 1)) = \pi. \tag{1.56}$$

In this case, the Wannier charge center is located at the other inversion center, the one in the boundary of the unit cell. Now, if we construct a finite version of the system (following the same definition of the unit cell), then we will cut the system

through a Wannier charge center. Thus, in this case the system will have an edge state in each of the ends of the chain. We could also see it in another way. If the only hopping is t', then, when we make the model finite, there will be two orbitals sitting at the edges, with no tunneling hoppings. Then, the energy of those orbitals is forced to be 0 (the on-site energies are 0) and they will be localized at the edges.

This edge state is protected by symmetry in the following sense: due to inversion symmetry (k to $-k$), the Zak phase is forced to be either 0 or π. Then, if there is a state located at the boundary in the case where the Zak phase is π, we cannot remove the state from there unless we break inversion symmetry.

We are then inclined to label these two phases as trivial ($t' = 0$) and topological ($t = 0$), following that the topological one has a non-trivial Zak phase and edge states. We can, though, change the origin of the cell from one inversion point to the other one, as shown in Fig. 1.3. If we were to compute the Zak phases in both cases now, we would encounter the contrary; $t = 0$ is the trivial case and $t' = 0$ the topological one. Thus, we cannot say that the surface states are topological. However, they are inversion symmetry protected once we fix the definition of a unit cell. Then, if we had an analogous system in a 2D or 3D material, provided that we define the unit cell in a particular way, we could find surface states that are protected symmetry. As we will see later on, this is the case of drumhead states in Nodal line semimetals.

Chapter 2

Topological Quantum Chemistry

In general, the relevant electronic transport properties of a crystal stem from the available electronic states close to the Fermi level. For instance, the metallic behavior of a system can be described from the size of the gap between valence and conduction states. In the last decades, thanks to the development of new techniques that can probe states several electronvolts below the Fermi level, there has been an increased interest in describing the properties of electronic bands as a whole.

There are several ways in which we can define the concept of band. The standard way is in terms of energies; we solve the Schrödinger equation as described in Sec. 1.1 to get both eigenstates and eigenvalues. The eigenvalues will form dense packages that span an energy window. If we label the energies by the corresponding wave vector $\mathbf{k}$ of the Bloch wavefunction, we can define bands as a function that maps $\mathbf{k}$ to energies, $E_n(\mathbf{k})$, where n is the band index.

Considering the symmetry of the crystal we can define the concept of band in an different way. Bloch wavefunctions with wavevector $\mathbf{k}$ will transform under irreducible representations of the symmetry group that leaves $\mathbf{k}$ invariant. Thus, we can define a band by a vector containing the irreducible representations of the Bloch wavefunctions across the BZ. This is the definition of band representation (BR). Note that this is a global description of the band in reciprocal space and, thus, the Bloch wavefunction is not a well suited basis to describe it. Instead, it is preferred to describe it in terms of localized orbitals in real space (Wannier functions). These Wannier functions will encode the symmetries of the system and span the bands, in an analogous way to Bloch wavefunctions.

During his research, Zak *et al* [17–19, 57] developed the formalism of BRs. They discovered a special class of BRs that could not be further decomposed into smaller BRs. They named them elementary band presentations (EBR), and they form a basis for all possible BRs. If we consider time reversal symmetry in addition to the crystalline symmetries, we can extend the concept of EBR to physical EBR (PEBR).

Later, Zak and Michel examined the connectivity of the (P)EBRs[1] and claimed that all of them were connected [16, 58]. However, it has been recently proven that this is not the case [41]. In fact, if a (P)EBR happens to be disconnected[2], then *at least one of the disconnected sets is not a (P)EBR, and cannot come from a set of localized orbitals*. This is one sufficient condition for a set of bands to have a *topologically non-trivial* [13,59–61] gap, which translates into the impossibility to find maximally localized Wannier functions that respect the symmetries of the system. In the course of this research, the theory of Topological Quantum Chemistry (TQC) was developed, which we present in this chapter. This formalism can predict whether a material in a particular space group (SG) can hold topological band gaps by analyzing the symmetry of the bands and how atoms are arranged in a lattice.

Before the introduction of TQC, diagnosing the topology of bands was not an easy task, given the complexity of numerical calculations of topological invariants. In a hallmark paper by Fu and Kane [7], they found a connection between the $\mathcal{Z}_2$ index of 2D TIs and inversion symmetry eigenvalues. It consists on computing the symmetry eigenvalues of the occupied set of bands. In case there is and odd (even) number of negative eigenvalues, the bands will also have an odd (even) topological $\mathcal{Z}_2$ index. This is the first example of a symmetry indicator (SI); a symmetry calculation that diagnoses non-trivial topology. The theory of SIs has been recently generalized by Song *et al* in Ref. [15], where they developed explicit formulas that map symmetry eigenvalues to topological invariants in all non-magnetic SGs. In the same paper, they also tabulate the relation between the topological invariants and the topological systems that are characterized by them (such as mirror Chern insulators or higher order TIs).

The full discussion of TQC, results and applications can be found in a recent series of papers [12, 13, 41, 62–64], with the very recent addition of magnetic space groups (MSG) [65]. In this chapter, we introduce the main concepts and results of the theory by solving two widely known examples, spinless and spinful graphene. We will try to describe the theory in a self-contained way, thus providing a brief, practical explanation of the tools and concepts before using them, such as general group theory and the Bilbao Crystallographic Server [66–69], where all elementary band representations are tabulated.

The chapter is organized as follows: in Sec. 2.1 we review the basic aspects of the hexagonal lattice and present our convention. In Sec. 2.2 we compute the symmetry transformation properties of p orbitals at carbon atom sites of graphene. In Sec. 2.3

[1] The connectivity represents the number of energy bands that are connected together throughout the whole BZ and cannot be disconnected without breaking the crystal symmetry. In a more graphical sense, a set of connected bands is the one that can be drawn without lifting the pencil.

[2] A set of bands are disconnected if there is a direct gap (not necessarily indirect) in the whole BZ that breaks them into different sets.

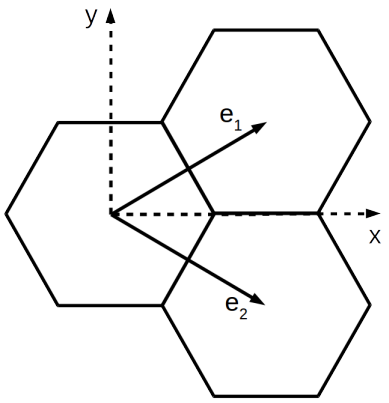

Figure 2.1: Hexagonal lattice on the 6mm (17) wallpaper group.

we show the procedure of induction of a BR. In Sec. 2.4 we compute the little groups for the high-symmetry points in the BZ. In Sec. 2.5 we analyze the cases of graphene, both spinless and spinful. In Sec. 2.6 we analyze the connectivity of the (P)EBRs induced in graphene. Finally, in Section (2.7) we summarize the main results.

2.1 Hexagonal lattice

In this section we review some basic aspects of the hexagonal lattice and present our conventions.

Taking as origin the center of the hexagonal tiles, and the x, y axes as shown in Figure (2.1), the vectors describing the Bravais lattice are:

$$\begin{aligned} \boldsymbol{e}_1 &= \frac{\sqrt{3}}{2}\hat{x} + \frac{1}{2}\hat{y} \\ \boldsymbol{e}_2 &= \frac{\sqrt{3}}{2}\hat{x} - \frac{1}{2}\hat{y}, \end{aligned} \tag{2.1}$$

where we have taken length units such that the norm of the vectors, i.e. the lattice constant, is 1. The generators of the symmetry (point) group of the lattice are $\{C_3|0\}$, $\{C_2|0\}$ and $\{m_{1\bar{1}}|0\}$[3][4]. Their effect on the basis vectors is shown in Fig. 2.2.

[3]Here, by $1\bar{1}$ we denote the mirror plane which is perpendicular to the direction $\boldsymbol{e}_1 - \boldsymbol{e}_2$, in this case, orthogonal to the y axis

[4]We could have used $\{C_3|0\}$ as the generator of all the rotations in this group. However, for reasons that will be clear later, we use a different set of generators.

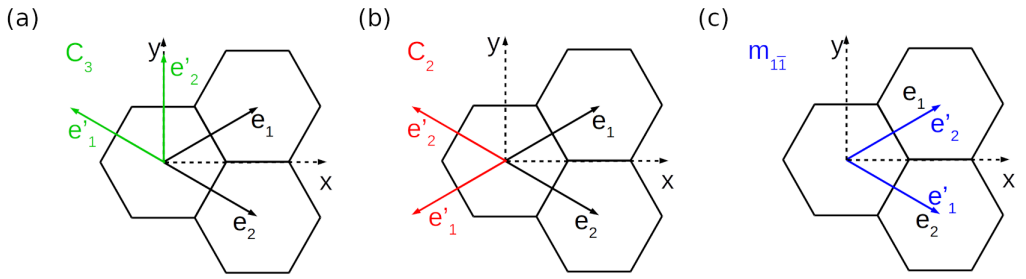

Figure 2.2: Action of the symmetry operators on the basis vectors.

$$\begin{aligned} C_3: &\quad (\boldsymbol{e}_1, \boldsymbol{e}_2) \to (-\boldsymbol{e}_2, \boldsymbol{e}_1 - \boldsymbol{e}_2) \\ C_2: &\quad (\boldsymbol{e}_1, \boldsymbol{e}_2) \to (-\boldsymbol{e}_1, -\boldsymbol{e}_2) \\ m_{1\bar{1}}: &\quad (\boldsymbol{e}_1, \boldsymbol{e}_2) \to (\boldsymbol{e}_2, \boldsymbol{e}_1)\,. \end{aligned} \tag{2.2}$$

Before proceeding, let's define some important concepts[5]:

Definition 1. (Orbit of q). The *orbit of* q is the set of all positions in the same unit cell related to q by the elements of the symmetry group G, i.e., $\text{Orb}_q = \{gq | g \in G\}$.

Definition 2. (Stabilizer group/Site-symmetry group). The *stabilizer group* or *site-symmetry group* of a position q is the set of symmetry operations $g \in G$ that leave q fixed. It is denoted by $G_q = \{g | gq = q\} \subset G$. There are two important points to take into account:

- G_q can include elements $\{R|\vec{r}\}$ with non-zero translations, $\vec{r} \neq 0$.
- Since any site-symmetry group leaves a point invariant, it is isomorphic to a crystallographic point group (there are 32 crystallographic point groups).

Definition 3. (Wyckoff position). A *Wyckoff position* is any position in the unit cell of the crystal. Besides this general definition, there are *special* Wyckoff positions, which are positions that are left invariant by some symmetry operations, such as mirror planes and rotation axis.

Definition 4. (Maximal Wyckoff position). A *Maximal Wyckoff position* is a Wyckoff position whose site-symmetry group is a maximal subgroup of the Point Group of the crystal. In other words, Maximal Wyckoff positions have the larger site-symmetry groups out of all positions in the unit cell. They are the maximal symmetric positions. In real materials, atoms tend to sit in these.

[5]See Apeendix A for a more complete set of definitions.

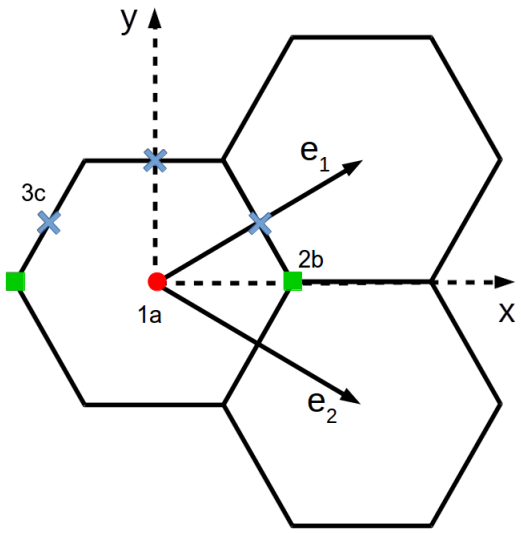

Figure 2.3: Maximal Wyckoff positions for the wallpaper group 17.

Definition 5. (Coset representatives). The *coset representatives* of a site-symmetry group can be defined as the set of elements that generate the orbit of a Wyckoff position.

Now that we have defined the relevant concepts, we can start to analyze the symmetry of different Wyckoff positions. In what follows, we compute some site-symmetry groups for special Wyckoff positions (see Fig. 2.3).

- $q = (\boldsymbol{e}_1 - \boldsymbol{e}_2)/2 = \boldsymbol{e}_y/2$ (blue cross)

$$\begin{aligned} \{m_{11}|0\}: \quad & (\boldsymbol{e}_1, \boldsymbol{e}_2) \to (-\boldsymbol{e}_2, -\boldsymbol{e}_1) \\ & q = \frac{\boldsymbol{e}_1 - \boldsymbol{e}_2}{2} \to \frac{\boldsymbol{e}_1 - \boldsymbol{e}_2}{2} = q \\ \{C_2|1\bar{1}\}: \quad & (\boldsymbol{e}_1, \boldsymbol{e}_2) \to (-\boldsymbol{e}_1, -\boldsymbol{e}_2) + (\boldsymbol{e}_1 - \boldsymbol{e}_2) \\ & q = \frac{\boldsymbol{e}_1 - \boldsymbol{e}_2}{2} \to \frac{-\boldsymbol{e}_1 + \boldsymbol{e}_2}{2} + \boldsymbol{e}_1 - \boldsymbol{e}_2 = \frac{\boldsymbol{e}_1 - \boldsymbol{e}_2}{2} = q. \end{aligned} \tag{2.3}$$

Thus the generators for the site-symmetry group at $q = \frac{\boldsymbol{e}_1 - \boldsymbol{e}_2}{2}$ are the following:

$$\{m_{11}|0\}, \{C_2|1\bar{1}\}, \tag{2.4}$$

which generate a group isomorphic to C_{2v}.

- $q = (\boldsymbol{e}_1 + \boldsymbol{e}_2)/3$ (green square)

$$\begin{aligned} \{m_{1\bar{1}}|0\}: \quad & (\boldsymbol{e}_1, \boldsymbol{e}_2) \to (\boldsymbol{e}_2, \boldsymbol{e}_1) \\ & q = \frac{(\boldsymbol{e}_1 + \boldsymbol{e}_2)}{3} \to \frac{(\boldsymbol{e}_1 + \boldsymbol{e}_2)}{3} = q \\ \{C_3|01\}: \quad & (\boldsymbol{e}_1, \boldsymbol{e}_2) \to (-\boldsymbol{e}_2, \boldsymbol{e}_1 - \boldsymbol{e}_2) + (\boldsymbol{e}_2) \\ & q = \frac{(\boldsymbol{e}_1 + \boldsymbol{e}_2)}{3} \to \frac{-\boldsymbol{e}_2 + \boldsymbol{e}_1 - \boldsymbol{e}_2}{3} + \boldsymbol{e}_2 = \frac{(\boldsymbol{e}_1 + \boldsymbol{e}_2)}{3} = q. \end{aligned} \tag{2.5}$$

In this case, the site-symmetry group is isomorphic to C_{3v}[6].

- $q = 0$ (red dot)

In this case all elements in the point group leave this point invariant, and the stabilizer group at $q = 0$ is isomorphic to the point group C_{6v}.

- $q = x(\boldsymbol{e}_1 + \boldsymbol{e}_2)\,,\ x \in (0, \frac{1}{3})$ (*line connecting the dot and the square*)

In this case we consider the line that goes from the origin to one of the vertices of the hexagon. This set of points is left unchanged by the mirror plane $m_{1\bar{1}}$. The position $q = (x, x)$ interpolates between the origin and the corner of the lattice. Note that the element $m_{1\bar{1}}$ is common to the site-symmetry groups of the origin and the vertex of the hexagon.

2.1.1 Orbits for the different q points

Let's compute now the orbits of the points we have just discussed. For this, we only need to consider symmetry operations that do not belong to the site-symmetry group. However, there is an ambiguity as to which of them to choose, because there are more than necessary[7]. The ones we choose are the *coset representatives*.[8]

[6] See Appendix B

[7] Imagine that our full group has 15 elements and that our site-symmetry group has 5. Then, the orbit of that point will have 15/5=3 positions, i.e., we need 3 out of the 15-5=10 remaining elements to generate the orbit. The other 7 elements will generate the same positions in the orbit.

[8] See Apeendix A for a more formal definition.

- $q = (\boldsymbol{e}_1 - \boldsymbol{e}_2)/2 = \boldsymbol{e}_y/2$

  Since the site-symmetry group for this point contains as generators the mirror plane and the C_2 axis, we will use the C_3 axis to generate the orbit:

$$\begin{aligned} \{C_3^+|0\}(\frac{1}{2}, -\frac{1}{2}) &= (-\frac{1}{2}, 0) \\ \{C_3^-|0\}(\frac{1}{2}, -\frac{1}{2}) &= (0, \frac{1}{2}). \end{aligned} \tag{2.6}$$

  So the orbit of q is composed by 3 points. We call these the 3c Wyckoff positions.

- $q = (\boldsymbol{e}_1 + \boldsymbol{e}_2)/3$

  In this case, the site-symmetry group contains the mirror plane and the C_3 axis, so we need to consider the C_2 axis:

$$\{C_2|0\}(\frac{1}{3}, \frac{1}{3}) = (-\frac{1}{3}, -\frac{1}{3}). \tag{2.7}$$

  These positions are labeled as 2b Wyckoff positions.

- $q = 0$

  Since the site-symmetry group at this point is the whole point group, there are no other position in its orbit. This position is denoted as 1a.

- $q = x\,(\boldsymbol{e}_1 + \boldsymbol{e}_2)$

  The site symmetry group for this set of points contains just the mirror plane, so any combination of the axes (the C_2 and C_3 axes) will generate a position in the orbit. In this case, there will be 6 positions in the orbit, which coincide with the ones generated by the C_6 axis.

The site-symmetry groups at any two points in the orbit of q are conjugate to each other and, hence, isomorphic[9]. We are interested in the maximal Wyckoff positions,

[9] See appendix B

which are the positions whose site-symmetry group is a maximal subgroup of the full point group. Thus, as C_{6v} has only 3 maximal subgroups, C_{6v}, C_{3v}, and C_{2v}, the maximal Wyckoff positions will be the ones whose site-symmetry group is isomorphic to one of these. As we showed, the site-symmetry groups for the positions 1a, 2b, and 3c are isomorphic to the maximal subgroups of C_{6v}[10]. However, the last position for which we computed the site-symmetry group and the orbit is not a maximal Wyckoff position since its site-symmetry group is not maximal.

2.1.2 Adding orbitals

To respect crystal symmetry, when we add an orbital at a Wyckoff position, we have to add the same orbital at all positions in the orbit. These orbitals, once placed in their positions, will transform under a representation of the site-symmetry group. Then, if we know the representation under which the orbitals in particular Wyckoff position transform, we can get the representation of the orbitals in the rest of the orbit by applying the following procedure.

Let ρ_{q_1} be the representation[11] under which a set of orbitals in the position q_1 transform, h an element of the site-symmetry group G_{q_1} and g_α one of the coset representatives. Then

$$\begin{aligned} &hq_1 = q_1, \quad g_\alpha q_1 = q_\alpha \rightarrow q_1 = g_\alpha^{-1} q_\alpha \\ &g_\alpha h g_\alpha^{-1} q_\alpha = g_\alpha h q_1 = g_\alpha q_1 = q_\alpha. \end{aligned} \tag{2.8}$$

Thus $g_\alpha h g_\alpha^{-1}$ belongs to the site-symmetry group of q_α. Then, if we know ρ_{q_1} we also know that $\rho_{q_\alpha}(h) = \rho_{q_1}(g_\alpha^{-1} h g_\alpha)$[12]. This is precisely the definition of conjugate groups, which proves that the site-symmetry groups of all Wyckoff positions in the same orbit are conjugate to each other and, thus, isomorphic.

So far, we have been discussing about placing atomic orbitals. However, it is more accurate to speak of *crystal orbitals*. Atomic orbitals transform under irreducible representations of the full rotation group $O(3)$[13]. When placed on a crystal environment,

[10] One can see the reason behind Wyckoff position naming; the number indicates multiplicity (number of elements in the orbit) while the letters, in alphabetical order, order the positions form more symmetric to less.

[11] A representation assigns a square matrix or operator $\rho(g)$ to each element of the group, in such a way that when we compose two elements the product of the two matrices is equal to the matrix assigned to the resulting element, i.e., $\rho(g_1)\rho(g_2) = \rho(g_1 g_2)$.

[12] See Appendix C.

[13] To be precise, the full rotation group would be SO(3), because rotations have determinant 1. however, this does not cover all crystalline symmetry operations, since we are leaving out both mirrors, inversion, and combinations of these. If we add these two, i.e., $\mathrm{SO}(3) \oplus \mathrm{I} \otimes \mathrm{SO}(3)$ what we get is the full 3D symmetry group, O(3).

the symmetry is reduced and atomic orbitals are not orthogonal anymore. Then, one must consider crystal orbitals, which transform under irreducible representations of the site-symmetry group, a subgroup of the full rotation group. In general, these crystal orbitals will be formed by a linear combination of atomic orbitals that transform in the same way now that we reduced the symmetry group.

Crystal orbitals can be described by a set of Wannier states (highly localized as explained in Sec. 1.4), one per orbital, that transform under an irreducible representation of the site-symmetry group [59, 60].

2.2 Adding p orbitals at 2b positions

In this section, we will study how p orbitals transform when placed in an environment with a reduced amount of symmetry. In this case, at Wyckoff 2b position of the space-group P6mm (the wallpaper group 17).

2.2.1 Spinless p orbitals

Angular momentum $l = 1$ orbitals or, as the are commonlly known, p orbitals, are a basis for the 3-dimensional ($l = 1$) or *vector* (V) representation of O(3). The site-symmetry group for Wyckoff 2b is not the whole rotation group O(3) but just one of its subgroups, namely C_{3v}. Thus, we want to analyze how p orbitals transform under the point group C_{3v}. Mathematically, we want to express the vector representation of O(3) in terms of irreducible representations of C_{3v}, a process that is known as *subduction*. In mathematical terms, if we denote by V the representation of O(3) under which p orbitals transform, we want to find the corresponding subduced representation $V \downarrow G_{q^{2b}} \equiv V \downarrow C_{3v}$ (the down arrow represents the operation of subduction).

To determine how the three orbitals p_x, p_y and p_z transform under the symmetries of the group C_{3v} we only need to analyze the effect of the generators, since the rest of the elements can be obtained by matrix multiplication (group element composition). The action of the generators is shown in Table 2.1.

C_{3v}	E	C_3	$m_{1\bar{1}}$
p_x	p_x	$cp_x + sp_y$	p_x
p_y	p_y	$cp_y - sp_x$	$-p_y$
p_z	p_z	p_z	p_z

Table 2.1: Effect of C_{3v} group elements on p orbitals.

where c, s stand for $cos(\frac{2\pi}{3})$, $sin(\frac{2\pi}{3})$. We can now construct the matrices of the

C_{3v}	E	$C_3^{\pm}$	m_i
V	3	0	1
ρ^{p_z}	1	1	1
ρ^{p_x,p_y}	2	-1	0
A_1	1	1	1
A_2	1	1	-1
E	2	-1	0

Table 2.2: Table of characters of the group C_{3v}. The first row gives the traces of the matrices for the vector representation, while the next two correspond to the blocks formed by p_z and p_x, p_y. Under the solid line we have written the characters of the irreps (irreducible representations) of C_{3v}.

representation[14]:

$$V(E)=\begin{pmatrix}1&0&0\\0&1&0\\0&0&1\end{pmatrix},\ V(m_{1\bar{1}})=\begin{pmatrix}1&0&0\\0&-1&0\\0&0&1\end{pmatrix},\ V(C_3)=\begin{pmatrix}cos(\frac{2\pi}{3})&sin(\frac{2\pi}{3})&0\\-sin(\frac{2\pi}{3})&cos(\frac{2\pi}{3})&0\\0&0&1\end{pmatrix}. \tag{2.9}$$

It is important to note that *all* the symmetry elements of the group, not just the generators, must appear in the character table. To save space, the elements that belong to the class are written together, since they the same traces. In this case, our group has 6 elements (E, $C_3^{\pm}$ and three mirror planes m_i), but there are only 3 different classes. In this case, the three classes correspond to the identity, the C_3 rotations and the mirror planes.

Although there is an algorithmic method[15] to compute how a group representation decomposes into irreducible representations (irreps) of one of its subgroups [43], in this case it is not hard to see by simple inspection that $V = A_1(p_z) + E(p_x, p_y)$. This is an example where an irreducible representation of $O(3)$ becomes reducible when restricted to a subgroup, that is, when the symmetry is reduced.

So far, we have been working with single-valued or spinless group representations, representations of subgroups of $O(3)$. If we want to take spin into account, we have

[14]These matrices correspond to the basis of p_x, p_y, p_z. There is another convention where we change $(p_x, p_y) \to (p_x - ip_y, p_x + ip_y)$ so that the vectors in this new basis are eigenstates of L_z and $\rho(C_3)$ becomes diagonal, $\rho(C_3) = diag(e^{-2\pi i/3}, e^{2\pi i/3}, 0))$. On this basis the matrix for the mirror plane is non-diagonal, $(\rho(m_{1\bar{1}}) = \begin{pmatrix}0&1&0\\1&0&0\\0&0&1\end{pmatrix}$. The traces are invariant under such transformations, so the character of the representation stays the same.

[15]See the explanation around Eq. (2.17) below.

to extend our methods to the so called "double-valued" representations. The reason is that spin transforms under $SU(2)$, which is a different group[16].

2.2.2 Spinful p orbitals

We will now focus on p_z orbitals with spin up and down, also at the Wyckoff 2b position. Angular momentum eigenstates rotate with the unitary operator $\exp(i\boldsymbol{n}\cdot\boldsymbol{J}\Omega)$, where $\boldsymbol{J}$ is the total angular momentum operator, $\boldsymbol{n}$ is a unit vector in the direction of the rotation axis and Ω is the rotation angle. Representations of SO(3) correspond to integer total angular momentum. However, for half-odd angular momentum, a rotation of 2π gives a minus sign instead of the identity. As mentioned earlier, this reflects the fact that half-odd angular momentum states transform under representations of $SU(2)$. Following the procedure described in the previous section, we construct the representation for spin up and down p_z orbitals.

For a $\frac{2\pi}{3}$ rotation around the C_3 axis in the z direction, we have $e^{i\frac{\pi}{3}}$ for the spin-up state ($s_z=\frac{1}{2}$) and $e^{-i\frac{\pi}{3}}$ for spin down($s_z=-\frac{1}{2}$)[17]. We can write this representation in a more compact way as $\rho(C_3)=\exp\left(i\frac{\pi}{3}\sigma_z\right)$ where σ_z is the third Pauli matrix. We can think of a mirror plane as a π degree rotation around an axis orthogonal to the mirror plane followed by inversion[18]. Spin rotates, but inversion has no effect on it, so, for spin states, a mirror plane is equivalent to a π degree rotation around the direction orthogonal to the mirror. In this case, the mirror is perpendicular to the y axis. Thus the representation for the mirror plane is $\rho(m_{1\bar{1}})=\exp\left(i\frac{\pi}{2}\sigma_y\right)=i\sigma_y$. The matrices for the generators will then be:

$$\rho(C_3)=\begin{pmatrix} e^{i\frac{\pi}{3}} & 0 \\ 0 & e^{-i\frac{\pi}{3}} \end{pmatrix}, \quad \rho(m_{1\bar{1}})=\begin{pmatrix} 0 & 1 \\ -1 & 0 \end{pmatrix}. \tag{2.10}$$

Now we can write the character of this representation by computing the traces, and compare them to the irreducible representations of the double-group. Remember that for double groups a rotation of 2π is equal to minus the identity, so the number of elements doubles. For each element of the ordinary group we have to include the result of composing the element with a 2π rotation, namely $\bar{E}$.

We can see that the representation under which our orbitals transform is an irreducible representation ($\bar{\Gamma}_6$) of the site-symmetry double-group. The other two spinful irreps are total angular momentum $\frac{3}{2}$ representations. More precisely, the basis for

[16]In fact, $SU(2)$ is the universal covering of the (proper) rotation group $SO(3)$. Above we argued that the appropriate group to describe all symmetry operations is O(3), not SO(3). Then, you may wonder why we consider SO(3) when discussing double-valued representations. Since spin is not affected by inversion symmetry we can restrict ourselves to SO(3).

[17]Remember that p_z orbitals have $L_z=0$

[18]In this case, as the π degree rotation and inversion commute, we can apply them in any order.

C_{3v}	E	$C_3^{\pm}$	m_i	$\bar{E}$	$\bar{C}_3^{\pm}$	$\bar{m}_i$
ρ	2	1	0	-2	-1	0
$\bar{\Gamma}_4$	1	-1	-i	-1	1	i
$\bar{\Gamma}_5$	1	-1	i	-1	1	-i
$\bar{\Gamma}_6$	2	1	0	-2	-1	0

Table 2.3: Table of characters of the group C_{3v}.

$\bar{\Gamma}_5$ is $\left|\frac{3}{2}\right\rangle + i\left|-\frac{3}{2}\right\rangle$, while the basis for $\bar{\Gamma}_4$ is $\left|\frac{3}{2}\right\rangle - i\left|-\frac{3}{2}\right\rangle$, made from p_x, p_y spinful orbitals[19] [62, 64]. The remaining combinations of p_x, p_y spinful orbitals, like p_z, transform under $\bar{\Gamma}_6$. [20].

We have obtained the representations under which both spinless and spinful p_z orbitals transform under C_{3v} group, which is the site-symmetry group of the Wyckoff 2b position, the sites where carbon atoms lie in graphene. In what follows, we will compute the band representations induced from these orbitals.

2.3 Inducing a Band Representation

From the Wannier states $W_{i\alpha}(\mathbf{r} - \boldsymbol{t}_\mu)$[21] we define Fourier transformed Wannier states (Bloch waves):

$$a_{i\alpha}(\mathbf{k}, \mathbf{r}) = \frac{1}{\sqrt{N}} \sum_{\mu} e^{i\mathbf{k}\boldsymbol{t}_\mu} W_{i\alpha}(\mathbf{r} - \boldsymbol{t}_\mu), \tag{2.11}$$

where $\boldsymbol{t}_\mu$ are all vectors in the Bravais lattice. We have gone from a $n \times n_q \times N$ (n positions in the orbit times n_q orbitals per site in the orbit times N cells in the crystal) dimensional basis to a finite $n \times n_q$ basis for each $\mathbf{k}$. This corresponds to $n \times n_q$ bands. These functions are a set of Bloch waves that span bands in reciprocal space. We want to compute under which irreducible representations transform these Bloch waves, since that is the basis to induce a Band Representation.

Here is the power of this theory: even if we don't know the actual form of the Hamiltonian, if it complies with the symmetries of the crystal, the eigenstates will transform under a certain representation of the space group, what is called a band representation [57]. Thus, we do not need to know the very specific energy spectrum

[19] $\left|\frac{3}{2}\right\rangle = (|p_x\rangle + i\,|p_y\rangle) \otimes |\uparrow\rangle$, $\left|-\frac{3}{2}\right\rangle = (|p_x\rangle - i\,|p_y\rangle) \otimes |\downarrow\rangle$

[20] The combinations are $(|p_x\rangle + i\,|p_y\rangle) \otimes |\downarrow\rangle$ and $(|p_x\rangle - i\,|p_y\rangle) \otimes |\uparrow\rangle$.

[21] Here, the i index labels the orbital (s, p, d...) while α labels the position on the orbit (1, 2, 3...). The last index is t_μ, which labels the cell of the crystal. This way we have labeled all orbitals in our crystal. We can see here how there is one Wannier function per orbital.

to make predictions. Predictions that range from crossings at high symmetry $\mathbf{k}$ points or, using the mapping between symmetry and topology, to prediction of topological phases..

We now proceed to compute $a_{i\alpha}(\mathbf{k},\mathbf{r})$ functions' transformation properties under any element h of the full group G. We can derive it from Wannier functions' transformation properties[22]:

$$[\rho_G(h)]_{j\beta,i\alpha}W_{j\beta}(\mathbf{r}-\boldsymbol{t}_\mu)=[\rho(g_{\beta\alpha})]_{ji}W_{j\beta}(\mathbf{r}-R\boldsymbol{t}_\mu-\boldsymbol{t}_{\beta\alpha}). \tag{2.12}$$

Then, using Eq. (2.11):

$$\begin{aligned}[\rho_G(h)]_{j\beta,i\alpha}a_{j\beta}(\mathbf{k},\mathbf{r}) =&\frac{1}{\sqrt{N}}\sum_\mu e^{i\mathbf{k}\cdot\boldsymbol{t}_\mu}[\rho_G(h)]_{j\beta,i\alpha}W_{j\beta}(\mathbf{r}-\boldsymbol{t}_\mu)\\ =&\frac{1}{\sqrt{N}}\sum_\mu e^{i\mathbf{k}\cdot\boldsymbol{t}_\mu}[\rho(g_{\beta\alpha})]_{ji}W_{j\beta}(\mathbf{r}-R\boldsymbol{t}_\mu-\boldsymbol{t}_{\beta\alpha})\\ =&e^{-iR\mathbf{k}\cdot\boldsymbol{t}_{\beta\alpha}}[\rho(g_{\beta\alpha})]_{ji}\frac{1}{\sqrt{N}}\sum_\mu e^{i(R\mathbf{k})\cdot(R\boldsymbol{t}_\mu+\vec{\boldsymbol{t}}_{\beta\alpha})}W_{j\beta}(\mathbf{r}-R\boldsymbol{t}_\mu-\boldsymbol{t}_{\beta\alpha})\\ =&e^{-iR\mathbf{k}\cdot\boldsymbol{t}_{\beta\alpha}}[\rho(g_{\beta\alpha})]_{ji}a_{j\beta}(R\mathbf{k},\mathbf{r}),\end{aligned} \tag{2.13}$$

where $g_{\beta\alpha}=g_\beta^{-1}\{E|-\boldsymbol{t}_{\beta\alpha}\}hg_\alpha\in G_q$[23]. For each value of $\mathbf{k}$ on the reciprocal space, this expression tells us how the Bloch waves transform. This is what we call a *Band Representation*.

The representation $\rho_G(h)$ is a $(n\times n_q)$ dimensional unitary square matrix at each pair of ($\mathbf{k}$, $\mathbf{k}'$) vectors. The only non-zero blocks are the ($\mathbf{k}$, $\mathbf{k}'=R\mathbf{k}$), as can be seen from the above equation, since it relates the $a(\mathbf{k})$ state to the $a(R\mathbf{k})$ one. This block can be written as:

$$[\rho_G^{\mathbf{k}}(h)]_{j\beta,i\alpha}=e^{-iR\mathbf{k}\cdot\boldsymbol{t}_{\beta\alpha}}[\rho(g_\beta^{-1}\{E|-\boldsymbol{t}_{\beta\alpha}\}hg_\alpha)]_{ji}. \tag{2.14}$$

2.4 Little groups at k-points in the first BZ

Let's denote by $G_{\mathbf{k}}$ the *little group* of a $\mathbf{k}$-point in the reciprocal space. We will see that the most interesting $\mathbf{k}$-points will be the ones with highest symmetry but, for the time being, $\mathbf{k}$ can have any value in the first BZ. The character of the band representation is the set of traces of the $[\rho_G^{\mathbf{k}}(h)]_{j\beta,i\alpha}$ matrices for each h, i.e.,

[22] See Appendix C for a complete derivation of the transformation properties of Wannier functions.
[23] See Appendix C for further details.

$$\chi^{\mathbf{k}}_G(h) = [\rho^{\mathbf{k}}_G(h)]_{i\alpha,i\alpha} = \sum_{\alpha,i} e^{-iR\mathbf{k}\cdot\boldsymbol{t}_{\alpha\alpha}}[\rho(g)]_{ii} = \sum_{\alpha} e^{-iR\mathbf{k}\cdot\boldsymbol{t}_{\alpha\alpha}}\chi^{\mathbf{k}}(g_\alpha^{-1}\{E|-\boldsymbol{t}_{\alpha\alpha}\}hg_\alpha). \tag{2.15}$$

At a particular **k**-point, Bloch waves transform under representations of its little group $G_{\mathbf{k}}$. If we have the character of the representation under which they transform at any **k**-point in the first BZ, we can *subduce* the full representation, from the full group G to the little group, $G_{\mathbf{k}}$[24]. Once we do this, we know the *small representation* under which Bloch waves transform at each **k**-point. We can now ask ourselves if this subduced representation is reducible. In general, it will be reducible, and we will be able to express our representation as a sum of irreps of the little group[25]. In mathematical terms, we want to construct:

$$(\rho \uparrow G) \downarrow G_{\mathbf{k}} \approxeq \bigoplus_i m_i \sigma_i^{\mathbf{k}}, \tag{2.16}$$

where $\sigma_i^{\mathbf{k}}$ are irreps of the little group $G_{\mathbf{k}}$ and the m_i are the multiplicities of the representation, i.e., how many times that irrep appears in the decomposition. This number can be easily obtained using the so called *magic formula* [43]:

$$m_i = \frac{1}{n}\sum_h \bar{\chi}_i(h)\chi^{\mathbf{k}}(h), \tag{2.17}$$

where n is the number of elements in the group (order of the group), h are the elements of the group, the bar indicates complex conjugate, χ_i denote the characters of the irrep and $\chi^{\mathbf{k}}$ is the character of the representation we want to decompose. We have then shown that some properties of the bands are inherited from the way orbitals transform in real space. Out of all the **k**-points inside the BZ, not all of them provide us with the same information; points in which the small group is trivial give trivial information. This is why we can encode the Band Representation by looking at the transformation properties in a finite set of highly symmetric **k**-points.

2.5 Example of band representation

In this section we will explicitly compute the band representation arising from spinless and spinful p_z orbitals in graphene. We will see how, even if we are not using any

[24]This is a rigorous mathematical procedure, common in group theory. In practice, it is like constructing the table of characters for the big group and remove the elements that do not belong to the little group.

[25]Here, the term "sum" has to be understood as sum of representations. For example, a 1-dimensional representation "plus" a 2-dimensional representation gives a 3-dimensional one.

specific Hamiltonian, we can predict that spinless graphene has Dirac cones, while spinful does not, and that spinful graphene is always topological.

2.5.1 Spinful graphene

Graphene is described by carbon atoms sitting at 2b Wyckoff positions, with coordinates $q_1 = \left(\frac{1}{3}, \frac{1}{3}\right)$ and $q_2 = \left(-\frac{1}{3}, -\frac{1}{3}\right)$. The site-symmetry group of this site is isomorphic to C_{3v} and we choose the representation of the generators to be (see Sec. 2.2.2):

$$\rho(C_3) = \exp\left(i\frac{\pi}{3}\sigma_z\right), \quad \rho(m_{1\bar{1}}) = i\sigma_x. \tag{2.18}$$

The coset representatives are chosen to be $g_1 = \{E|0\}$, $g_2 = \{C_2|0\}$. The first thing we need to compute are the $\boldsymbol{t}_{\beta\alpha}$. The action of an element of the full group will have the following form:

$$hq_\alpha = \{E|\boldsymbol{t}_{\beta\alpha}\}q_\beta, \quad g_\beta^{-1}\{E|-\boldsymbol{t}_{\beta\alpha}\}hg_\alpha q_1 = q_1 \equiv gq_1 = q_1, \tag{2.19}$$

where the vector $\boldsymbol{t}_{\beta\alpha}$ represents the possibility of an element to take some Wyckoff away to another cell. It can be shown that (see Appendix C):

$$\boldsymbol{t}_{\beta\alpha} = hq_\alpha - q_\beta. \tag{2.20}$$

We will use this last equation to compute the $\vec{t}_{\beta\alpha}$ for the different generators.

- $\{C_3|0\}$

$$\begin{aligned}
&\boldsymbol{t}_{\beta\alpha} = hq_\alpha - q_\beta \\
&\boldsymbol{t}_{11} = \{C_3|0\}\left(\frac{1}{3}, \frac{1}{3}\right) - \left(\frac{1}{3}, \frac{1}{3}\right) = \left(\frac{1}{3}, -\frac{2}{3}\right) - \left(\frac{1}{3}, \frac{1}{3}\right) = (0, -1) \\
&\boldsymbol{t}_{22} = \{C_3|0\}\left(-\frac{1}{3}, -\frac{1}{3}\right) - \left(-\frac{1}{3}, -\frac{1}{3}\right) = \left(-\frac{1}{3}, \frac{2}{3}\right) + \left(\frac{1}{3}, \frac{1}{3}\right) = (0, 1)\,.
\end{aligned} \tag{2.21}$$

Once determined that $\boldsymbol{t}_{\beta 1}$ exists for a certain β, there is no other β for which $\boldsymbol{t}_{\beta\alpha}$ makes sense. We can see in Fig. 2.4 how $\boldsymbol{t}_{11}$ connects two q_1 positions in different cells, due to the action of the C_3 axis. But this C_3 axis *does not connect a position q_1 to a position q_2*, so $\boldsymbol{t}_{21}$ does not exist. What this really means is that when constructing the representation for the C_3 axis with indices $(j\beta, i\alpha)$, the block with $\alpha = 1$, $\beta = 2$ will be full of zeroes, while the block with

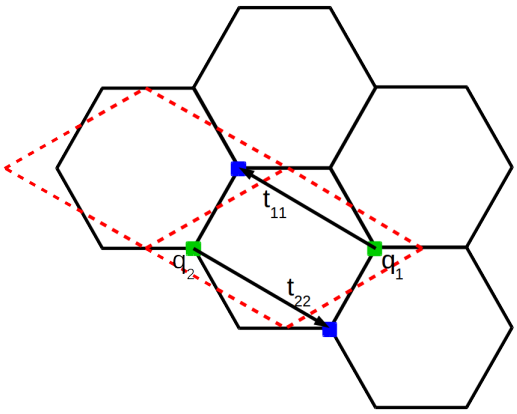

Figure 2.4: Action of the C_3 axis on Wyckoff positions. In green, the original positions. In blue, the new position after the action of the rotation. In red, the unit cells.

$\alpha = 1$, $\beta = 1$ will be the representation of some element of the site-symmetry group of position q_1. But this element can only be the one we obtained before, $g = g_\beta^{-1}\{E|-\boldsymbol{t}_{\beta\alpha}\}hg_\alpha$. We can use this equation to find this g element:

$$\begin{aligned} g_{11} &= \{E|0\}^{-1}\{E|-\boldsymbol{t}_{11}\}\{C_3|0\}\{E|0\} = \{E|-0\bar{1}\}\{C_3|0\} = \{C_3|01\} \\ g_{22} &= \{C_2|0\}^{-1}\{E|-\boldsymbol{t}_{22}\}\{C_3|0\}\{C_2|0\} = \{C_3|01\}. \end{aligned} \tag{2.22}$$

So we can construct now the representation of this element. We will write it by blocks, each block defined by coordinates (β, α) being a matrix with indices (i, j). Using Eq. (2.14):

$$[\rho_G^{\mathbf{k}}(\{C_3|0\})]_{j\beta,i\alpha} = \begin{pmatrix} e^{i(C_3\mathbf{k})\boldsymbol{e}_2} & 0 \\ 0 & e^{-i(C_3\mathbf{k})\boldsymbol{e}_2} \end{pmatrix} \otimes e^{i\frac{\pi}{3}\sigma_z} = \begin{pmatrix} e^{i(C_3\mathbf{k})\boldsymbol{e}_2}e^{i\frac{\pi}{3}\sigma_z} & 0 \\ 0 & e^{-i(C_3\mathbf{k})\boldsymbol{e}_2}e^{i\frac{\pi}{3}\sigma_z} \end{pmatrix}, \tag{2.23}$$

where the product is tensor product.

- $\{m_{1\bar{1}}|0\}$

Following the same procedure as before:

$$\begin{aligned}\boldsymbol{t}_{11} &= \{m_{1\bar{1}}|0\}\left(\frac{1}{3},\frac{1}{3}\right) - \left(\frac{1}{3},\frac{1}{3}\right) = (0,0)\\ \boldsymbol{t}_{22} &= \{m_{1\bar{1}}|0\}\left(-\frac{1}{3},-\frac{1}{3}\right) - \left(-\frac{1}{3},-\frac{1}{3}\right) = (0,0).\end{aligned} \tag{2.24}$$

The no-null blocks will be diagonal and, in this case, both $\boldsymbol{t}_{\alpha\beta}$ are zero. Let's find the elements g:

$$\begin{aligned}g_{11} &= \{E|0\}^{-1}\{E|-\boldsymbol{t}_{11}\}\{m_{1\bar{1}}|0\}\{E|0\} = \{E|0\}\{m_{1\bar{1}}|0\} = \{m_{1\bar{1}}|0\}\\ g_{22} &= \{C_2|0\}^{-1}\{E|-\boldsymbol{t}_{22}\}\{m_{1\bar{1}}|0\}\{C_2|0\} = \{C_2|0\}^{-1}\{E|-\vec{t}_{22}\}\{\bar{C}_2|0\}\{m_{1\bar{1}}|0\} = \{\bar{m}_{1\bar{1}}|0\},\end{aligned} \tag{2.25}$$

where in the last step we have used the commutation relation of the C_2 axis and the mirror plane, but notice that, in double groups, $C_2^2 = \bar{E} = -E \neq E$. We are able to build the representation for this element:

$$[\rho_G^{\mathbf{k}}(\{m_{1\bar{1}}|0\})]_{j\beta,i\alpha} = \begin{pmatrix}1 & 0\\ 0 & 1\end{pmatrix} \otimes i\sigma_x = \begin{pmatrix}i\sigma_x & 0\\ 0 & -i\sigma_x\end{pmatrix}. \tag{2.26}$$

- $\{C_2|0\}$

So far, we have found that the induced representations are diagonal, giving us the feeling that it could be reducible. This has happened because the elements for which we have been constructing the representation were in the site-symmetry group, or differ by an integer lattice translation. However, we will find now that, since C_2 is not contained in the site-symmetry group, the representation will be off-diagonal, and, thus, will make this representation irreducible. Let's compute the representation for C_2.

$$\begin{aligned}\boldsymbol{t}_{21} &= \{C_2|0\}\left(\frac{1}{3},\frac{1}{3}\right) - \left(-\frac{1}{3},-\frac{1}{3}\right) = (0,0)\\ \boldsymbol{t}_{12} &= \{C_2|0\}\left(-\frac{1}{3},-\frac{1}{3}\right) - \left(\frac{1}{3},\frac{1}{3}\right) = (0,0).\end{aligned} \tag{2.27}$$

We see that, in this case, the non-vanishing blocks are the ones with coordinates $\alpha = 1$, $\beta = 2$ and $\alpha = 2$, $\beta = 1$. So the representation will be off-diagonal. Let's compute the elements g:

$$\begin{aligned} g_{21} &= \{C_2|0\}^{-1}\{E|-\boldsymbol{t}_{21}\}\{C_2|0\}\{E|0\} = \{E|0\} \\ g_{12} &= \{E|0\}^{-1}\{E|-\boldsymbol{t}_{12}\}\{C_2|0\}\{C_2|0\} = \{\bar{E}|0\}. \end{aligned} \tag{2.28}$$

So, the representation for this element is:

$$[\rho_G^{\mathbf{k}}(\{C_2|0\})]_{j\beta,i\alpha} = \begin{pmatrix} 0 & -I \\ I & 0 \end{pmatrix} = -i\sigma_y \otimes \sigma_0, \tag{2.29}$$

where I is the 2x2 identity.

2.5.2 Spinless graphene

Having determined the spinful representation, it is easy to see what the spinless representation is, by just getting rid of the spin degree of freedom. Now, the 4x4 matrices are 2x2 matrices:

$$[\rho_G^{\mathbf{k}}(\{C_3|0\})]_{\beta\alpha} = \begin{pmatrix} e^{i(C_3\mathbf{k})\cdot\boldsymbol{e}_2} & 0 \\ 0 & e^{-i(C_3\mathbf{k})\cdot\boldsymbol{e}_2}, \end{pmatrix} \tag{2.30}$$

$$[\rho_G^{\mathbf{k}}(\{m_{1\bar{1}}|0\})]_{\beta\alpha} = \begin{pmatrix} 1 & 0 \\ 0 & 1 \end{pmatrix}, \tag{2.31}$$

$$[\rho_G^{\mathbf{k}}(\{C_2|0\})]_{\beta\alpha} = \begin{pmatrix} 0 & -1 \\ 1 & 0 \end{pmatrix}. \tag{2.32}$$

Now that we have the representation under which Bloch waves transform at any $\mathbf{k}$-point, we can see which symmetry enforced degeneracies we will have, by looking at the dimension of the subduced representation at different $\mathbf{k}$-points. Let's see what happens at the $\mathbf{k} = (\frac{1}{3}, \frac{2}{3})$ point.

The little group of the $\mathbf{k} = (\frac{1}{3}, \frac{2}{3})$ point is formed by a C_3 axis and a mirror plane (isomorph to C_{3v}), but the mirror plane is not $m_{1\bar{1}}$ but m_{11}. We can compute explicitly the representation of this mirror plane to obtain the character to define its representation, but it is not necessary. Following the argument we gave before, the representation of an element that is not part of the site-symmetry group is off diagonal when we induce it, since it mixes the two positions. Thus, the trace of the representation of the mirror plane m_{11} will be 0. Because the C_3 axis is in the little group, $(C_3\mathbf{k})\boldsymbol{e}_2 = \boldsymbol{K}\cdot\boldsymbol{e}_2$ and we can compute the trace of the C_3 axis matrix: $[\rho_G^{\mathbf{k}}(\{C_3|0\})]_{\alpha\alpha} = 2\cos(\boldsymbol{K}\cdot\boldsymbol{e}_2) = 2\cos\left(\frac{4\pi}{3}\right) = -1$. So our representation has the following character in C_{3v}:

C_{3v}	E	$C_3^{\pm}$	m_i
$\rho_G^{\mathbf{k}}$	2	-1	0
A_1	1	1	1
A_2	1	1	-1
E	2	-1	0

Table 2.4: Table of characters of the group C_{3v}.

C_{6v}	E	$C_3^{\pm}$	$C_2, \bar{C}_2$	$C_6^{\pm}$	m_{11}	$m_{1\bar{1}}$	$\bar{E}$	$\bar{C}_3^{\pm}$	$\bar{C}_6^{\pm}$
ρ_G^{Γ}	4	2	0	0	0	0	-4	-2	0
$\bar{\Gamma}_7$	2	1	0	$-\sqrt{3}$	0	0	-2	-1	$\sqrt{3}$
$\bar{\Gamma}_8$	2	1	0	$\sqrt{3}$	0	0	-2	-1	$-\sqrt{3}$
$\bar{\Gamma}_9$	2	-2	0	0	0	0	-2	2	0

Table 2.5: Table of characters of the group C_{6v}.

We see that this representation is already an irreducible representation of C_{3v}, i.e., there will be a band crossing at the **k**-point of the two bands that are doubly degenerate due to trivial spin degeneracy. And this crossing is protected by symmetry. We have found the famous Dirac cones of spinless graphene.

2.6 Subducing the Band Representation

We will focus now on spinful graphene, since it is the one that can display topological properties. We will subduce now the representation at different, high-symmetry points in the first Brillouin Zone, which are Γ, K *and* M (see Fig. 2.5).

2.6.1 Γ point

The little group at this point is the full point group, C_{6v}. This group contains C_3 axis, C_2 axis, planes and C_6 axis also. We have not computed the representation for the C_6 axis, but we can obtain it from the representations of 2 and C_3 axis by combining them (a 6 axis is a C_2 axis minus a C_3 axis). We can see the character of the representation in Table (2.5).

Just by inspection of the table we get that the representation is reducible, in fact, $\rho_G^{\Gamma} = \bar{\Gamma}_7 \oplus \bar{\Gamma}_8$.

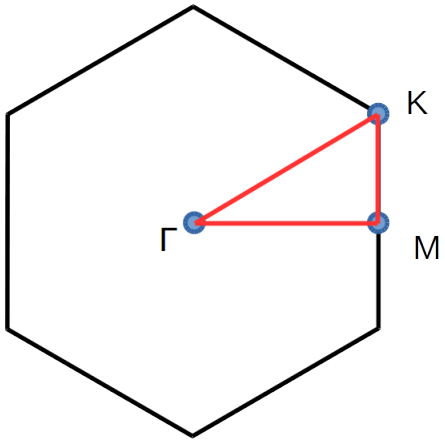

Figure 2.5: First Brillouin Zone for graphene.

C_{3v}	E	$C_3^{\pm}$	m_i	$\bar{E}$	$\bar{C}_3^{\pm}$	$\bar{m}_i$
ρ_G^K	4	-1	0	-4	-1	0
$\bar{K}_4$	1	-1	-i	-1	1	i
$\bar{K}_5$	1	-1	i	-1	1	-i
$\bar{K}_6$	2	1	0	-2	-1	0

Table 2.6: Table of characters of the group C_{3v}.

2.6.2 K point

The little group of this point is C_{3v}. We compute the character of the representation as before:

In this case we find that (see Table 2.6):

$$\rho_G^K = \bar{K}_4 \oplus \bar{K}_5 \oplus \bar{K}_6. \tag{2.33}$$

We see that if we have SOC, the Dirac cones break, since there is no 4-dimensional representation; the 2 dimensional spinless breaks into two 1 dimensional irreps ($\bar{K}_4$, $\bar{K}_5$) and a 2 dimensional one ($\bar{K}_6$).

C_{2v}	E	$C_2^{\pm}$	$m_{1\bar{1}}$	m_{11}	$\bar{E}$
ρ_G^K	4	0	0	0	-4
$\bar{M}_5$	2	0	0	0	-2

Table 2.7: Table of characters of the group C_{2v}.

C_s	E	m	$\bar{E}$	$\bar{m}$
$\bar{\Gamma}_7$	2	0	-2	0
$\bar{\Gamma}_8$	2	0	-2	0
$\bar{\Lambda}_3$	1	-i	-1	i
$\bar{\Lambda}_4$	1	i	-1	-i

Table 2.8: Table of characters of the group C_s.

2.6.3 M point

In this case, the little group is C_{2v} Looking at the character table (see Table 2.7), we see that we have no more work to do, since there is only one representation of the double group, $\bar{M}_5$, so the subduced representation will be a sum of two $\bar{M}_5$. We can still carry out the calculation to check that it is true. Explicitly:

$$\rho_G^M = \bar{M}_5 \oplus \bar{M}_5. \tag{2.34}$$

2.6.4 High-symmetry lines

We can use this machinery to see how this crossings will split when we get a bit away from the high symmetry points. If we follow the high-symmetry lines depicted in Fig. 2.5 (in red), we see that the little group for all the points that lie in any of the lines is C_s, i.e., a mirror plane. Let's start by computing how our degeneracies break down when moving away from the Γ point to the K point.

In Table (2.8), we can see the traces of the relevant representations at Γ for the symmetries of the line that connect Γ and K. Since there are only 2 symemtry operations, there can only be 2 irreps. In this case, both $\bar{\Lambda}$ irreps are 1 dimensional, so both $\bar{\Gamma}_7$ and $\bar{\Gamma}_8$ representations split into unidimensional ones, which is the sum of both $\bar{\Lambda}$ irreps. We can repeat this procedure for all irreps at high-symmetry points to obtain:

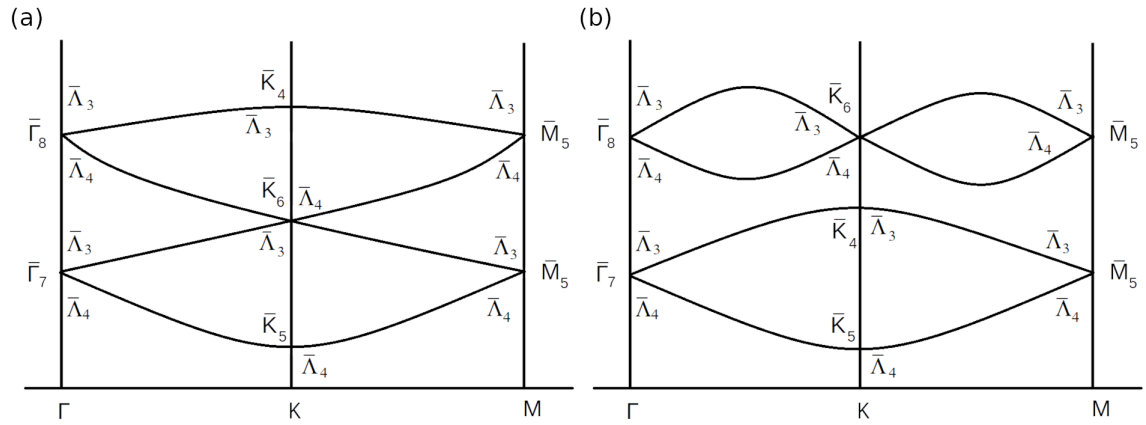

Figure 2.6: Different connectivities allowed by compatibility relations: (a) Connected set of bands, (b) disconnected set of bands.

$$
\begin{aligned}
\bar{\Gamma}_7 &\to \bar{\Lambda}_3 \oplus \bar{\Lambda}_4 \\
\bar{\Gamma}_8 &\to \bar{\Lambda}_3 \oplus \bar{\Lambda}_4 \\
\bar{K}_4 &\to \bar{\Lambda}_3 \\
\bar{K}_5 &\to \bar{\Lambda}_4 \\
\bar{K}_6 &\to \bar{\Lambda}_3 \oplus \bar{\Lambda}_4 \\
\bar{M}_5 &\to \bar{\Lambda}_3 \oplus \bar{\Lambda}_4.
\end{aligned}
\tag{2.35}
$$

Now we can try connect bands. The only restriction is that a band *cannot change the representation along a high-symmetry line*, so a band that comes from a $\bar{\Lambda}_3$ at the Γ point cannot arrive at a $\bar{\Lambda}_4$ at K point. Following this, we get the qualitative pictures on Fig. 2.6 (a) and (b).

We see in Fig. 2.6 (a) that the bands are *connected*, in the sense that we can draw them in a single trace. However, since Group Theory does not give us any prediction on the energetics, we can have another picture, as displayed in Fig. 2.6 (b).

The first one is an Elementary Band Representation, i.e., it is not the sum of smaller dimensional band representations. But in Fig. 2.6 (b) we see that the EBR is *disconnected* now. Since they both together form an EBR, it cannot be that both of them are EBRs independently. So it must happen that at least one of them is not a BR, i.e., not Wannier representable and, thus, *topological*. Therefore, graphene with SOC is topological in both cases; either as a topological insulator (disconnected EBR) or as a topological semimetal (symmetry protected degeneracy at the Femrmi level).

2.7 Conclusions

In this chapter we reviewed the recently developed formalism of topological quantum chemistry. We showed how we can predict topological phases from symmetry arguments. The formalism can be used for diagnosing topology too, as we will show in the following chapter. We will apply the mechanism described here to identify a topological material through its symmetry properties, PbTe, which is a mirror Chern insulator for some experimental structures in the literature.

Chapter 3

Mirror Chern insulator PbTe

As an application of previously described formalism of Topological Quantum Chemistry, a high-throughput calculation of all high-quality[1] stoichiometric materials in the Inorganic Crystal Structure Database (ICSD) [23] was performed. In this chapter we will focus our attention on PbTe, that was predicted to be topologically non-trivial for some crystal structures. We will start by reviewing the formalism of symmetry indicators (TI). Then, we focus on an old simplified tight binding model of PbTe which was predicted to host four Dirac fermions on a two-dimensional antiphase boundary [20–22], hereafter referred to as Fradkin Dagotto Boyanovski (FDB) model. Next, we will modify the model in order to respect all symmetries of the crystal SG $Fm\bar{3}m$ (225). In particular, we will show that our improved TB model captures the transition between a trivial insulator and a mirror Chern and higher-order topological insulator (HOTI), with symmetry indicated topological index $\nu_{\mathbb{Z}_8} = 4$. We will prove that the four Dirac cones in the FDB model at an antiphase domain wall are the boundary modes of this mirror and higher-order topological insulator. Finally, we will demonstrate that any symmetric completion of the FDB model has $\nu_{\mathbb{Z}_8} = 4$, with mirror Chern number $\nu_{m_{1\bar{1}0}} = 2$ and higher-order "S_4" invariant $\delta_{S_4} = 1$ [15, 70, 71] (here $m_{1\bar{1}0}$ denotes the mirror about $\hat{x} - \hat{y}$, and S_4 signifies a fourfold rotoinversion). Finally, we will connect these results to the recent prediction [72, 73] that PbTe may be, in some cases, a TCI/HOTI. In doing so, we will see the relevance of careful structural determination for finding small-gap topological materials.

3.1 Symmetry Indicators

In the previous chapter we showed how the formalism of topological quantum chemistry is used to determine the possible symemtry configurations of the bands starting

[1] Crystals with very accurate measurements of atomic positions and structure

from localized orbitals in real space. We found that if an EBR is split, then at least on set of bands has to be topological. This is a particular example of symmetry-indicated topology. The theory, however, does not predict the precise topological phase of the system. The first quantitative mapping between symmetry and topology was introduced by Fu and Kane [7]. Using the so-called Fu-Kane criterion (or formula), they related the $\mathbb{Z}_2$ topological index to a $\mathbb{Z}_2$ symmetry index, based on inversion eigenvalues of filled bands. An odd number of negative inversion eigenvalues in the set of occupied bands translates into non-trivial $\mathbb{Z}_2$ topological index. This work has been recently generalized into symmetry indicator formalism [14, 15]. We will now review the basic aspects of the formalism.

Following TQC formalism, symmetry data of occupied bands can be described by its band representation, an array containing the irreducible representations at high symmetry momenta. We define {BS} as the set of all possible gapped band structure described by band representations. The authors of [41] tabulated all possible atomic insulators (AI) starting from localized orbitals in real space, which form a linear space we denote as {AI}. Then, topologically non-trivial band structures are those that belong to {BS} while not belonging to {AI}. This can be mathematically expressed as the quotient space $X_{\mathrm{BS}} = \{\mathrm{BS}\}/\{\mathrm{AI}\}$. X_{BS} is always a finitely group of the form $\mathbb{Z}_n$, with $n = 2, 3, 4, 6, 8, 12$. Each generator of X_{BS} is called a symmetry indicator. Even though the authors of Ref. [14] derived the group structure of X_{BS} for all 230 non-magnetic space groups, they did not give the explicit formulas for the generators or the mapping between generators and topological invariants. This work has been recently developed by the authors in Ref. [15], where they provide explicit formulas to compute the generators (symmetry indicators) based on the band representations. They also compute the mapping between symmetry indicators and topological invariants, which determine the topological features of the band structure.

It is worth noting that this system has both advantages and disadvantages. On the one hand, the diagnose power is limited; topological phases can be diagnosed as trivial if the required symmetries are not present. As an example, a strong 3D TI is protected by TRS and can be diagnosed by inversion symmetry if present, but the 3D TI topological phase can exit regardless of inversion symmetry. However, symmetry indicators have proved useful for high-throughput ab-initio calculations of tens of thousands of materials, revealing that more than 27% of all materials in Nature are topological [23].

3.2 Effective Tight Binding model

Let us start as did the authors of Ref. [20] considering the rocksalt structure of PbTe (see Fig. 3.1 (a)), in the space group $Fm\bar{3}m$ (225), a centrosymmetric, symmorphic

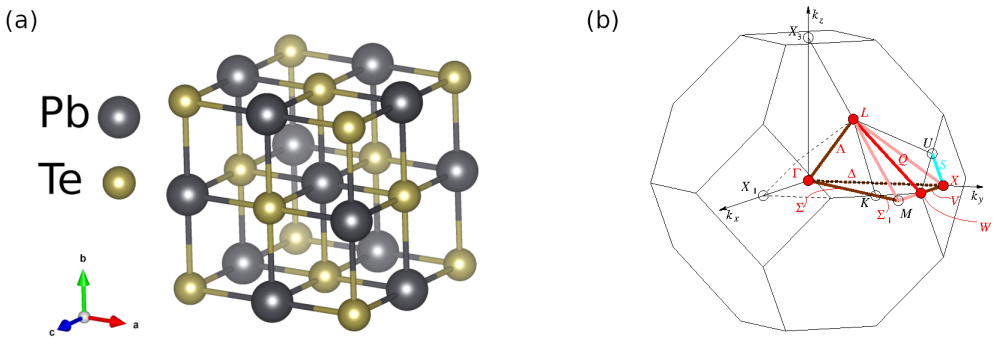

Figure 3.1: (a) PbTe crystal structure. It has the same structure as rocksalt (NaCl), in SG $Fm\bar{3}m$ (225). (b) Brillouin Zone for SG $Fm\bar{3}m$ (225) [67–69].

space group with a face-centered-cubic (FCC) Bravais lattice and octahedral point group (see Fig. 3.1 (b)). We take the following basis for the Bravais lattice [2]:

$$\mathbf{t_1} = (0, 1/2, 1/2),\ \mathbf{t_2} = (1/2, 0, 1/2),\ \mathbf{t_3} = (1/2, 1/2, 0). \tag{3.1}$$

The rocksalt structure has Te atoms located at the 4a Wyckoff position, with reduced coordinates $q_a = (0, 0, 0)$, and Pb atoms at the 4b Wyckoff position with reduced coordinates $q_b = (1/2, 1/2, 1/2)$. The point group of PbTe is generated by a threefold rotation $C_{3,111}$ about the body diagonal of the unit cell, a fourfold rotation C_{4x} about the $\hat{\mathbf{x}} = \mathbf{t_2} + \mathbf{t_3} - \mathbf{t_1}$ axis, spatial inversion I , and time-reversal symmetry T. The original model of FDB consisted of spin-1/2 s orbitals on the 4a and 4b Wyckoff positions as a proxy for the Te and Pb atoms (whether we start from s or p orbitals, the sign of the inversion matrix will change, but all topological properties remain invariant). They added a staggered on-site potential taking opposite values $\pm m$ on the Te and Pb sites, and a nearest-neighbor spin-dependent hopping. Letting τ be a set of Pauli matrices acting in the orbital (Te,Pb) basis, and letting σ be the set of Pauli matrices acting on spin, we can write the Bloch Hamiltonian for the FDB model as

$$H_{FDB} = m\tau_z + t\tau_y \sum_{\mu=x,y,z} \sigma_\mu \cos\left(\frac{k_\mu}{2}\right), \tag{3.2}$$

where we have taken the liberty of restoring a neglected factor of i in the hopping term to restore TRS [4] [3]. Eq. 3.2 is manifestly time-reversal, inversion, and $C_{3,111}$

[2] We set the lattice constant a = 1 for simplicity

[3] While this makes our Eq. 3.2 formally different from the original FDB model, we view the lack of time-reversal symmetry in Ref. [20] to be a simple oversight.

symmetric; each of these symmetries acts trivially in the orbital τ space, and as a rotation (the identity rotation for inversion) on the spin degrees of freedom. Precisely, we have for these symmetries g that $\Delta(g)^{-1}H_{FDB}(\mathbf{k})\Delta(g) = H_{FDB}(g\mathbf{k})$, with the matrix representation Δ specified by

$$\begin{aligned}\Delta(C_{3,111}) &= \exp\left[\frac{-i\pi}{3\sqrt{3}}(\sigma_x+\sigma_y+\sigma_z)\right],\\ \Delta(I) &= \mathbb{I}_{4x4},\\ \Delta(T) &= i\sigma_y\mathcal{K},\end{aligned} \tag{3.3}$$

with $\mathcal{K}$ being complex conjugation.

The spectrum of this Hamiltonian consists of two sets of doubly degenerate bands (due to IT symmetry) separated by a spectral gap which is smallest at the L point $(1/2, 1/2, 1/2)$ and given by $\delta E_L = 2m$. Depending on the sign of m, there is a band inversion at the L point: for $m > 0$ the valence bands carry the representation $\bar{L}_9$ of the little group of L [with inversion eigenvalues (-1, -1)], while for $m < 0$ the valence bands carry the representation $\bar{L}_8$ of the little group of L [with inversion eigenvalues (+1,+1)]. Because there are four L points in the FCC Brillouin zone, this is not a $\mathbb{Z}_2$ nontrivial TI [7], and so we must look for nontrivial TCI invariants.

Here, however, we run into a problem: The Hamiltonian H_{FDB} is C_{4x} symmetric, but the matrix representative of C_{4x} can be seen to be

$$\Delta(C_{4x}) = i\tau_z\sigma_y \exp\left(-i\frac{\pi}{4}\sigma_x\right). \tag{3.4}$$

This has the unfortunate property that $\Delta(C_{4x})^4 = +1$, rather than -1 as needed for a double-valued representation. Repairing this by multiplying by a factor of $\sqrt{i}$ is futile, as the $\Delta(C_{4x}$ and $\Delta(T)$ no longer commute. Thus, the FDB Hamiltonian does not have the symmetries of SG $Fm\bar{3}m$.

To repair the symmetries, we seek hopping terms which vanish at the L point, are non-vanishing elsewhere and transform in the representation given by Eq. 3.3, along with

$$\Delta(C_{4x}) = \exp\left(-i\frac{\pi}{4}\sigma_x\right). \tag{3.5}$$

In this way, we will replicate the band inversion at L in our symmetric model. Let us first fix the spin-orbit coupling (SOC) term. Noting that the matrices $\tau_{x,y}$, σ_μ transform in a pseudovector representation under rotoinversions, we need them to be multiplied by functions of k which are also pseudovectors. Combining this observation with time-reversal invariance and the boundary conditions on the Bloch Hamiltonian, we find that the simplest choice of SOC term which vanishes at L is

$$H_{SOC} = t\tau_y \sum_{\mu,\nu,\lambda=x,y,z} \left(\epsilon^{\mu\nu\lambda} \sigma_\mu sin\left(\frac{k_\nu}{2}\right) sin(k_\lambda) \right). \tag{3.6}$$

For now, let us overlook the long (fifth nearest-neighbor) range of this coupling in light of its mathematical simplicity. We may be tempted to take $m\tau_z + H_{SOC}$ as our improved Hamiltonian; however, H_{SOC} vanishes along the whole $\Gamma - L$ line, rather than just at the L point. To remedy this, we can add two additional spin-independent hopping terms:

$$H_{hop} = \sum_{\mu=x,y,z} \left[\delta_1 \tau_z (1 + cos(k_\mu)) + \delta_2 \tau_x cos\left(\frac{k_\mu}{2}\right) \right]. \tag{3.7}$$

We take for our full improved Hamiltonian

$$H_{iFDB} = m\tau_z + H_{SOC} + H_{hop}. \tag{3.8}$$

When $m = 0$ with t and δ_2 nonzero, this model is gapless only at the L point. For $m \neq 0$, a nonzero δ_1 ensures that the spectrum of this Hamiltonian is gapped. We see that there is thus an insulator-to-insulator transition driven by an inversion of bands at the L point, just as in the original FDB model. We show the bulk spectrum for positive and negative values of m in Fig. 3.2 (a) and Fig. 3.2 (b).

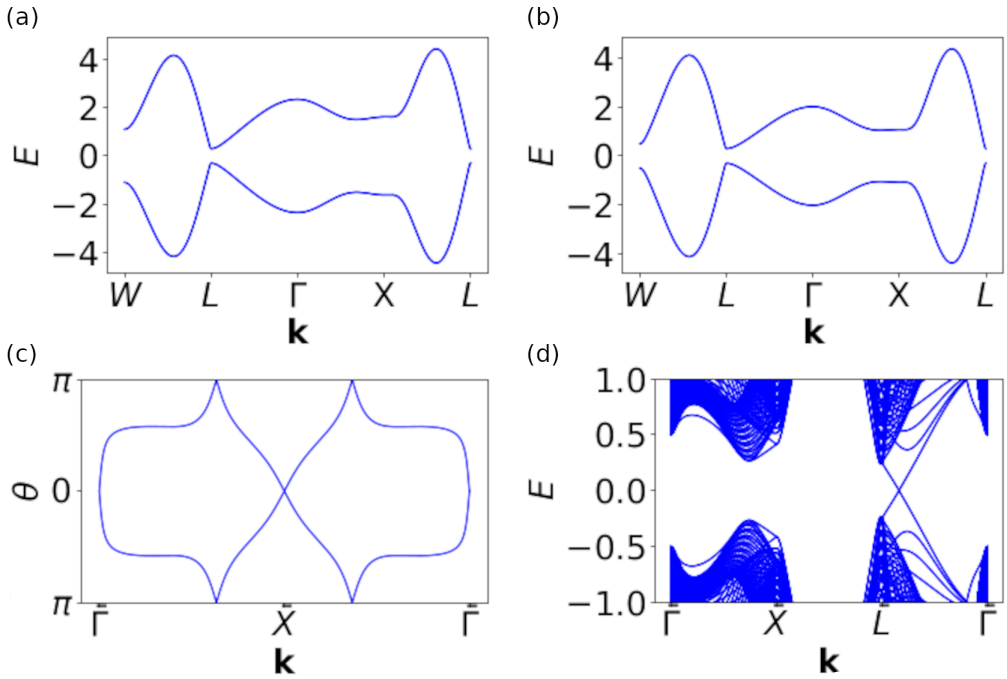

Figure 3.2: (a) and (b) Spectrum of the iFDB Hamiltonian given in Eq. 3.8, with parameter values $t = \delta_2 = 0.5$, $\delta_1 = 0.1$. In (a) we take $m = 0.3$, while in (b) we take $m = -0.3$. (c) Wilson loop in the k_2 direction evaluated in the space of the lowest two bands of the model in Eq. 3.8 with $m < 0$, as a function of k_3, with $k_1 = 0$. We see that the Wilson loop phases Θ wind twice around the circle $(-\pi, \pi]$. This implies that the model is in a topological phase with mirror Chern number $\nu_{m_{1\bar{0}}} = 2$. (d) Spectrum for the topological phase of the iFDB model for a $\hat{z}$-normal slab. Note the mirror-symmetry protected Dirac fermion on the $\bar{\Gamma} - \bar{L}$ line.

3.3 Topological properties

Let us now examine the topological nature of this band-inversion transition. We will start by analyzing the band representations in the model following Refs. [11, 23, 41]. Following the notation of the Bilbao Crystallographic Server [67–69], our model is induced from orbitals transforming under the $\bar{E}_{1g}$ representation of the point group O_h on the 4a site, and a second set of orbitals transforming in the same representation on the 4b site. The four bands in our model thus transform under the composite band representation $(\bar{E}_{1g})4a \uparrow G \oplus (\bar{E}_{1g})4b \uparrow G$. These two elementary band representations subduce representations of the little group G_k at each of the high-symmetry momenta Γ, X, W, and L in the Brillouin zone; we summarize these representations in Table 3.1 below. In the atomic limit of H_{iFDB}, we have $m \gg t, \delta_1, \delta_2$, and so the valence

EBR	Γ	X	L	W
$(\bar{E}_{1g})_{4a} \uparrow G$	$\bar{\Gamma}_6$	$\bar{X}_6$	$\bar{L}_9$	$\bar{W}_6$
$(\bar{E}_{1g})_{4b} \uparrow G$	$\bar{\Gamma}_6$	$\bar{X}_6$	$\bar{L}_8$	$\bar{W}_7$

Table 3.1: Little group irreps subduced by each of the elementary band representations in our model. The first column gives the name of the elementary band representation (EBR). The subsequent columns give the little group irreps at each of the high-symmetry points.

bands of our model transform in the $(\bar{E}4b \uparrow G)$ elementary band representation, with occupied little group representations $\bar{\Gamma}_6, \bar{X}_6, \bar{W}_6, \bar{L}_9$; this can be checked explicitly using the representation Δ defined in Eqs. 3.3 and 3.5 and taking into account the boundary conditions $|u_{n\mathbf{k}+n_i\mathbf{g}_i}> = (\tau_z)^{\sum_i n_i}|u_{n\mathbf{k}}>$, where $\{\mathbf{g}_i\}$ is a basis for the reciprocal lattice, and $\{n_i\}$ are integers; this expresses the "tight-binding gauge" boundary conditions [74]. Upon inverting bands by taking $t \geq \delta_2 \gg \delta_1 > 0 > m$, $|m| \ll t$, we see that the occupied band irreps at Γ, X, and W have not changed. At L, however, the wave functions now transform under the $\bar{L}_8$ irrep. Examining the full table of elementary band representations for $Fm\bar{3}m$ [67–69], we find that the collection $(\bar{\Gamma}_6, \bar{X}_6, \bar{W}_6, \bar{L}_8)$ of occupied little group representations cannot be subduced by an integer sum or difference of elementary band representations; we thus conclude that this phase of our model is a symmetry-indicated, stable topological crystalline insulator. Going further, we can attempt to express the irrep multiplicities in this model as a rational sum of those in elementary band representations (EBRs). Reading off the denominator of the rational coefficients, we find that symmetry-indicated TCIs in this space group are classified by an index $\nu_{\mathbb{Z}_8}$. The index $\nu_{\mathbb{Z}_8}$ can be expressed as [15, 70, 71]

$$\nu_{\mathbb{Z}_8} = \kappa_1 - 2\kappa_4, \tag{3.9}$$

where $4\kappa_1$ is the sum of occupied band inversion eigenvalues ans $2\sqrt{2}\kappa_4$ is the sum of occupied band IC_{4z} eigenvalues. Note that both κ_1 and κ_4 are integers [71]. For our model, we have $\nu_{\mathbb{Z}_8} = 4$ in the topological phase, and $\nu_{\mathbb{Z}_8} = 0$ in the trivial phase. As shown in Refs. [15, 71], a minimal model for a TCI with $\nu_{\mathbb{Z}_8} = 4$ arises through a "stacking" (in Hilbert space) of four Z_2 odd topological insulators. We thus expect to find protected gapless states on symmetric surfaces of this model, as we will discuss further below.

Furthermore, note that while the original FDB model is not C_{4z} symmetric, it is inversion symmetric. Thus, the sum of occupied band inversion eigenvalues κ_1^{FDB} can be computed for that model and is given by

$$\kappa_1^{FDB} = \begin{cases} 0, & m > 0 \\ 4, & m < 0. \end{cases} \tag{3.10}$$

Next, note that IC_{4z} is not in the little group of any of the L points. Therefore, in any symmetric completion of the FDB model the occupied band IC_{4z} eigenvalues do not change as a function of m, and so neither does κ_4. Thus, in any symmetric completion of the FDB model, the index $\nu_{\mathbb{Z}_8}$ must change by 4 as the sign of m changes. Assuming additionally that the $m > 0$ phase is connected to the (unobstructed [10]) atomic limit, we deduce that the band inversion in the FDB model becomes, when cubic symmetry is enforced, the transition between phases with $\nu_{\mathbb{Z}_8} = 0$ and $\nu_{\mathbb{Z}_8} = 4$.

As discussed in detail in Refs. [15,71], the value of $\nu_{\mathbb{Z}_8}$ does not uniquely determine the topological phase of a system in space group $Fm\bar{3}m$. In particular, with $\nu_{\mathbb{Z}_8} = 4$, there are two possible types of topological phase: the first has a mirror Chern number $\nu_{m_z} = 4 \bmod 8$ associated with the m_z mirror symmetry, while the second has both a mirror Chern number $\nu_{m_{1\bar{1}0}} = 2 \bmod 8$ associated with the diagonal $\hat{x} - \hat{y}$ mirror symmetry, as well as a nonvanishing higher-order topological index. It is this latter phase which describes our current model.

We can make these statements more precise by examining the low-energy $\mathbf{k} \cdot \boldsymbol{p}$ theory for the topological transition in both H_{FDB} and H_{iFDB}. Starting with the original FDB model, we find by expanding Eq. 3.2 that

$$H_{FDB}(L + \mathbf{k}) \approx m\tau_z + \sum_{\mu=x,y,z} \frac{t}{2} \tau_y \sigma_\mu k_\mu. \tag{3.11}$$

On the other hand, performing the same expnsion of H_{iFDB}, setting $\delta_2 = t$, and defining the rotated coordinates (k_a, k_b, k_c) and spin matrices (s_a, s_b, s_c) as in Eqs. 3.12 and 3.13)

$$\begin{pmatrix} k_1 \\ k_2 \\ k_3 \end{pmatrix} = \begin{pmatrix} \frac{-1}{2\sqrt{6}} & \frac{-1}{2\sqrt{2}} & \frac{1}{\sqrt{3}} \\ \frac{-1}{2\sqrt{6}} & \frac{1}{2\sqrt{2}} & \frac{1}{\sqrt{3}} \\ \frac{1}{\sqrt{6}} & 0 & \frac{1}{\sqrt{3}} \end{pmatrix} \begin{pmatrix} k_a \\ k_b \\ k_c \end{pmatrix}, \tag{3.12}$$

$$\begin{pmatrix} s_x \\ s_y \\ s_z \end{pmatrix} = \begin{pmatrix} \frac{1}{\sqrt{2}} & \frac{\sqrt{3}+\sqrt{6}}{6} & \frac{\sqrt{2}-1}{2\sqrt{3}} \\ \frac{-1}{\sqrt{2}} & \frac{\sqrt{3}+\sqrt{6}}{6} & \frac{\sqrt{2}-1}{2\sqrt{3}} \\ 0 & \frac{1}{\sqrt{6}} - \frac{1}{\sqrt{3}} & \frac{1}{\sqrt{6}} + \frac{1}{\sqrt{3}} \end{pmatrix} \begin{pmatrix} s_a \\ s_b \\ s_c \end{pmatrix}, \tag{3.13}$$

yields, to *quadratic* order:

$$H_{iFDB}(L + \mathbf{k}) \approx [m + 2\delta_1(k_a^2 + k_b^2 + k_c^2)]\tau_z + \sqrt{3}\delta_2 k_c \tau_x + 2T\sqrt{3}\tau_y(k_a s_a + k_b s_b). \tag{3.14}$$

Up to a choice of basis for the Dirac matrices, this is the Bernevig-Hughes-Zhang model Hamiltonian for a topological insulator [75,76] (note that because of our choice of boundary conditions and our expansion about the L point, inversion symmetry is represented by $\Delta L(I) = \tau_z$ in the $k \cdot p$ expansion). Eq. 3.14 is also equivalent to Eq. 3.11 if we take $\delta_2 = 2T = t/2$. Since there are four L points, we see that this is a TCI rather than a TI transition. Furthermore, note that the plane $k_x = k_y$ corresponds to the plane $k_b = 0$, and is invariant under $m_{1\bar{1}0}$; this symmetry is represented at the L point by the matrix $\Delta L(m_{1\bar{1}0}) = \exp\big[i\pi/(2\sqrt{2})(s_a)\big]$. Restricting H_{iFDB} to the mirror plane, we find that the Hamiltonian is block diagonal in the basis of $m_{1\bar{1}0}$ eigenstates, and describes a Chern insulator transition in each mirror subspace. Since there are two L points in this mirror plane, we thus deduce, following Ref. [77], that this model corresponds to a mirror Chern insulator with $\nu_{m_{1\bar{1}0}} = 2$. To verify this, we extract the mirror Chern number from the flow of hybrid Wannier charge centers [78,79], i.e., from the Wilson loop [80,81]. We show in Fig. 3.2 (c) the k_2 directed Wilson loop for the occupied bands as a function of k_3. We see that in the $k_1 = 0$ plane the Wilson loop phases exhibit a nontrivial winding with winding number 2; since in the FCC Brillouin zone this is the only mirror invariant plane [77], this signifies the mirror Chern number $\nu_{m_{1\bar{1}0}} = 2$ [82].

As pointed out in Refs. [15,71,83], models in space group $Fm\bar{3}m1'$ with $\nu_{\mathbb{Z}_8} = 4$ and $\nu_{m_{1\bar{1}0}} = 2$ also have a nontrivial higher-order index $\delta S_4 = 1$ protected by fourfold rotoinversion symmetry. This phase has four Dirac cones on a $\hat{z}$-normal surface, thus explaining the four Dirac fermions on an antiphase boundary found in Refs. [20–22]. At the level of the tight-binding model, an antiphase domain wall is simply a boundary between the trivial ($m > 0$) and topological ($m < 0$) phase of the model. These domain-wall fermions are indeed of topological origin, and are symmetry protected in any symmetric extension of the FDB model. We show the spectrum of the topological phase of Eq. (3.8) on a $\hat{\mathbf{z}}$-normal slab in Fig. 3.2 (d).

Finally, note that the original low-energy FDB Hamiltonian in Eq. 3.2 has an accidental mirror symmetry $\tilde{\Delta}(m_{1\bar{1}0}) = \tau_z \exp\big[i\pi/(2\sqrt{2})(s_x - s_y)\big]$, which leaves the plane $k_x = k_y$ invariant. While this symmetry is inconsistent with the inversion symmetry for the full model (and also will be broken by crytal-symmetry preserving perturbations, including higher-order terms in the $k \cdot p$ expansion), it explains why the authors of Ref. [20–22] were able to find domain-wall fermions in their model.

3.4 Ab initio results

In the previous sections, we have seen how symmetrized completions of the FDB model of PbTe yield higher-order topological and mirror Chern insulators. Under certain conditions, the band structure for realistic PbTe as computed with ab initio

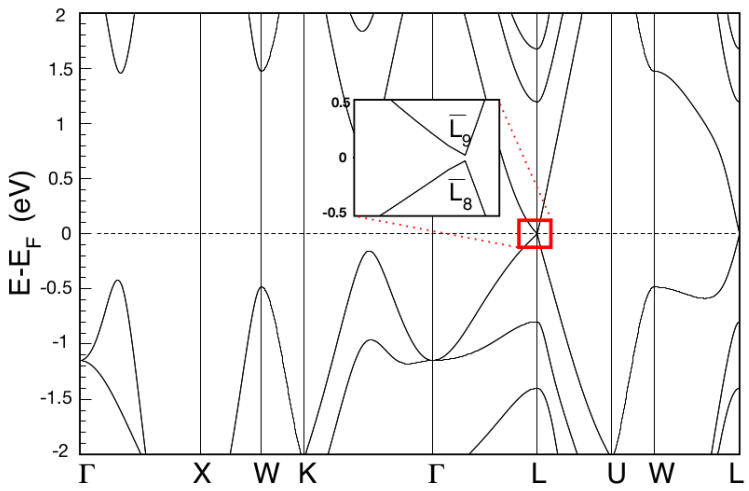

Figure 3.3: Bulk band structure of PbTe, calculated using the structure reported in Reference [48]. The inset shows the small gap and band inversion at the L point.

methods realizes this same $\nu_{\mathbb{Z}_8} = 4$ symmetry-indicated phase. This can be seen by analyzing the material catalogs of Refs. [23,72], which both report the value of $\nu_{\mathbb{Z}_8} = 4$ for PbTe. For confirmation, we have recomputed the ab initio band structure of PbTe using density functional theory (DFT) [45,46] as implemented in the Vienna Ab initio Simulation Package (VASP) [49, 50]. We use the structural parameters as reported in Ref. [84]. The interaction between ion cores and valence electrons was treated by the projector augmented-wave method [51], the generalized gradient approximation (GGA) for the exchange-correlation potential with the Perdew-Burke-Ernkzerhof for solids parametrization [52], and spin-orbit coupling was taken into account by the second variation method [85]. A Monkhorst-Pack centered at Γ k-point grid of ($11 \times 11 \times 11$) for reciprocal space integration and 500 eV energy cutoff of the plane-wave expansion have been used. We show the band structure in Fig. 3.3, with an inset highlighting the rather small gap at L. Employing the VASPtoTrace tool [23, 67–69], we compute the little group irreps of the occupied bands at the high-symmetry points, shown in Table 3.2; we give the irreps of SnTe as well for comparison. By using Eq. 3.9, we see that $\nu_{\mathbb{Z}_8} = 4$ for both SnTe and PbTe. Note, in fact, that the irrep labels for SnTe and PbTe differ only in a shift of the origin of the system by $(\frac{1}{2}, \frac{1}{2}, \frac{1}{2})$. Furthermore, the topological transition to $\nu_{\mathbb{Z}_8} = 4$ in the realistic material is driven by a band inversion of the irreps at L relative to W , just as in the FDB model. To fully determine the topological phase, we evaluate the mirror Chern number of the occupied bands using Quantum Espresso and Z2PACK [53–55, 79]. We find a mirror

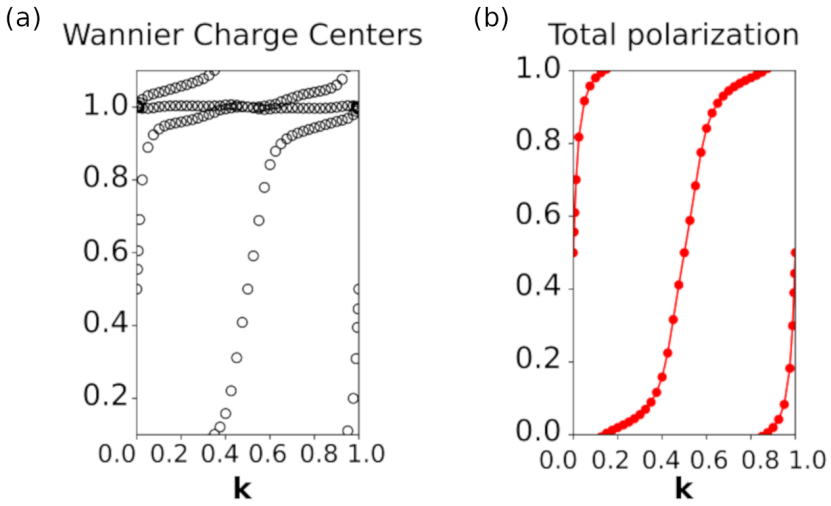

Figure 3.4: Hybrid Wannier charge centers for the +i mirror subspace of the occupied bands of PbTe in the m_{110}-invariant plane. (a) Raw Wannier centers (Wilson loop eigenvalues). (b) Trace of the Hybrid Wannier charge centers matrix (see Sec. 1.5). Since the trace winds twice across the unit cell, we deduce that the mirror Chern number $\nu_{m_{110}} = 2$.

Chern number $\nu_{m_{110}} = \nu_{m_{1\bar{1}0}} = 2$, just as in the iFDB model [4] (see Fig. 3.4).

k	SnTe	PbTe
Γ	$\bar{\Gamma}_6\bar{\Gamma}_6$, $\bar{\Gamma}_8$, $\bar{\Gamma}_{11}$	$\bar{\Gamma}_6\bar{\Gamma}_6$, $\bar{\Gamma}_8$, $\bar{\Gamma}_{11}$
X	$\bar{X}_6$, $\bar{X}_6$, $\bar{X}_8$, $\bar{X}_8$, $\bar{X}_9$	$\bar{X}_6$, $\bar{X}_6$, $\bar{X}_8$, $\bar{X}_8$, $\bar{X}_9$
L	$\bar{L}_9$, $\bar{L}_8$, $\bar{L}_8$, $\bar{L}_4\bar{L}_5$, $\bar{L}_9$,	$\bar{L}_8$, $\bar{L}_9$, $\bar{L}_9$, $\bar{L}_6\bar{L}_7$, $\bar{L}_8$,
W	$\bar{W}_6$, $\bar{W}_7$, $\bar{W}_7$, $\bar{W}_6$, $\bar{W}_7$	$\bar{W}_7$, $\bar{W}_6$, $\bar{W}_7$, $\bar{W}_6$, $\bar{W}_6$

Table 3.2: Occupied band irreps for SnTe and PbTe at the high- symmetry points. Irreps are listed in order of increasing energy, i.e., those states closest to the Fermi level appear at the end of the list. Note that the irreps at Γ and X are identical for the two materials.

However, it is well accepted that the mirror Chern number $\nu_{m_{1\bar{1}0}}$ in PbTe is zero under ambient experimental conditions, while it is 2 for SnTe [77]. To reconcile this with the non- trivial $\nu_{\mathbb{Z}_8} = 4$ topological index, we note that in addition to the structure used for the ab initio calculations here and in Refs. [23, 72], PbTe has 41 other entries in the ICSD [86] in the space group $Fm\bar{3}m1'$ [23]. A DFT analysis of

[4] These two mirror Chern numbers are equal due to the cubic symmetry of the system.

other structures (for instance, the structure reported in Ref. [87]) yields a trivial index $\nu_{\mathbb{Z}_8} = 0$ due to a band deinversion at L, in agreement with the experimental findings. This highlights the fact that for small band-gap insulators, one must be cautious in extracting the band topology from ab initio calculations; for PbTe in particular, the failure of semilocal DFT to correctly produce the (correct sign of the) experimental band gap in certain cases has been noted previously [88].

To investigate this systematically, we have computed the band structures and topological index $\nu_{\mathbb{Z}_8}$ for all 42 entries of PbTe in the ICSD, using the Perdew-Burke-Ernzerhof (PBE) functional. The input parameters for these compounds differ only in the reported lattice constant a_0, which range between 6.157 and 6.543 Å. For the six reported structures with $a_0 \leq 6.44\mathring{A}$, PBE predicts $\nu_{\mathbb{Z}_8} = 4$; for the remaining with larger lattice constants we find $\nu_{\mathbb{Z}_8} = 0$. In Table 3.3 we give a table summarizing our DFT calculations. Taken optimistically, this shows that PbTe is very close to a topological phase transition, which may be tunable as a function of external parameters such as hydrostatic pressure.

ICSD	$a_0(\mathring{A})$	Top?	ICSD	$a_0(\mathring{A})$	Top?	ICSD	$a_0(\mathring{A})$	Top?	ICSD	$a_0(\mathring{A})$	Top?
48585	6.47	NO	194220	6.46	NO	648586	6.458	NO	648599	6.459	NO
38295	6.462	NO	648616	6.462	NO	648587	6.456	NO	648600	6.452	NO
600522	6.461	NO	648617	6.463	NO	648603	6.458	NO	600843	6.47	NO
96500	6.459	NO	648589	6.461	NO	648605	6.4591	NO	602956	6.46	NO
96504	6.461	NO	648590	6.445	NO	648606	6.4603	NO	604178	6.460	NO
96505	6.461	NO	648591	6.46	NO	648607	6.463	NO	96506	6.460	NO
648592	6.460	NO	648608	6.4564	NO	63099	6.454	NO	648593	6.459	NO
648612	6.452	NO	648583	6.464	NO	648594	6.459	NO	182661	6.500	NO
648584	6.46	NO	648596	6.46	NO	182662	6.543	NO	648614	6.46	NO
648597	6.439	YES	648615	6.157	YES	648588	6.44	YES	63098	6.4384	YES
153711	6.4245	YES	648613	6.439	YES						

Table 3.3: Summary of computed topological phases for all reported structures of PbTe in the ICSD [23, 86]. The first column gives the ICSD id of the reported structure. The second column gives the lattice constant a_0, measured in Angstroms. The third column indicates the computed value of the topological index $\nu_{\mathbb{Z}_8}$: "Yes" corresponds to$\nu_{\mathbb{Z}_8} = 4$, while "No" corresponds to $\nu_{\mathbb{Z}_8} = 0$.

3.5 Conclusions

We have revisited the effective model of PbTe as presented in Refs. [20–22]. We have shown that the domain-wall fermions in the FDB model, long derided as non-

topological, are signatures of the topological surface states present in any symmetric completion of the model, protected by mirror and fourfold rotoinversion symmetries. Furthermore, we show that ab initio calculations reveal that some of the reported structures of realistic PbTe are in this same symmetry-indicated class of materials, at least within the GGA. This shows that PbTe is an ideal platform for exploring structurally tunable topological behavior. Finally, while within the context of our effective model there is no difference between an antiphase domain wall and a domain wall with the vacuum, this is not necessarily true in a more realistic system. Given the recent focus on defect response of higher-order topological insulators [89–91], it would be interesting to examine this more carefully for both SnTe and PbTe structural variations in future work.

Chapter 4

Time Reversal symmetry breaking: CoS_2

So far we have reviewed the theory of Topological Quantum Chemistry and applied it to a specific case of Topological Insulator, spinful graphene and PbTe. There are, however, topological phases of matter that are not insulationg. This is the case of Topologicla Semimetals, systems in which degeneracies at the Fermi level are protected by topology, symmetry or both. In this chapter we will analyze our most recent recent work on the discovery of a new topological semimetal phase on a ferromagnetic pyrite, CoS_2. Contrary to previous chapters where we analyzed very symmetric systems, in this case the magnetization breaks many symmetries of the system, but we still manage to predict topological features. At the end of the chapter, we compare our theoretical predictions to recent experimental data, which shows good matching between theory and experiment.

4.1 Introduction

Topological semimetals are a class of materials that display protected band crossings close to the Fermi level with nonzero Berry phase [23, 24, 34, 92–94]. In 3 dimensions (3D) one can find three types of topological band crossings, namely, nodes, lines and planes. When nodes have a linear dispersion in all directions and they carry a topological charge, they are named Weyl nodes. Weyl nodes can only exist in systems with broken inversion or time-reversal symmetry (TRS). They are stable even in the absence of symmetries and have very interesting surface states called Fermi arcs, that connect the surface projection of the nodes. From each Weyl node with topological charge 1, there will be a Fermi arc stemming from its projection in the surface. Important examples of inversion symmetry breaking Weyl semimetals are transition

metal monophosphides [95], $MoTe_2$ [96] and TaAs [25–27]. Contrary to the prolific discovery of inversion symmetry-broken Weyl semimetals, time reversal symmetry-broken (magnetic) ones are still scarce. They were first predicted in pyrochlore iridates [97], $HgCr_2Se_4$ [98] and the Heusler family of XCo_2Z (X=IVB or VB; Z=IVA or IIIA) [99], and recently measured experimentally in $EuCd_2As_2$ [100], $Co_3Sn_2S_2$ [37, 101] and Co_2MnGa [102]. These materials usually display a large anomalous Hall effect [37], which is important for both electronic and spintronic devices [103], and they played a fundamental role in the first experimental realization of the chiral anomaly [104]. Higher order generalizations of Weyl nodes have been proposed [32] and confirmed experimentally [105–109]. These so called multifold fermions have higher Chern numbers, which produce more Fermi arcs in the surface. It has also been shown that space group chirality (no inversion or mirror symmetries) has an important effect on the connectivity of such Fermi arcs [105, 110]. Even if the search for multifold fermions has been focused on non-magnetic materials, there has been an increased shift of attention to magnetic systems. There are, however, few material predictions that can host magnetic multifold fermions [111, 112], thus, making it a priority to find new material realizations of such multifold fermions.

Another notable topological feature are Nodal lines. These crossings are protected by inversion-TRS, spin rotation or reflection symmetries [113–120]. Compared to Weyl semimetals, Nodal line semimetals are more difficult to diagnose, since the topological invariants [121] and, thus, the surface spectrum, are protected by crystalline symmetries, so surfaces not preserving them will not display topologically protected surface states [122–125]. In the facets where symmetries are preserved, however, there will appear what are known as drumhead states, a set of surface states covering the projection of the nodal line in the surface. In the cases in which spin-orbit coupling (SOC) can be neglected, Nodal lines protected by inversion-TRS can occur at any point in the Brillouin zone (BZ), as well as in high symmetry planes. When including SOC, though, inversion-TRS can no longer protect the crossings, and these will generally be gapped. This is the case for spin rotation symmetry protected Nodal lines too, because SOC mixes spin components and gaps the crossings. Then, in the cases in which SOC cannot be neglected, only mirror symmetries can protect Nodal lines. This is why there are few examples of real materials that host Nodal lines when SOC is taken into account [122, 126], and why finding new ones is exciting both theoretically and experimentally. Like in Weyl semimetals, Nodal line semimetals have recently been found to have large Spin Hall current [127], expanding the family of topological materials promising for topological electronic applications. Generalizing Nodal lines, non-symmorphic symmetries can force crossings on entire high symmetry planes in the boundary of the BZ. These are named nodal planes, which give rise to Topological Protectorates; regions of the Fermi surface that intersect the Nodal planes. They have been predicted to be large sources of Berry curvature [128, 129].

Pyrites of the form XS_2 (with X being Fe, Ni and Co) are a notable family of TRS-breaking materials that have been studied for decades due to the large size of pure crystals that can be found in nature or easily grown experimentally [130, 131]. Among this family, CoS_2 has been experimentally confirmed to be ferromagnetic and extensively studied for its spin polarization and magnetic properties. Unlike many magnetic materials, CoS_2 is an itinerant ferromagnet [132, 133], that is, the ferromagnetism does not stem from highly localized electrons. Thus, electron-electron interactions can be neglected when studying the electronic properties of the system. This implies that standard mean field approximations such as density functional theory (DFT) within the local spin density approximation (LSDA) are an excellent way to obtain reliable and accurate electronic properties [134].

Topological condensed matter physics is a relatively new field of physics. Thus, it is possible that 'old' materials could display topological properties that have been missed. This is the case on point; it has been recently reported experimentally that CoS_2 is a Weyl semimetal, with spin-polarized single and double Fermi arcs stemming from the projections of the Weyl nodes in the surface [35]. In this work, we perform an extensive study of the topological properties as a function of its crystal symmetries and also report several Nodal line structures near the Fermi level that survive the addition of SOC interaction. We also find novel drumhead surface states emerging from the Nodal lines.

The presence of both Nodal lines and Weyl nodes near the Fermi level, along with the big size of pure crystals and ferromagnetic nature of the pyrite, make CoS_2 a promising platform to probe topological phenomena in an accessible material that can be used in all sorts of electronic applications, from new magnetic memories to spin injector junctions, in which the spin polarized Fermi arcs will contribute to reduce the weight of the minority spin pocket [135].

This work is structured as follows: First we review the basic aspects of Weyl nodes and Nodal lines. Next, we study the symmetry of the crystal and electronic structures. We then analyze the symmetry enforced 4-fold degeneracy arising at the $M = (\frac{1}{2}, \frac{1}{2}, 0)$ point and the effect of spin-orbit coupling on it. Finally we study the Nodal lines and Weyls nodes in CoS_2. We conclude by summarizing the results of this work.

4.2 Topological properties of Weyl nodes and Nodal lines

In topological semimetals, conduction and valence bands intersect at some points inside the Brillouin Zone (BZ). These crossings can be either accidental or protected, either by symmetry or non-trivial topology. Accidental crossings can be broken by

small perturbations that respect the symmetries of system. By definition, protected crossings cannot. We can think of two main types of protection, protection by crystalline symmetry and topological protection. In the first case, bands that cross have different transformation properties under some symmetry element that leaves the degeneracy point invariant in momentum space; in this case we say that the bands belong to different irreducible representations [43] and thus can not hybridize. This is the case for Dirac semimetals [136–138], in which C_n rotational symmetry protects the Dirac nodes in the $\Gamma - Z$ direction. We can also think of crossings that can be protected by mirror symmetries that leave a plane in variant in the BZ. Analogous to Dirac nodes, in-plane crossings can be mirror symmetry-protected. In this case, instead of 0-dimensional crossings, collections of 0-dimensional crossings span the whole plane, thus giving rise to 1-dimensional Nodal lines [113–120]. These nodal lines come in a variety of ways; they can form closed rings inside the BZ, closed rings connecting neighboring BZ, open strings that connect two BZ or even connected loops so that they form nodal chains.

Besides being protected by symmetry, band crossings can be protected by topology too. In systems with broken TRS or inversion symmetry, there exist two-band crossings that can be locally described effectively by the Weyl Hamiltonian, thus the name of Weyl nodes [36, 139–145]. This effective theory is formally equivalent to the basic example of Berry curvature monopole; Weyl nodes are sources (sinks) of Berry curvature with topological charge +1 (-1). Following the Nielsen-Ninomiya theorem, these crossings have to occur by pairs, though crystalline symmetry can increase the number of pairs. To this date, several examples of Weyl semimetals have been both predicted and identified [25, 33, 35, 36, 139–145]. The most remarkable feature of these materials are the Fermi arcs; open Fermi surfaces that connect the projection of Weyl nodes on the surface of the material.

Nodal lines also have a topological non-trivial structure [121, 146–148]. It has been shown that nodal lines can be characterized by a series of topological invariants [149]. One way to check that a nodal line is topologically protected is to see if a closed loop enclosing the nodal line is contractible until it disappears. This can be done by means of the Berry phase; if the calculation of the Berry phase on a loop that is linked to the nodal line is non-trivial (Berry phase equal to π), then the loop is non-contractible and the crossing is topologically protected. On the other hand, if the Berry phase was found to be trivial (Berry pahse equal to 0) then the nodal line would be topologically trivial. Topological nodal lines also display surface states [123, 124, 150–152], although they are not as robust as the Fermi arcs coming from Weyl nodes. In particular, spin-orbit coupling can break the nodal line degeneracy [153, 154].

4.3 Crystal and electronic structures

4.3.1 Symmetries and structure

CoS_2 crystallizes in SG $Pa\bar{3}$ (205). This is a non-symmorphic cubic Space Group, generated by $\{I|0\}$, $\{C_{2z}|\frac{1}{2}0\frac{1}{2}\}$ and $\{C_{31}|0\}$, whose combination produces glide symmetry planes, $\{m_x|1/2,1/2,0\}$, $\{m_y|0,1/2,1/2\}$ and $\{m_z|1/2,0,1/2\}$. Cobalt atoms sit in the 4a Wyckoff position, while sulfur atoms sit in the 8c Wyckoff position. The structure is shown in Fig. 4.1(a). Experimental measurements [155, 156] reveal that the system has ferromagnetic ordering, which mainly stems from the cobalt d orbitals. This is represented by red arrows on cobalt atoms in Fig. 4.1(a). Experimental measurements determine that the magnetization is on the (100) direction family. We choose the direction of the magnetization in the z direction, without loss of generality.

When taking into account magnetization, the symmetry of the system is lowered. The 3-fold axes are broken, as well as TRS. The only surviving unitary symmetries are the 2-fold screw $\{C_{2z}|\frac{1}{2}0\frac{1}{2}\}$, the glide $\{m_z|1/2,0,1/2\}$ and inversion symmetry. The screws in the x and y directions, as well as the glides orthogonal to x and y axis are preserved in combination with TRS. All these properties are summarized in its magnetic space group, which is Pb'c'a (No. 61.436) [67–69].

4.3.2 Electronic structures

To study the electronic structure, we performed density functional theory (DFT) calculations as implemented in the Vienna ab initio simulation package (VASP) [49–52]. As it was shown in previous studies [35, 157], the appropriate method to compute the electronic structure is the local spin density approximation (LSDA) with no Hubbard U correction [134], with the Dudarev simplified exchange correlation term, together with PAW pseudopotentials. We used a grid of 7x7x7 k-points for the self-consistent calculation.

The resulting band structures, with and without the effect of spin-orbit coupling are shown in Fig. 4.1(b) and Fig. 4.1(c). Notice that the bands below the Fermi level are polarized mainly in the direction of the majority spin (up, following the magnetization), with a small minority pocket at the R point, as experimentally demonstrated in Ref. [35].

Without SOC in a ferromagnet, the Schrödinger equation can be decoupled into spin up and spin down sectors where spin is labeled in the quantization axis of the ferromagnet. In one of the spin sectors, the symmetry thus appears to be the non-magnetic one $Pa\bar{3}$ (205), regardless of the orientation of the magnetization. This artifice breaks down when SOC is included. Since SOC interaction has small effect

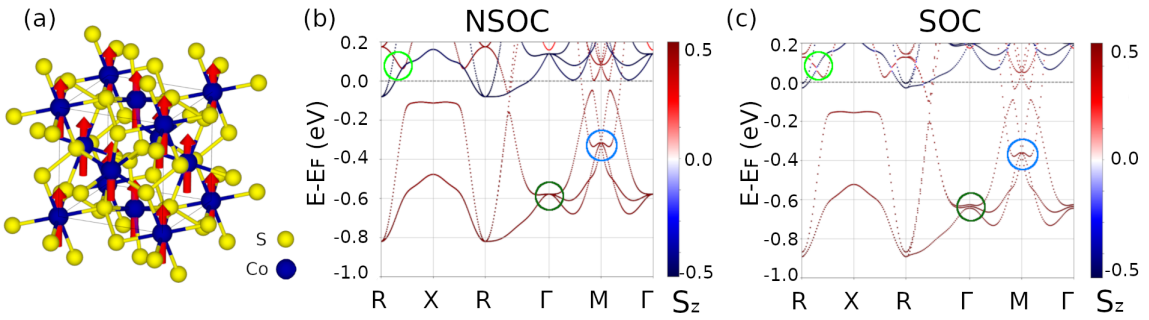

Figure 4.1: (a) Crystal and magnetic structure of CoS_2. (b) and (c) Electronic band structures near the Fermi level. (b) without and (c) with SOC interaction. Inside light green circles, effect of the SOC interaction mixing spins. Inside dark green circles, 3fold degeneracy breaking when symmetry is lowered due to the SOC interaction. Inside blue circles, symmetry enforced 4fold degeneracy.

on the band structure (see Fig. 4.1(b) and Fig. 4.1(c)), we expect the symmetry breaking effects to be small. In the band structure plots shown in Fig. 4.1(b) and Fig. 4.1(c), SOC couples both spins and opens gaps when spin-up and spin-down bands meet (see light green circles). In addition, the 3-fold degeneracy at the Γ point in the SOC-free plot is lifted when including SOC (see dark green circles). As expected, the gaps are small.

4.4 Effective 4-fold $\mathbf{k}\cdot\mathbf{p}$ model

In Fig. 4.1 (b) we see that there is a 4-fold degeneracy near the Fermi level in k-point $M = (\frac{1}{2}, \frac{1}{2}, 0)$ (see blue circles), which survives the addition of SOC as shown in Fig. 4.1 (c). Since we are interested in band crossings close to the Fermi level, we analyse this degeneracy. It is a symmetry-protected degeneracy, following the 4-dimensional irreducible co-representation at the M point. Following Group Theory tools, we can construct the most general, symmetry allowed, low-energy Hamiltonian that describes the 4-fold degeneracy in the vicinity of the M point. The resulting $\mathbf{k}\cdot\mathbf{p}$ Hamiltonian at first order in momentum and magnetization reads

$$H(\boldsymbol{k}) = B_x \boldsymbol{f}\cdot\boldsymbol{\sigma}\otimes\tau_3 + k_x v_x B_z \sigma_0\otimes\tau_1 + k_y \boldsymbol{v_y}\cdot\boldsymbol{\sigma}\otimes\tau_1 + k_z v_z \sigma_0\otimes\tau_3, \tag{4.1}$$

where momentum $\boldsymbol{k} = (k_x, k_y, k_z)$ is measured from M, σ, τ are Pauli matrices, B_x is the magnetic field in the x direction and $\boldsymbol{f}, v_x, \boldsymbol{v_y}, v_z$ are undetermined constants. This resembles the Hamiltonian of a Dirac fermion, but there are two main differences:

first, the momentum-independent $B_x \boldsymbol{f}\cdot\boldsymbol{\sigma}\otimes\tau_3$ term, which gaps the 4-fold when $B_x \neq 0$ and second that both k_x and k_y go with τ_1 and there is no τ_2, so the resulting energy dispersion does not result in a 3D cone:

$$E(\boldsymbol{k}) = \pm\sqrt{(B_x f)^2 + (v_x B_z k_x + v_y k_y)^2 + (v_z k_z)^2} \tag{4.2}$$

where $f = \sqrt{\boldsymbol{f}^2}$ and $v_y = \sqrt{\boldsymbol{v}_y^2}$. To see that this is not a cone, we can do a rotation of coordinates such that $k_1 = v_x B_z k_x + v_y k_y$ and k_2 is orthogonal to k_1 and lies in the $k_z = 0$ plane. In that case, the resulting energy dispersion would be cone-like in k_1, k_z but completely flat in k_2. Thus, we cannot compute topological quantities such as the Chern number of half-filled bands, because they are completely degenerate in the k_2 direction.

Furthermore, we can rotate the model to find the corresponding $\mathbf{k}\cdot\mathbf{p}$ model in the other M points, $M_2 = (\frac{1}{2}, 0, \frac{1}{2})$ and $M_3 = (0, \frac{1}{2}, \frac{1}{2})$. $\{C_{31}|0\}$ symmetry transforms momentum and magnetization in the same way, $C_{31}(k_x, k_y, k_z) = (k_z, k_x, k_y)$ and $C_{31}(B_x, B_y, B_z) = (B_z, B_x, B_y)$. Then,

$$\begin{cases} C_{31}M_1 = C_{31}(\frac{1}{2}, \frac{1}{2}, 0) = (0, \frac{1}{2}, \frac{1}{2}) = M_3 \\ C_{31}B_x = C_{31}(B, 0, 0) = (0, B, 0) = B_y \\ C_{31}M_3 = C_{31}(0, \frac{1}{2}, \frac{1}{2}) = (\frac{1}{2}, 0, \frac{1}{2}) = M_2 \\ C_{31}B_y = C_{31}(0, B, 0) = (0, 0, B) = B_z. \end{cases} \tag{4.3}$$

Notice that the momentum independent term that goes with B_x in M_1 will go with B_z in M_2. Since we have chosen the direction of the magnetization in the z axis, we predict that the 4fold will gap in the M_2 point. We confirmed this by computing the energy bands in the 3 M_i points (see Fig. 4.2 (a)) and we found two of them degenerate (M_1, M_3) and one with a gap of 5.5meV, as shown in Fig. 4.2 (b). The size of the gap is directly related to the energy scale of the SOC interaction. Thus, as SOC effect is small, the gap opening is small too.

Apart from 4-fold degeneracy at the M_1 and M_3 points, we also found that the planes $k_x = \pm 0.5$ and $k_y = \pm 0.5$ only have 2-dimensional magnetic irreducible co-representations. This implies that the bands will always be 2-fold degenerate at those planes, thus, they are Nodal planes. However, due to the presence of inversion symmetry, they will not have topological charge [128].

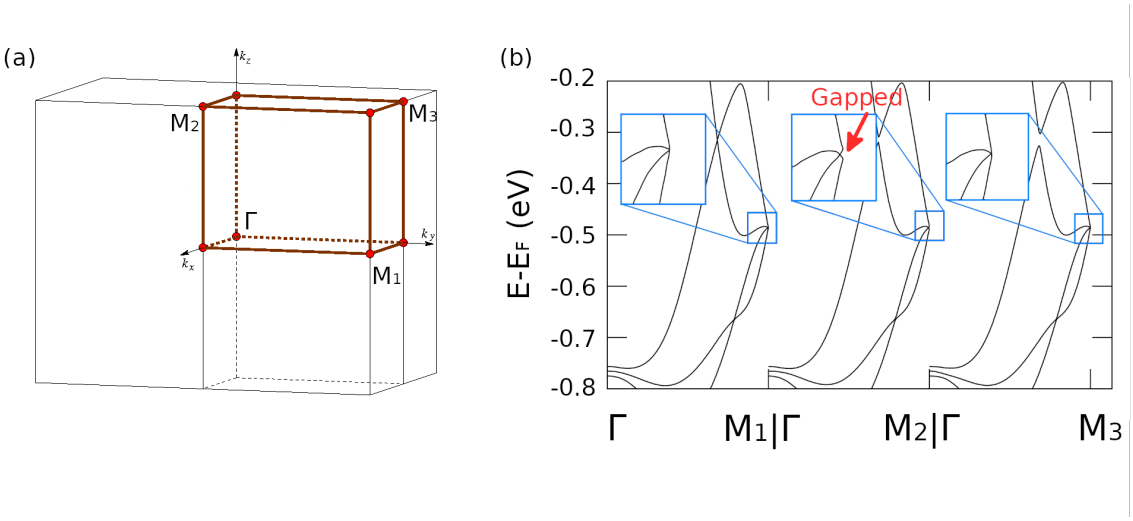

Figure 4.2: (a) Brillouin zone of the MSG Pb'c'a (No. 61.436) depicting the position of unequivalent M_i points (extracted from the BCS). (b) Dispersion from Γ to the different M_i points. The red arrow indicates the gap opening in M_2, as predicted by the $\mathbf{k} \cdot \mathbf{p}$ model.

4.5 Topological analysis: Nodal lines and Weyl nodes

We now study the topological properties of CoS_2 focusing on both Weyl nodes and Nodal lines. The calculations in what follows are based on the interpolated Tight Binding model in the Wannier basis [56] constructed from VASP ab-initio calculation [49–52]. We performed Berry phase calculations, as well as surface calculations as implemented in WannierTools [158].

We focus on the crossings between the last two valence bands near the Fermi level (the two top bands polarized in the majority spin in Fig. 4.1(c)). We found two nodal lines, one in the plane $k_z = 0$ and another one in $k_z = \pi$. Both planes are left invariant by $\{m_z|1/2, 0, 1/2\}$ (see Fig. 4.3(a)), which is the symmetry that protects both Nodal lines. In order to characterize the topological protection of the Nodal line, we computed the Berry phase around a loop enclosing it. The location of the Berry phase integration paths (red rectangles) is shown Fig. 4.3(a). Each red rectangle represents an integrated Berry phase of π, thus, non-trivial Z_2 index. We conclude that the Nodal lines in both planes are topologically protected.

In Fig. 4.3 (b) we show the projection of both Nodal lines in the (001) direction. We showed that the Nodal lines are topologically protected, but which region of the $k_z = 0$ plane will host surface states depends on the choice of cell origin [159]. We fix

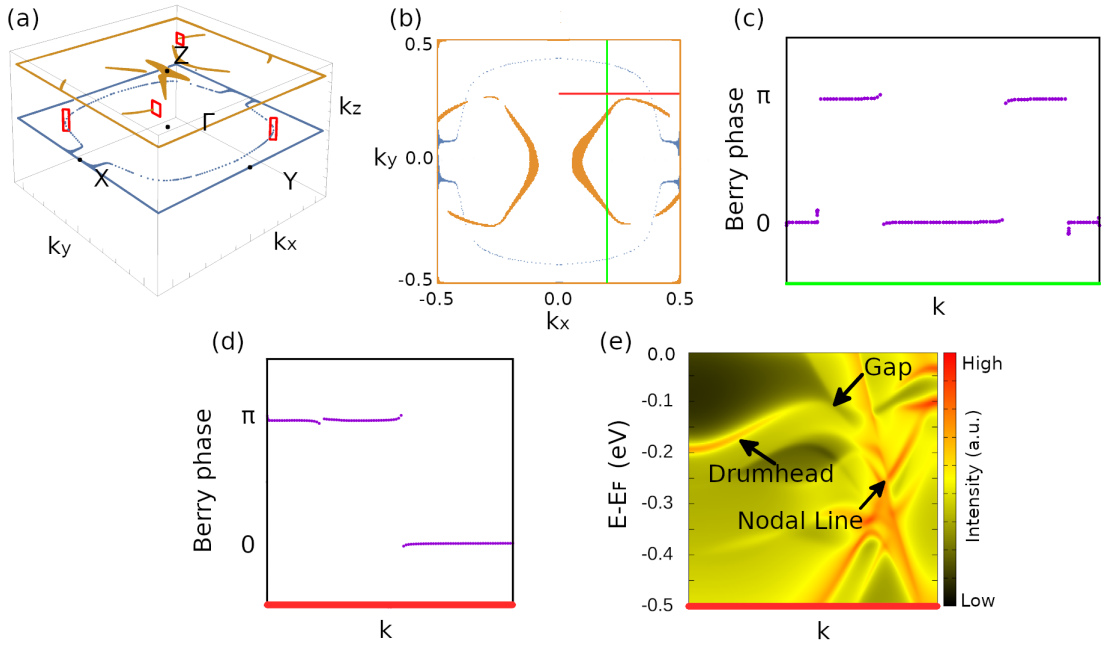

Figure 4.3: (a) Position of the Nodal lines in the BZ. Each red rectangle represents an integrated Berry phase of π. (b) Projection of the Nodal lines in the (001) direction. (c) and (d) Berry phase calculations on the paths depicted in (b). (e) Surface calculation in the (001) cleavage plane, computed along the red path shown in (b). Notice that the drumhead surface states gap in regions where the Berry phase is equal to 0.

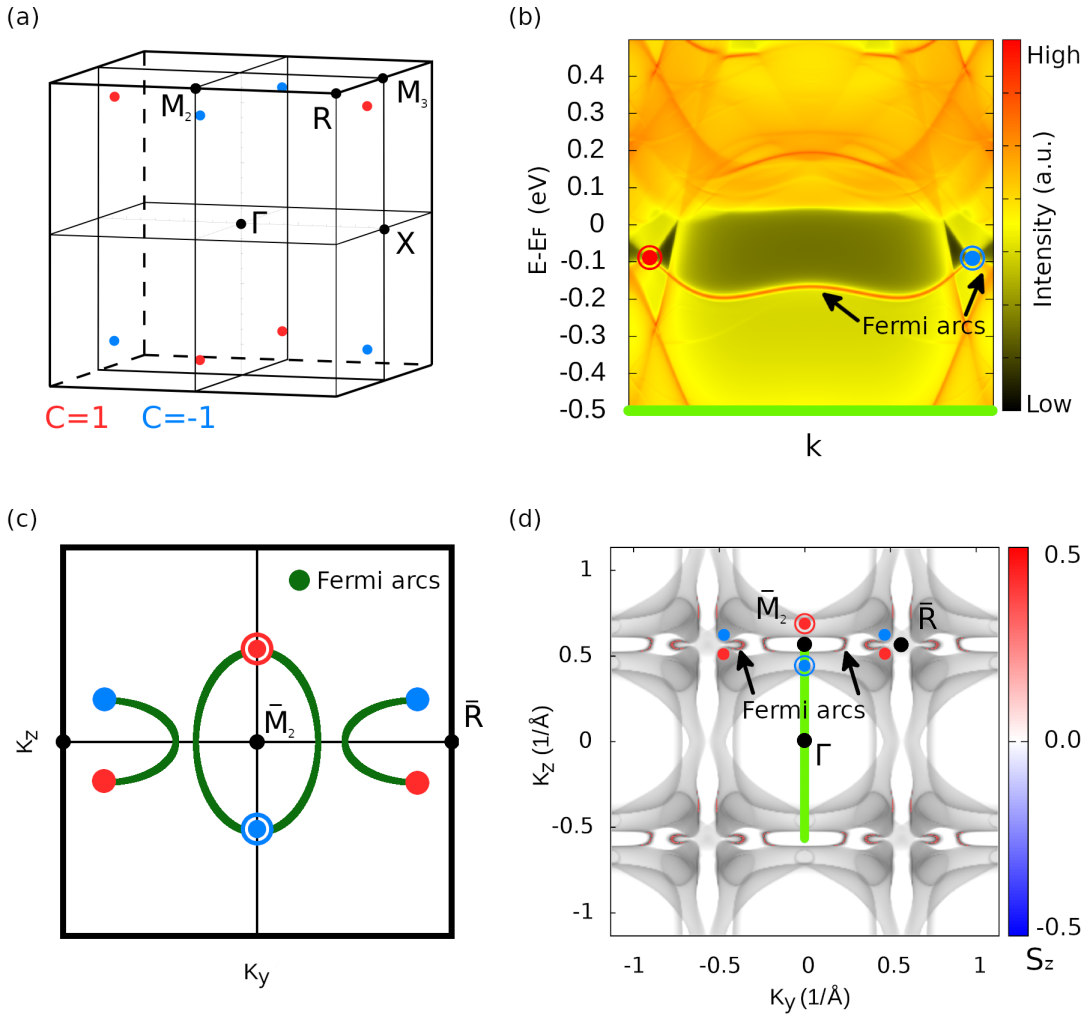

Figure 4.4: (a) Position of the Weyl nodes in the BZ. (b) Surface calculation in the (100) cleavage plane in the path depicted in (d). (c) Zoomed-in schematic depiction of the surface states in the (100) cleavage plane near the $\bar{M}_2$-$\bar{R}$ line. The location of the projection of the Weyls into the surface is shown by red and blue dots. Dots with a surrounding circle represent the projection of two Weyl nodes with equal chirality. (d) Spin polarization of Fermi arcs in the surface calculation. They are polarized in the direction of the majority spin, just like the bulk bands.

our unit cell as shown in Fig. 4.1 (a). We compute the Berry phases (integrating on k_z) along the momentum paths depicted in Fig. 4.3 (b). The results of the calculation are shown in Fig. 4.3 (c) and Fig. 4.3 (d). The calculations show that the Berry phase inside the blue Nodal line is equal to π, while the Berry phase outside, or inside the projection of both Nodal lines is equal to 0. Thus, the inside of the blue Nodal line is the non-trivial region, with expected drumhead surface states, while the rest of the regions are trivial. Berry phase calculation in Fig 4.3 (d) and surface spectrum calculation in Fig. 4.3 (e) are done in the same momentum path, as depicted in Fig. 4.3 (b). We performed the surface spectrum calculation via the Green's function iterative method [160], building a semi-inifinite slab as implemented in WannierTools [158], based on the effective Tight Binding model in the Wannier basis [56] constructed from VASP ab-initio calculation [49–52] We observe that drumhead surface states survive only in regions where the Berry phase of Fig. 4.3 (d) is equal to π, while they gap in regions where it is equal to 0.

By carefully examining the region close to the Fermi level we found a total of 8 Weyl points close to the Fermi level, whose location in momentum space is displayed in Fig. 4.4 (a). In Fig. 4.4 (b), we show (100) surface spectrum for $k_y = 0$, along the momentum path depicted in Fig. 4.4 (d) in green. In this path, we cross the projection of 4 Weyl nodes, projected pairwise with the same chirality. We can see two bright surface states that connect the projection of the Weyl nodes, one within the BZ and the other going through the boundary. Notice that Fermi arcs connect Weyl nodes across the boundary of the BZ but they avoid the Nodal planes, which are located at $k_y = \pm\pi$. In the (100) cleavage plane, we can observe 4 different Fermi arcs as depicted in Fig. 4.4 (c). The Fermi arc close to the $\bar{R}$ point connects the projection of two opposite chirality Weyl nodes. Near the $\bar{M}$ points, though, we can see two Fermi arcs connecting the projections, instead of one. This is due to pairs of Weyl nodes (with the same chirality) being projected in the same point. In Fig. 4.4 (d), we see the Fermi surface calculation on the (100) surface, schematized in Fig. 4.4 (c). The connection of the Fermi arcs is the same one as in the scheme of Fig. 4.4 (c), with single Weyl nodes connected by a single Fermi arc and double Weyl nodes connected by two Fermi arcs. From the ab initio calculation we know that the bands in the relevant energy window are predominantly polarized in the direction of the majority spin. We computed the spin polarization of the Fermi arcs to see if they inherit the polarization from the bulk. We show in Fig 4.4 (d) that the Fermi arcs are completely polarized in the direction of the majority spin, as is the case in the bulk.

There are several proposed applications for topological semimetals. In the field of quantum optics, it has been shown that Weyl semimetals could be used to realize a Veselago lens for electrons [38] (negative refractive index). It has also been confirmed experimentally that Weyl semimetals have a quantized circular photogal-

vanic effect [40, 161] due to their topological charge. In the field of electronics, Weyl semimetals show signatures of the Chiral anomaly. There are materials that show a large magnetorresistance, such as the family of TaAs [143], which can be harnessed for the next generation of memory devices. The spin polarization of the Fermi arcs can also influence the performance of a Weyl semimetal as a spin injector, improving the expected bulk results [39].

4.6 Experimental results

In this section we will compare the theoretical predictions we made to recent angular resolved photo-emission spectroscopy (ARPES) experimental results. This work has been carried out by the teams lead by Niels Schröter (MPI Halle) and Leslie Schoop (Princeton University).

In order to measure the bulk electronic band structure, two distinct cleavage planes were obtained, one with a surface normal pointing along (111) and the other one pointing along (100). They performed photon energy-dependent ARPES measurements with soft X-ray photons ($h\nu = 350 - 800$ eV) to locate the high-symmetry planes along the k_z direction normal to the sample surface. For the data measured on the (111) cleavage plane in Fig. 4.5 (a), we can clearly identify circular Fermi surface pockets at the R point in the corner of the Brillouin zone. Our calculated Fermi surface (following the methods described in Sec. 4.5) in Fig. 4.5 (b) is in good qualitative agreement with the experimental data, confirming the existence of Fermi surface pockets at the point. When inspecting the experimental band dispersion along the R-X-R direction (see Fig. 4.5 (c)), we see that the circular pockets at the R point are electron-like, and are related to another parabolic band with a minimum at around 0.65 eV by the exchange splitting. The magnitude of the exchange splitting extracted from the energy distribution curve at the R point (see Fig. 4.5 (d)) is ΔE = 0.60(3) eV. Our LSDA calculations of the band dispersion shown in Fig. 4.5 (e) are in good qualitative agreement with the experimental data and indicate that the observed electron pocket is of minority-spin character, which implies that CoS2 is not a true half-metal. However, the experimentally observed exchange splitting is approximately 250 meV smaller than in the LSDA calculations, such that the majority spin-bands are located closer to the Fermi-level in the experiment than expected from the calculations.

To search for the topological Nodal line and Weyl-nodes in CoS2, they also probed the bulk band structure in both cleavage planes containing the Γ point. Fig. 4.6 (a-d) display the experimental and calculated Fermi-surfaces for the (111) and (100) cleavage planes containing the Γ point, which are in good qualitative agreement. Fig. 4.6 (e) shows the band dispersion along the $M - \Gamma$ direction measured on the

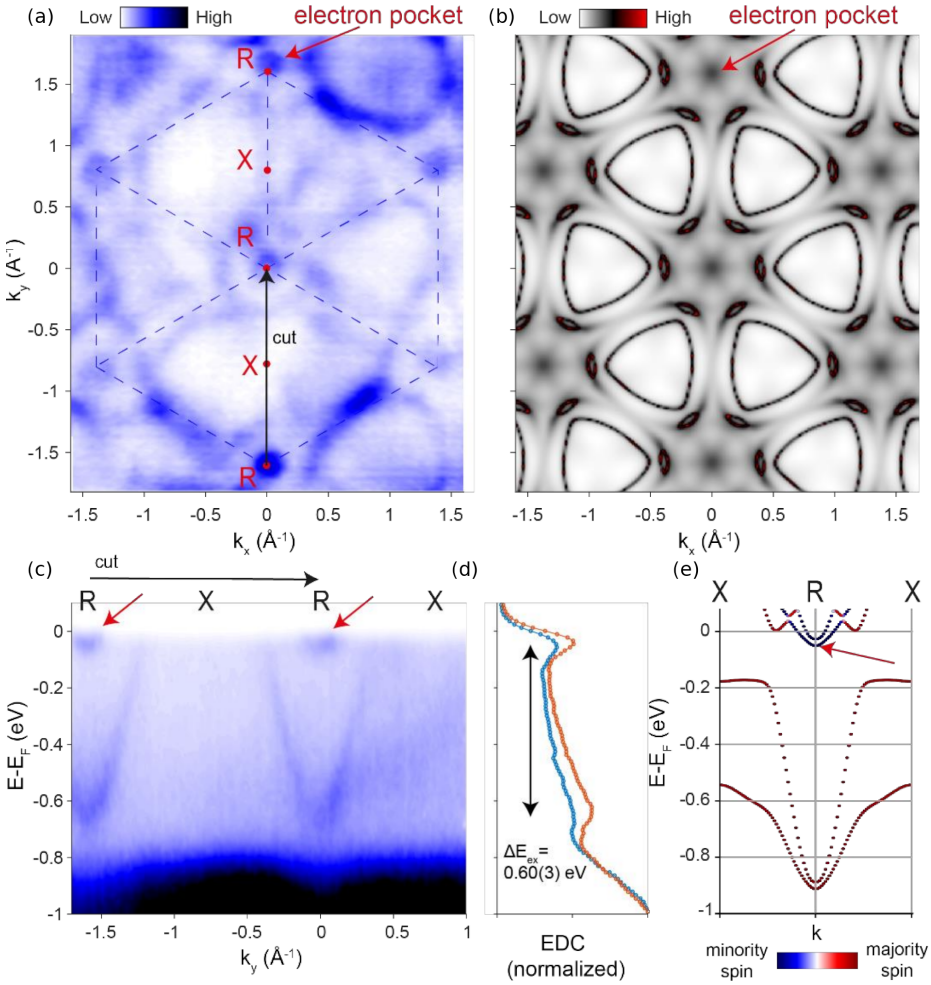

Figure 4.5: (a) ARPES Fermi surface on the (111) cleavage plane that cuts R. We can identify circular electron pockets centered at the R point. (b) Ab initio calculation on the same cleavage plane as (a). We observe that there is qualitative agreement between experimental and theoretical calculations. (c) Experimental band dispersion on the k path depicted in (a) (black arrow). Red arrows depict electron pockets at the R point. (d) Experimental energy distribution curve at the R point. From here we extract the value of the exchange splitting ($\Delta E = 0.60(3)$ eV). (e) Ab-initio calculation of bands in the same direciton as (c). We confirm that the electron pocket in R is polarized in the direction of the minority spin.

(111) surface (black arrow in Fig. 4.6 (a)), and the $\Gamma - M$ direction, measured on the (100) surface (black arrow in Fig. 4.6 (c)). Note that the observable bands along these two directions are very different, possibly due to matrix element effects. The line cut obtained from the (111) surface shows a V-shaped feature centered at the M point, and a quasi-parabolic band centered at the Γ point. In contrast, the dispersion obtained from the (100) surface shows a single band dispersing in the opposite direction from the quasi-parabolic band. To enhance the contrast of our data, we also show the corresponding second derivative spectrum in Fig. 4.6 (f). The combined band dispersion from both surfaces is illustrated in Fig. 4.6 (g), which displays the peak positions from a fit of the momentum distribution curves (MDCs).

By comparison with the calculated band dispersion shown in Fig. 4.6 (h), we can see that the band crossing between the blue and red bands (from the (111) surface and (100) surface, respectively) is part of a topological nodal line, while the blue bands form a cone-like dispersion. The Weyl node that corresponds to the cone-like dispersion is shown in Fig. 4.6 (i), which displays the calculated band dispersion along the $M^* - \Gamma$ direction, where $M^* = (0.5, 0.458, 0.0)$ is a point that is slightly displaced from M, such that we cross the Weyl node, which is identical to the M point within the experimental uncertainty. Since we cannot observe the band top of the blue bands along the $M - \Gamma$ direction in the experimental data, we conclude that the Weyl node must be located slightly above (but very close to) the Fermi-level.

To detect the theoretically predicted Fermi arcs, they used surface-sensitive VUV-ARPES to investigate the surface electronic structure of the (100) surface in CoS_2. Fig. 4.7 (a) shows the experimentally obtained Fermi-surface, which was measured on a strongly tilted crystal plane. Comparing to the LSDA calculation in Fig. 4.7 (b), we can clearly identify the Fermi arcs around $\bar{M}_2$, while the ones close to the $\bar{R}$ point are not visible. In Fig. 4.7 (c) we show the experimental line-cut in the direction depicted in Fig. 4.7 (a) (black arrow). It displays a surface state band crossing the Fermi level that connects two hole-like pockets that are located at the points at opposite ends of the Brillouin zone. Comparing to the LSDA calculated surface spectrum (see Fig. 4.7 (d)), we conlcude that those states are in fact Fermi arcs. Note that the renormalized energy scale of the Fermi arcs in the calculation compared to the experiment is expected due to the reduced exchange splitting, which we already observed for the bulk band structure. Therefore, the Fermi arcs cross the Fermi-level in the experiment, while they are located below the Fermi-level in the calculation.

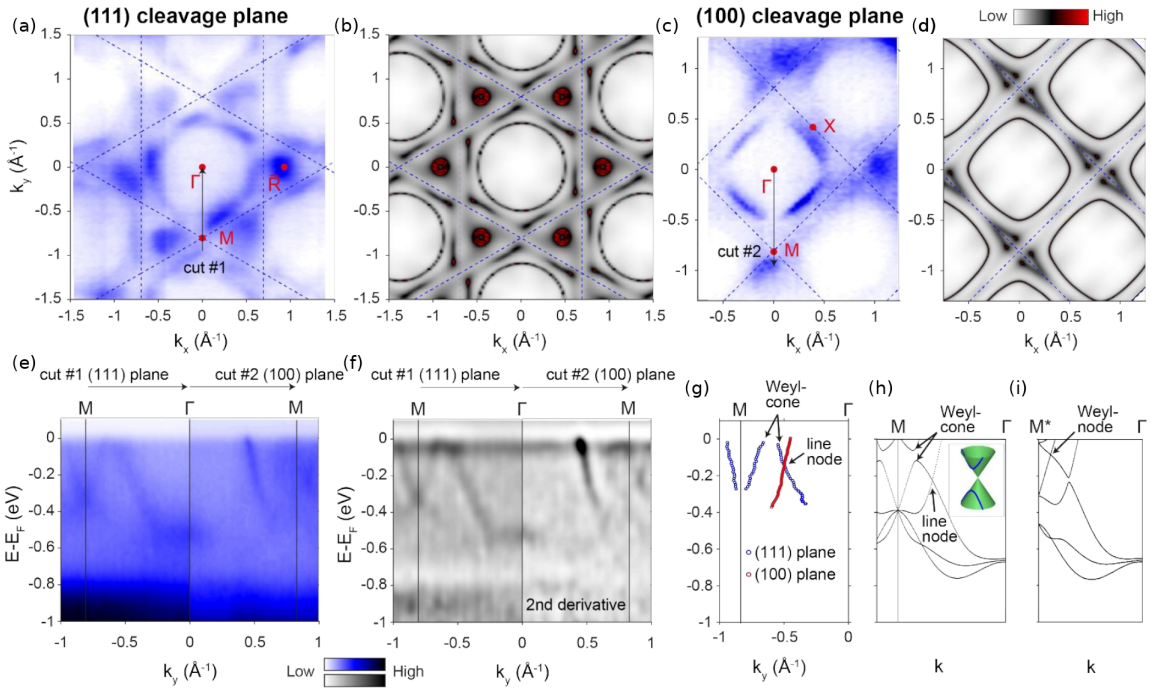

Figure 4.6: (a-d) Experimental vs ab-initio calculation of Fermi surfaces. (a-b) On the (111) cleavage plane that cuts Γ. Ab-initio calculation shows qualitative agreement. (c-d) On the (100) cleavage plane that cuts Γ. Ab-initio calculation shows qualitative agreement. (e) Line cuts of the $M - \Gamma$ path extracted from both (111) and (100) cleavage planes. We clearly see the location of the 4fold degeneracy. (f) Second derivative of the spectrum in (e), improving contrast. (g) Combined band dispersion from both cleavage planes, showing the location of the Nodal line and the Weyl node. (h-i) Ab-initio calculation of bands in two close paths. (h) Location of the Nodal line. (i) Location of the Weyl node. Notice that the separation of the two paths is smaller than experimental accuracy.

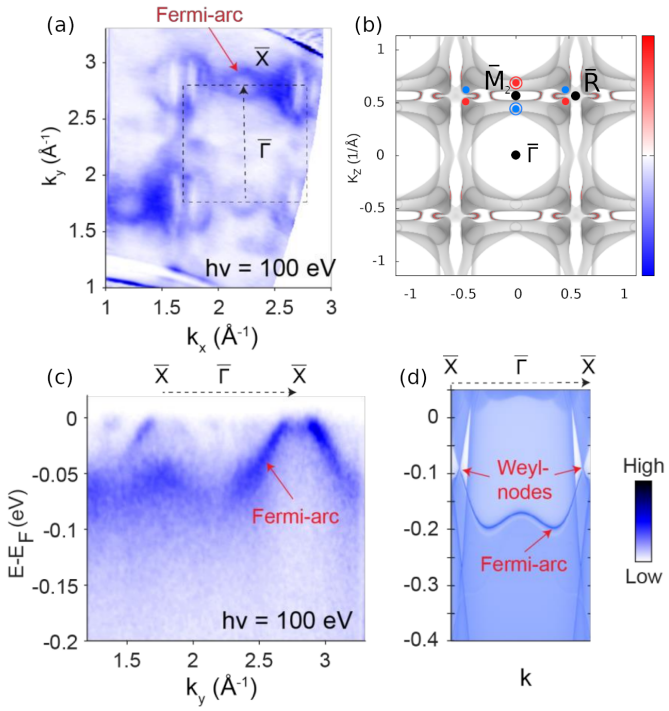

Figure 4.7: (a) Fermi surface calculation of surface spectrum in the (100) cleavage plane. We indicate the location of the Femri arcs experimentally observable. (b) Ab-initio Fermi surface calculation of surface spectrum in the (100) cleavage plane, showing the location of Fermi arcs. (c) Line cut of experimental band spcetrum in the direction depicted in (a) (black arrow). Red arrow shows the location of one of the Fermi arcs. (d) Ab-initio calculation showing the Fermi arcs connecting Weyl nodes. There is good agreement between experimental data and ab-initio calculations.

4.7 Conclusions

In this work we revisited the recently discovered Weyl semimetal CoS_2 ferromagnetic pyrite. We analyzed both Nodal lines and Weyl nodes found on the ferromagnetic system. We found two nodal lines close to the Fermi level, with surface drumhead states in the (001) surface. We also found a family of Weyl nodes close to the Fermi level, with their distinctive Fermi arcs on the (100) surface. Compared to trivial dangling bond surface states, Fermi arc surface states are more robust against attempts of passivation, because they are protected by the topological invariants (Chern numbers, chirality) of the bulk Weyl nodes; hence engineering of the interface potential cannot easily remove the Fermi arcs. These surface states increase the number of available electrons in the surface, thus improving its metallic properties for junctions. Follow-

ing the spin polarization in the direction of the majority in the bulk, we checked if the Fermi arcs are polarized in the same direction too, being this one of the few example of spin polarized Fermi arcs in real materials [30]. The Fermi arcs would contribute to the spin majority polarization, making it an interesting material for spintronics, like a possible spin injector [31]. Therefore, CoS_2 provides a prime example of a spintronic material whose performance is affected by its topologically nontrivial band structure.

CoS_2 is also known to be a good catalyst, e.g. for the hydrogen evolution reaction [29], and it has recently been speculated that Fermi arcs in Pt- and Pd-based chiral topological semimetals [110, 162] may play a role in catalysis due to their d-electron character and their robustness against hydrogen passivation [163]. Since the Fermi arcs in CoS_2 are also derived from bulk bands of d-orbital character (see supplementary), they might contribute to the catalytic performance of CoS_2.

Finally, our findings of new Physics on this extensively studied 'old' material raise the idea that we should continue looking for new phenomena in already well established materials, which, apart from having some well known properties, are more easily growable in the lab or encountered in nature.

Chapter 5

Breaking symmetries with strain: Hall viscosity

Apart from magnetization, there are other physical phenomena that can lower the symemtry of a system, possibly changing its topological porperties. In this chapter, we will analyze the effect time-dependent strain has on one type of the multifold fermions described in the introduction: the threefold fermion. We will focus on the 3-fold fermion realized in cubic systems, such as SG $P2_13$ (198), with topological charge $C = 2$. In what follows, we analyze the response of this 3-fold fermion to time-sependent strain. During the research, we found a new, fundamentally 3 dimensional Hall viscosity. We develop a model to analytically compute this new viscosity on a toy model, to later generalize in which families of real materials it could be found. The main results have been published in [164].

5.1 Introduction

One of the most important properties of topological systems is the robustness of the topological indices. Since they are left invariant under small, adiabatic perturbations of the system, physical properties that are directly dependent on them share this robustness. The already classical example of this robustness is the Integer Quantum Hall effect, which, if the necessary experimental conditions are met [165], can be typically measured with an error of few parts per billion [166]. This is why Quantum Hall Resistivity (QHR) was used to define the resistivity standard. The reason behind the extraordinary quantization of the QHR is that this quantity is proportional to a topological invariant; the first Chern number. Thus, this effect, that is not material dependent, can be measured with high precision even in "dirty" samples, making it reachable for different samples and widely reproducible.

Then, it is natural to ask if there exist other transport quantities that are tied to topological invariants. Examples of this are the Quantized Circular Photogalvanic Effect, a photocurrent whose response is quantized in Weyl semimetals [161] and the dissipationless odd Hall viscosity in 2D [167], which is quantized in Chern insulators. In this chapter, we will study the antisymmetric response of a multifold fermion with Chern number $C = 2$ to strain, the Hall viscosity. Although we found it not to be quantized, it can still be measured in systems measuring the local flow profiles or thermoelectric transport coefficients in chiral magnets.

Classically, the relation between the stress and strain tensors can be described as follows:

$$T_{\alpha\beta} = \xi_{\alpha\beta\mu\nu} u_{\mu\nu} + \eta_{\alpha\beta\mu\nu} \dot{u}_{\mu\nu}, \tag{5.1}$$

where u is the strain tensor, $\dot{u}$ is the strain rate tensor (time-derivative of strain tensor), ξ is the elastic modulus and η is the viscosity tensor. The part of the viscosity tensor that is antisymmetric ($\eta^A_{\alpha\beta\mu\nu} = -\eta^A_{\mu\nu\alpha\beta}$) is called Hall viscosity, and gives rise to a dissipationless force.

In rotationally invariant 2D fluids, there is a single Hall viscosity coefficient, related to the topological properties of the occupied electronic states [168–176]. Analogous to the QHE, the Hall viscosity is proportional to the integral of an adiabatic curvature and is proportional to the Chern number. Then, it is quantized in 2D Chern insulators. In clean systems, the Hall viscosity manifests in width-dependent corrections to the Hall conductance of mesoscopic channels, backflow corrections to the local current density near point contacts, and in moments of the semiclassical distribution function [177–180]. Local voltage measurements on graphene samples in magnetic fields have shown signatures of the Hall viscosity [181]. Hall viscosity also appears in classical fluids with broken TRS like chiral active fluids [182, 183]. This "momentum" Hall viscosity (MHV), describes a stress response that can be related to a change in momentum density. The momentum Hall viscosity contains meaningful information even beyond the hydrodynamic regime [168, 184–186].

In parallel, a related geometric response coefficient (the phonon Hall viscosity (PHV)) has gained attention. A response to dynamic strains via electron-phonon coupling, and also a rank four tensor, the PHV is expected to appear in the dispersion for acoustic phonons [185, 187], and in spin-phonon coupled systems through a contribution to thermal Hall conductance [188–191].

Beyond 2D, the role of nondissipative viscosity in transport remains largely unexplored. Reports of hydrodynamic behavior in TSMs [192], and the growing interest in magnetic TSMs [193], raise the question of how to generalize the Hall viscosity to 3D. Preliminary efforts have focused on quasi-2D transport [194–200], or made use of preferred "polar" directions such as the Weyl node separation direction in

TSMs. Furthermore, octahedral symmetry forbids the presence of a nonzero Hall viscosity [184, 201]. However, magnetic crystals may have nonpolar point group symmetries that are not octahedral; the nondissipative geometric response of such systems remains an open question.

Looking beyond 2D, in this chapter we find that tetrahedral symmetry allows for the appearance of a new, fundamentally 3D "cubic" Hall viscosity. To our knowledge this has not been encountered before in the literature, and could be realized in a wide array of classical and quantum fluids with broken TRS. For uniaxial flows, this new viscosity gives raise to a force perpendicular to the flow direction which vanishes when the velocity is constant along the direction of flow. As a proof-of-principle, we focus on a toy model in the experimentally interesting case of the cubic MSG $P2_13$ (No. 198.9), with TRS breaking chiral magnetism. Chiral multifold fermions such as these act as point sources of Berry curvature in the Brillouin zone [63, 202–209], making them ideal models to explore topological response functions [204, 210–212]. We compute the MHV and PHV for this model. For the PHV, we consider an electron-phonon coupling ansatz to derive the "phonon" strain coupling [185,187,199,213,214] which will yield a resulting "phonon" stress tensor. For the MHV, we use the recently introduced lattice formulation of stress response [176] to derive a coarse-grained strain coupling corresponding to a conserved momentum density. Using the Kubo formula for viscosity [175], we derive both the MHV and PHV for a spin-1 fermion. We discuss the implication of our work for chiral magnetic TSMs such as the family Mn_3IrSi, Mn_3IrGe, $Mn_3Ir_{1-y}Co_ySi$, and $Mn_3CoSi_{1-x}Ge_x$ [193, 215, 216] in MSG $P2_13$ (No. 198.9).

5.2 Properties of Point Group 23

Before we move on to compute the Hamiltonian of the system and derive the stress tensors, we review the properties of Point Group 23, the Point Group associated to SG $P2_13$ (198). We will describe the representations of 23 and their products. This will allow us to identify the possible Hall viscosity components, and also provide a way of writing down the most general, symmetry allowed strained Hamiltonian necessary for the phonon-stress approach.

The set of generators we choose for the Point Group 23 is, in the vector representation V,

$$V(C_{2z}) = \begin{pmatrix} -1 & 0 & 0 \\ 0 & -1 & 0 \\ 0 & 0 & 1 \end{pmatrix}, \quad V(C_{2y}) = \begin{pmatrix} -1 & 0 & 0 \\ 0 & 1 & 0 \\ 0 & 0 & -1 \end{pmatrix}, \quad V(C_{3_1}^-) = \begin{pmatrix} 0 & 1 & 0 \\ 0 & 0 & 1 \\ 1 & 0 & 0 \end{pmatrix}. \tag{5.2}$$

The character table for the representations of 23 can be found below:

(23) (T)	E	C_{2i}	C_{3j}^{-}	C_{3j}^{+}
A	1	1	1	1
${}^2E$	1	1	w	w^*
${}^1E$	1	1	w^*	w
T	3	-1	0	0

Table 5.1: Character table for Point Group 23. $w = e^{2\pi i/3}$. Notice that the vector representation subduces to the T irreducible representation.

In this chapter we use the following irreducible tensors for 23: the Kronecker delta δ_{ij}, the Levi-Civita symbol ϵ_{ijk} and two new tensors Θ and Λ, irreducible only for Point Group 23, which can be used to contract indices and thus take products of irreducible representations:

$$\begin{aligned}\Theta_{ij}^{a} &= \begin{cases} \frac{1}{\sqrt{3}}\left(\delta_{1i}\delta_{1j} + \delta_{2i}\delta_{2j} - 2\delta_{3i}\delta_{3j}\right) & a = 1 \\ \delta_{1i}\delta_{1j} - \delta_{2i}\delta_{2j} & a = 2 \end{cases} \\ \Lambda_{ijk} &= \begin{cases} 1 & i \neq j \neq k \\ 0 & else. \end{cases}\end{aligned} \tag{5.3}$$

Note that Θ carries an index $a = 1, 2$ relating to the two dimensional representation ${}^1E^2E$, which is physically irreducible as introduced in Chapter (2). Indices i, j, k represent coordinates in 3-dimensional space. By means of these tensors, we can write explicitly the Kronecker Product table of the group[1]

$$\begin{aligned}
&A(x) \otimes A(y) = A(xy) \\
&A(x) \otimes {}^1E^2E(y^a) = {}^1E^2E(xy^a) \\
&A(x) \otimes T(y_i) = T(xy_i) \\
&{}^1E^2E(x^a) \otimes {}^1E^2E(y^b) = A(\delta_{ab}x^a y^b) \oplus A(\epsilon_{ab}x^a y^b) \oplus {}^1E^2E(-x^1y^1 + x^2y^2, x^1y^2 + x^2y^1) \\
&{}^1E^2E(x^a) \otimes T(y_i) = T(x^1y_i) \oplus T(x^2y_i) \\
&T(a_i) \otimes T(b_j) = A(\delta_{ij}a_ib_j) \oplus {}^1E^2E\left(\Theta_{ij}^{a}a_ib_j\right) \oplus T(\Lambda_{ij}a_ib_j) \oplus T(\epsilon_{ijk}a_jb_k).
\end{aligned} \tag{5.4}$$

In the non-interacting regime, we can express Hamiltonians in the second quantization as combiantions of field bilinears. We can express these bilinears in terms of square matrices, with the following interpretation:

[1]Remember that the product of irreducible representations is commutative.

$$(\Psi^\dagger\Psi)^a = \Psi_i^\dagger \lambda_{ij}^a \Psi_j, \tag{5.5}$$

where a labels the different bilinears.

We can see how λ matrices transform from Ψ transformation rules. If we fix a bilinear, we can do the following:

$$\Psi_i^\dagger \lambda_{ij}^a \Psi_j \to \Psi_i^\dagger R_{ik}^{-1} R_{km} \lambda_{mn}^a R_{nl}^{-1} R_{lj} \Psi_j = \Psi_i'^\dagger R_{ik} \lambda_{kl}^a R_{lj}^{-1} \Psi_j', \quad \lambda_{ij}^a \to R_{ik} \lambda_{kl}^a R_{lj}^{-1}. \tag{5.6}$$

These are the transofmration rules λ^a matrices transform.

The multifold fermion we are interested in transforms under the T representation of 23, which is the little group of SG $P2_13$ at Γ. In this case, since our fermionic field is 3 dimensional, there will be $3 \times 3 = 9$ independent λ matrices. One can use the Gell-Mann matrices as a basis for bilinears, since they form a complete basis of 3x3 Hermitian matrices,

$$\begin{aligned}
&\lambda_0 = \begin{pmatrix} 1 & 0 & 0 \\ 0 & 1 & 0 \\ 0 & 0 & 1 \end{pmatrix}, \quad \lambda_1 = \begin{pmatrix} 0 & 1 & 0 \\ 1 & 0 & 0 \\ 0 & 0 & 0 \end{pmatrix}, \quad \lambda_2 = \begin{pmatrix} 0 & -i & 0 \\ i & 0 & 0 \\ 0 & 0 & 0 \end{pmatrix}, \\
&\lambda_3 = \begin{pmatrix} 1 & 0 & 0 \\ 0 & -1 & 0 \\ 0 & 0 & 0 \end{pmatrix}, \lambda_4 = \begin{pmatrix} 0 & 0 & 1 \\ 0 & 0 & 0 \\ 1 & 0 & 0 \end{pmatrix}, \quad \lambda_5 = \begin{pmatrix} 0 & 0 & -i \\ 0 & 0 & 0 \\ i & 0 & 0 \end{pmatrix}, \\
&\lambda_6 = \begin{pmatrix} 0 & 0 & 0 \\ 0 & 0 & 1 \\ 0 & 1 & 0 \end{pmatrix}, \ \lambda_7 = \begin{pmatrix} 0 & 0 & 0 \\ 0 & 0 & -i \\ 0 & i & 0 \end{pmatrix}, \ \lambda_8 = \frac{1}{\sqrt{3}} \begin{pmatrix} 1 & 0 & 0 \\ 0 & 1 & 0 \\ 0 & 0 & -2 \end{pmatrix},
\end{aligned} \tag{5.7}$$

to parametrize the Hamiltonian near the Γ point,for states spanning the spin-1 multifold fermion. At Γ, the basis states for this degeneracy transform under the irreducible representation T of 23. In the non-interacting picture (and in second quantization), the Bloch Hamiltonian is a matrix, which, as we said, is a bilinear form of the eigenstates near that point (Ψ) that transoforms in the $\bar{T}(\bar{\Psi}_i) \otimes T(\Psi_j) = T(\bar{\Psi}_i) \otimes T(\Psi_j)$ representation, where indices i, j label the states. Thus, the nine Gell-Mann matrices will transform under $T \otimes T$. Following the Kronecker Product table, we can write the subduced representation and symmetry adapted coordinates of the Gell-Mann matrices in the point group 23. We find

$$\rho^{\bar{\Psi}\Psi} \equiv \rho^\lambda = A(\lambda_0) \oplus {}^1E^2E(\lambda_8, \lambda_3) \oplus T(\lambda_6, \lambda_4, \lambda_1) \oplus T(\lambda_7, -\lambda_5, \lambda_2). \tag{5.8}$$

For simplicity of notation, we will use through the chapter the following names for the T representaitons:

$$\begin{aligned} \mathbf{L} &\leftrightarrow T(\lambda_7, -\lambda_5, \lambda_2) \\ \tilde{\mathbf{L}} &\leftrightarrow T(\lambda_6, \lambda_4, \lambda_1). \end{aligned} \tag{5.9}$$

Notice that $\mathbf{L}$ forms a Pauli vector of spin-1 matrices. Thus, they are not only a 3-dimensional irrep of 23 but of the whole SO(3) group. $\tilde{\mathbf{L}}$, though, does not, and only transforms as vector in Point Group 23. We also use the letter indices $a, b, c = 1, 2$ to write v_a, an element of the two dimensional representation ${}^1E^2E(\lambda_8, \lambda_3)$.

5.3 Threefold $\mathbf{k} \cdot \mathbf{p}$ model from Group Theory

We can exploit the Group Theory results in the previous section to write the most general, symmetry allowed $\mathbf{k} \cdot \mathbf{p}$ Hamiltonian of the threefold degeneracy at Γ. For that purpose, we will combine λ matrices with a general field[2], which will transform as a sum of the irreps of the group:

$$\rho^Q = A(Q_0) \oplus {}^1E^2E(Q^a) \oplus T(Q_i). \tag{5.10}$$

Hamiltonians, being energy, have to be scalars. In terms of Representation Theory, they transform under the identity or trivial representation. So the number of Hamiltonians we can construct is equal to the number of times the identity is contained in the representation product of bilinears and the general field.

T (23)	E	C_{2i}	C_{3j}^-	C_{3j}^+
ρ^λ	9	1	0	0
ρ^Q	6	2	0	0
$\rho^\lambda \otimes \rho^Q$	54	2	0	0

Table 5.2: Character table of the representations on the group T(23).

We can use the "Magic Formula" to compute the number of independent Hamiltonians allowed by symmetry (See Table 5.2):

$$m_{A_1} = \frac{1}{12}(54 + 2 \cdot 3) = 5, \tag{5.11}$$

[2]Notice that by combining bilinear with the general field we will obtain all possible Hamiltonians that are symmetry allowed. It might seem an overkill if we only want to know the first order in momentum $\mathbf{k} \cdot \mathbf{p}$ Hamiltonian, but it will let us generalize our Hamiltonian to any interaction immediately. It will be useful when trying to couple to magnetic field and strain.

so we have 5 independent Hamiltonians. These Hamiltonians come from the product of the representations ρ^{λ} and ρ^{Q}, explicitly,

$$\left(A(\lambda^0) \oplus {}^1E^2E(\lambda^a) \oplus T(\lambda_i^S) \oplus T(\lambda_i^A)\right) \otimes \left(A(Q_0) \oplus {}^1E^2E(Q^a) \oplus T(Q_i)\right). \tag{5.12}$$

Looking at the relations in equation (5.4), it is straightforward to see which are the Hamiltonians that we get:

$$\begin{aligned} &A(\lambda^0) \otimes A(Q_0) \to H_0 \propto Q_0\lambda^0 \\ &{}^1E^2E(\lambda^a) \otimes {}^1E^2E(Q^b) \to H_1, H_2 \propto \delta_{ab}\lambda^a Q^b,\ \epsilon_{ab}\lambda^a Q^b \\ &T(\lambda_i^S) \otimes T(Q_j) \to H_3 \propto \delta_{ij}\lambda_i^S Q_j \\ &T(\lambda_i^S) \otimes T(Q_j) \to H_4 \propto \delta_{ij}\lambda_i^A Q_j. \end{aligned} \tag{5.13}$$

The most general Hamiltonian we can build will be a linear (complex) combination of these pieces. Written in matrix form for a clearer understanding:

$$\begin{aligned} &\alpha_0 \begin{pmatrix} Q_0 & 0 & 0 \\ 0 & Q_0 & 0 \\ 0 & 0 & Q_0 \end{pmatrix} + \alpha_1 \begin{pmatrix} \frac{1}{\sqrt{3}}Q_1 + Q_2 & 0 & 0 \\ 0 & \frac{1}{\sqrt{3}}Q_1 - Q_2 & 0 \\ 0 & 0 & -\frac{2}{\sqrt{3}}Q_1 \end{pmatrix} + \\ &\alpha_2 \begin{pmatrix} \frac{1}{\sqrt{3}}Q_2 - Q_1 & 0 & 0 \\ 0 & \frac{1}{\sqrt{3}}Q_2 + Q_1 & 0 \\ 0 & 0 & -\frac{2}{\sqrt{3}}Q_2 \end{pmatrix} + \alpha_3 \begin{pmatrix} 0 & Q_5 e^{-i\omega} & Q_4 e^{i\omega} \\ Q_5 e^{i\omega} & 0 & Q_3 e^{-i\omega} \\ Q_4 e^{-i\omega} & Q_3 e^{i\omega} & 0 \end{pmatrix}. \end{aligned} \tag{5.14}$$

where all coupling constants are now real $(\alpha_0, \alpha_1, \alpha_2, \alpha_3, \omega)$ and we have imposed hermiticity. Also, to simplify notation, we have used that $\alpha_1' H_1 + \alpha_2' H_2 = \alpha_1(H_1 + H_2) + i\alpha_2(H_2 - H_1)$ and $\alpha_3' + i\alpha_4' = \alpha_3 e^{i\omega}$.

5.4 $k \cdot p$ Hamiltonian: First Order Approximation

For studying the behavior of the bands near the degeneracy point we can construct a Hamiltonian that depends on the crystal momentum and make a Taylor expansion near that point. We will make that expansion in terms of $\delta\boldsymbol{k}$, a small displacement from the degeneracy point, $\Gamma = (0,0,0)$. Since $\delta\boldsymbol{k} = (\delta k_x, \delta k_y, \delta k_z)$ is a vector, it transforms under the T representation, $T(\delta k_x, \delta k_y, \delta k_z)$. Comparing with equation (5.14), we see the relation $Q_i \to \delta k_i$, so the most general Hamiltonian at first order in momentum in the vicinity of Γ is:

$$H(\delta\boldsymbol{k}) = \alpha^{\boldsymbol{k}} \begin{pmatrix} 0 & \delta k_z e^{-i\theta} & \delta k_y e^{i\theta} \\ \delta k_z e^{i\theta} & 0 & \delta k_x e^{-i\theta} \\ \delta k_y e^{-i\theta} & \delta k_x e^{i\theta} & 0 \end{pmatrix}, \tag{5.15}$$

where the precise value of the coupling constants $(\alpha^{\mathbf{k}}, \theta)$ is to be determined for each specific case. In general, what we will obtain is the most general form of the Hamiltonians; Group Theory does not give any information on what their precise values can be[3]. They have to be obtained experimentally or using some approximation (DFT, Tight Binding...). The coefficient in the front, $\alpha^{\mathbf{k}}$, can be thought of as the Fermi velocity, in analogy to Dirac semimetals (graphene, for instance).The other coefficient, the phase θ, is of great importance, since it controls the relative slope of the bands at first order near the degeneracy point. If our system is TRS invariant, this adds an extra restriction on w. Since TR operator complex conjugates, it leaves the $(\lambda^6, \lambda^4, \lambda^1)$ matrices invariant, while changes the sign of $(\lambda^7, -\lambda^5, \lambda^2)$. Since the momentum $\boldsymbol{k}$ also changes sign, if the system is TR symmetric there cannot be a coupling with $(\lambda^6, \lambda^4, \lambda^1)$ at first order in $\boldsymbol{k}$, which forces $w = \pi/2$. This is equivalent to saying that the momentum $\mathbf{k}$ will only couple to matrices of $\mathbf{L}$, without coupling to $\tilde{\mathbf{L}}$. Thus, we will have a Hamiltonian of the form $\mathbf{S} \cdot \mathbf{k}$, with $\mathbf{S}$ the spin-1 matrices. In this case, which we will later dub flat or isotropic, the model is symmetric not only under Point Group 23 but under the full SO(3) group.

5.5 Hall viscosity with cubic symmetry

Let us examine the symmetry properties of the Hall viscosity tensor in systems with tetrahedral symmetry. The symmetry analysis in this section holds for both the MHV and PHV, although the interpretation of the resulting stress differs. We define the Hall viscosity tensor as the antisymmetric (and therefore nondissipative) component of the viscosity tensor $\eta^{i\ k}_{\ j\ \ell}$, [169, 176, 184, 194, 217]

$$(\eta_H)^{i\ k}_{\ j\ \ell} \equiv \frac{1}{2}\left(\eta^{i\ k}_{\ j\ \ell} - \eta^{k\ i}_{\ \ell\ j}\right). \tag{5.16}$$

where i, j, k, ℓ index the three spatial directions. The Hall viscosity is odd under TRS [218], and for a fluid with a nonuniform velocity field v^ℓ, leads to a viscous stress[4]

$$\delta\tau^i_j = -(\eta_H)^{i\ k}_{\ j\ \ell}\partial_k v^\ell \tag{5.17}$$

[3]As it is often said in the field, the only exact result Group Theory outputs is 0 (symmetry forbiden).

[4]We use the notation τ for the stress tensor and T for the integrated stress tensor $T_{\mu\nu} = \int \tau_{\mu\nu} d^3x$

Our goal is to identify the independent symmetry-allowed Hall viscosity coefficients. Since these coefficients are scalars, we can determine them by using the invariant tensors of Point Group 23 defined in the previous section. With them, we can identify two viscosity coefficients compatible with tetrahedral symmetry:

$$\begin{aligned}(\eta_H)^{i\ k}_{\ j\ \ell} &= -\eta_1 \epsilon_{ab} \Theta^{ai}{}_j \Theta^{bk}{}_\ell + \frac{\eta_2}{\sqrt{3}} (\Lambda^{mi}{}_j \epsilon_m{}^k{}_\ell - \Lambda^{mk}{}_\ell \epsilon_m{}^i{}_j) \\ &= \eta_1 (\lambda_3 \wedge \lambda_8)^{i\ k}_{\ j\ \ell} + \frac{i\eta_2}{\sqrt{3}} (\lambda_1 \wedge \lambda_2 + \lambda_6 \wedge \lambda_7 - \lambda_4 \wedge \lambda_5))^{i\ k}_{\ j\ \ell},\end{aligned} \tag{5.18}$$

where ϵ_{ab} is the two-dimensional Levi-Civita symbol. In the second line we have reexpressed the antisymmetric product of irreducible tensors in terms of the Gell-Mann matrices λ. This shows that the η_2 term is the antisymmetric dot product of matrices transforming in two 3-dimensional T (vector) irreps,

$$\begin{aligned}\boldsymbol{L} &\equiv T(\lambda_7, -\lambda_5, \lambda_2) \\ \tilde{\boldsymbol{L}} &\equiv T(\lambda_6, \lambda_4, \lambda_1).\end{aligned} \tag{5.19}$$

each spanned by a triplet of Gell-Mann matrices.

Crucially, neither of $\eta_{1,2}$ require a preferred spatial direction. This contrasts with the familiar "quasi-2D" Hall viscosities which are proportional to a pseudovector (i. e. a magnetic field). Thus, η_1 and η_2 are new, essentially 3D Hall viscosities, which can be nonzero in systems with broken rotational symmetry. By contrast, octahedral symmetry requires $\eta_1 = \eta_2 = 0$, as the two tensors in Eq. (5.18) do not transform in the trivial representation of the group 432 (O). Furthermore, η_1 and η_2 can be nonzero in centrosymmetric point groups such as T_h ($m\bar{3}$).

Next, we compute the viscous force density that is produced by these Hall viscosities, noting a difference in interpretation for forces due to MHV and PHV[5],

$$f^\eta_j = -\partial_i \delta\tau^i{}_j = (\eta_H)^{i\ k}_{\ j\ \ell} \partial_i \partial_k v^\ell, \tag{5.20}$$

where $\boldsymbol{f}^\eta$ is the force density and $\delta\tau^i{}_j$ is the viscous stress tensor. We find that η_1 and η_2 contribute additively to $\boldsymbol{f}^\eta$:

$$f^\eta_j = \frac{\eta_1 + \eta_2}{\sqrt{3}} \Lambda^{mik} \partial_i \partial_k \left(\epsilon_{mj\ell} v^\ell \right). \tag{5.21}$$

We see that the fully symmetric tensor Λ, which is only invariant in systems with tetrahedral symmetry, plays a key role in generating the nondissipative forces. Contrast this with quasi-2D Hall viscous forces, which take the form

$$f^{\eta,2D}_j = \eta_{2D} B^m \nabla^2 (\epsilon_{mj\ell} v^\ell), \tag{5.22}$$

[5]Both the MHV and PHV will give rise to viscous forces dictated by Eq. (5.20), the force density MHV should be thought of as a rate of change of momentum density while the PHV force density is a term in the phonon equation of motion.

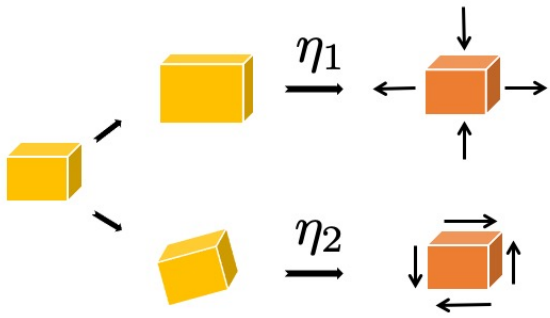

Figure 5.1: Schematic of η_1 and η_2. Dynamic strains (yellow) and viscosity give rise to stresses (orange). In response to a dynamic strain that elongates the length and width of a cubic parcel of fluid while compressing the depth, η_1 produces a diagonal shear stress. In response to a dynamic rotation of the parcel, η_2 produces an off-diagonal shear stress.

and require a symmetry-breaking pseudovector $\mathbf{B}$.

Finally, since only the sum $\eta_1 + \eta_2$ appears in the viscous forces, there must exist a divergenceless contact term which shifts between η_1 and η_2 in the bulk. This term is

$$\delta\tau^i_{\ j} = C_0 \epsilon^{mik} \Lambda_{mj\ell} \partial_k v^\ell, \tag{5.23}$$

which shifts

$$\eta_1 \to \eta_1 + \frac{\sqrt{3}C_0}{2} \tag{5.24}$$

$$\eta_2 \to \eta_2 - \frac{\sqrt{3}C_0}{2}, \tag{5.25}$$

analogous to the bulk redundancy between Hall viscosity and odd pressure in two-dimensional systems [176, 219]. We show the effects of $\eta_{1,2}$ in Fig. 5.1.

5.6 Tight Binding model

Let us now consider a model for a cubic chiral magnetic system, and compute $\eta_{1,2}$ for both the MHV and PHV, as a proof-of-principle [6]. Our tight-binding Hamiltonian is

[6]Note that this noninteracting model is not in the hydrodynamic regime

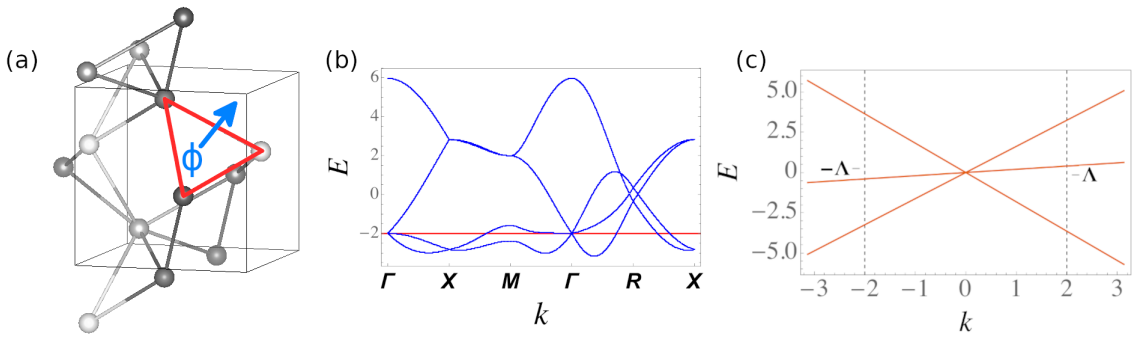

Figure 5.2: (a) Lattice model for SG $P2_13$ (198). In red, neraest neighbors hopping. In blue, complex phase ϕ, which is responsible for TRS breaking. The arrow shows the effective magnetic field the phase creates. (b) Tight Binding model band spectrum. We set the chemical potential to cut through the threefold at Γ. (c) Continuum dispersion of the threefold fermion close to the Γ point. Λ denotes the momentum cut-off.

$$H = \sum_{nm,\mathbf{r},\mathbf{r}'} c^{\dagger}_{n\mathbf{r}'} t^{\mathbf{r},\mathbf{r}'}_{nm} c_{m\mathbf{r}}, \tag{5.26}$$

consisting of s-type orbitals at the 4a Wyckoff position of SG $P2_13$ (No. 198), as shown in Fig. 5.2 (a):

$$\begin{aligned} q_0 &= (x, x, x) \\ q_1 &= (1/2 + x, 1/2 - x, -x) \\ q_2 &= (-x, 1/2 + x, 1/2 - x) \\ q_3 &= (1/2 - x, -x, 1/2 + x). \end{aligned} \tag{5.27}$$

For simplicity, we take $x = 0$ in this work. However, we must take care that simply setting $x = 0$ for this choice of orbitals leads to a lattice with the symmetries of space group $Fm\bar{3}m$ (225) rather than $P2_13$ (No. 198.9). To avoid this, we will determine the nearest neighbor hoppings with generic x, and then take the limit $x \to 0$. Considering hopping processes for nearest neighbor sites, the Hamiltonian

matrix reads [202, 204, 205]:

$$H = 2t \begin{pmatrix} 0 & e^{\frac{-ik_y a}{2}} \cos\left(\frac{k_x a}{2} + \phi\right) & e^{\frac{-ik_z a}{2}} \cos\left(\frac{k_y a}{2} + \phi\right) & e^{\frac{-ik_x a}{2}} \cos\left(\frac{k_z a}{2} + \phi\right) \\ e^{\frac{ik_y a}{2}} \cos\left(\frac{k_x a}{2} + \phi\right) & 0 & e^{\frac{-ik_x a}{2}} \cos\left(\frac{k_z a}{2} - \phi\right) & e^{\frac{ik_z a}{2}} \cos\left(\frac{k_y a}{2} - \phi\right) \\ e^{\frac{ik_z a}{2}} \cos\left(\frac{k_y a}{2} + \phi\right) & e^{\frac{ik_x a}{2}} \cos\left(\frac{k_z a}{2} - \phi\right) & 0 & e^{\frac{-ik_y a}{2}} \cos\left(\frac{k_x a}{2} - \phi\right) \\ e^{\frac{ik_x a}{2}} \cos\left(\frac{k_z a}{2} + \phi\right) & e^{\frac{-ik_z a}{2}} \cos\left(\frac{k_y a}{2} - \phi\right) & e^{\frac{ik_y a}{2}} \cos\left(\frac{k_x a}{2} - \phi\right) & 0 \end{pmatrix}, \tag{5.28}$$

where t is the overlap integral parameterizing hopping from neighbor to neighbor. The phase ϕ represents a time-reversal symmetry breaking magnetic flux, introduced via a Peierls substitution (see Fig. 5.2 (a)). In Fig. 5.2 (b), we can see the band dispersion for the system with $t = 1$ and $\phi = 0.1$.

5.6.1 Symmetry

This Hamiltonian satisfies the symmetry constraints of the MSG $P2_13$ (No. 198.9), with:

$$\rho\left(\{C_{3_1}^{-}|000\}\right) = \begin{pmatrix} 1 & 0 & 0 & 0 \\ 0 & 0 & 1 & 0 \\ 0 & 0 & 0 & 1 \\ 0 & 1 & 0 & 0 \end{pmatrix}, \tag{5.29}$$

$$\rho\left(\{C_{2x}|\tfrac{1}{2}\tfrac{1}{2}0\}\right) = \begin{pmatrix} 0 & 1 & 0 & 0 \\ 1 & 0 & 0 & 0 \\ 0 & 0 & 0 & 1 \\ 0 & 0 & 1 & 0 \end{pmatrix} e^{-\frac{1}{2}i(k_x - ky)}, \tag{5.30}$$

$$\rho\left(\{C_{2y}|0\tfrac{1}{2}\tfrac{1}{2}\}\right) = \begin{pmatrix} 0 & 0 & 1 & 0 \\ 0 & 0 & 0 & 1 \\ 1 & 0 & 0 & 0 \\ 0 & 1 & 0 & 0 \end{pmatrix} e^{-\frac{1}{2}i(k_y - k_z)}, \tag{5.31}$$

so that

$$\rho(g)^{\dagger} H(\mathbf{k}, \mathbf{Q}) \rho(g) = H(g\mathbf{k}, g\mathbf{Q}), \tag{5.32}$$

where $\mathbf{k}$ is crystal momentum and $\mathbf{Q}$ is any external field. When exactly at the Γ point, $\Gamma = (0, 0, 0)$, bands with different eigenvalues decouple, so we can rewrite the Hamiltonian into the basis of symmetry adapted coordinates at Γ. These are the coordinates that block diagonalize the symmetry operators in Eq. (5.29). The change of basis matrix is:

$$U = \frac{1}{2}\begin{pmatrix} 1 & 1 & 1 & 1 \\ 1 & 1 & -1 & -1 \\ 1 & -1 & 1 & -1 \\ 1 & -1 & -1 & 1 \end{pmatrix}. \tag{5.33}$$

5.6.2 Threefold at the Γ point: energies and states

We can expand the Hamiltonian Eq. (5.28) around the $\Gamma = (0,0,0)$ point, and apply the unitary transformation Eq. (5.33) to obtain the low-energy model

$$\begin{aligned} H &= \sum_{nm\mathbf{k}} c^\dagger_{n\mathbf{k}} f(\mathbf{k}) c_{m\mathbf{k}}, \\ f(\mathbf{k}) &= \left(\begin{array}{c|c} 6t\cos(\phi) & iv_F e^{i\phi}\mathbf{k}^T \\ \hline -iv_F e^{-i\phi}\mathbf{k} & h \end{array}\right) \end{aligned} \tag{5.34}$$

where the Fermi velocity is $v_F = ta$, with t the Tight Binding hopping parameter and a the lattice constant. The lower-right block corresponds to the 'spin-1' bands (threefold fermion) with

$$h = v_F\left(\cos(\phi)\,\mathbf{k}\cdot\mathbf{L} + \sin(\phi)\,\mathbf{k}\cdot\tilde{\mathbf{L}}\right) - 2t\cos(\phi)\lambda_0. \tag{5.35}$$

If we take $\theta = \phi + \frac{\pi}{2}$, the energies for general ϕ are given by [204]

$$E_n = \frac{2|\mathbf{k}|}{\sqrt{3}}\cos\left(\frac{1}{3}\arccos\left(\frac{3\sqrt{3}k_xk_yk_z}{|\mathbf{k}|^3}\cos(3\theta)\right) - \frac{2\pi(n-1)}{3}\right). \tag{5.36}$$

Above $n \in \{1,2,3\}$ indexes the three states [7], for small ϕ, the threefold dispersion takes a form that matches Fig. 5.2 (c),

$$\begin{aligned} E_1 &= |\mathbf{k}| + 3\phi\frac{k_xk_yk_z}{|\mathbf{k}|^2} + \mathcal{O}(\phi^2) \\ E_2 &= -6\phi\frac{k_xk_yk_z}{k^2} + \mathcal{O}(\phi^2) \\ E_3 &= -|\mathbf{k}| + 3\phi\frac{k_xk_yk_z}{|\mathbf{k}|^2} + \mathcal{O}(\phi^2) \end{aligned} \tag{5.37}$$

which have normalized eigenfunctions given by

$$\psi_n = \frac{1}{\sqrt{(3E_n^2 - |\mathbf{k}|^2)(E_n^2 - k_z^2)}}\begin{pmatrix} E_n^2 - k_z^2 \\ E_nk_xe^{-i\theta} + k_yk_ze^{2i\theta} \\ E_nk_ye^{i\theta} + k_xk_ze^{-2i\theta} \end{pmatrix}. \tag{5.38}$$

[7] We neglect the constant shift given by the λ_0 term

Now that we have the effective model of the threefold near the Γ point, we can analyze its symmetries. Dropping the constant term in Eq. 5.35 and making $v_F = 1$, we have that the effective Hamiltonian takes the form:

$$H_\Gamma = \cos\phi \mathbf{k}\cdot\mathbf{L} + \sin\phi \mathbf{k}\cdot\tilde{\mathbf{L}}. \tag{5.39}$$

The contribution $\mathbf{L}\cdot\mathbf{k}$, with $\mathbf{k} = (k_x, k_y, k_z)$, has full $SO(3)$ invariance, while $\tilde{\mathbf{L}}\cdot\mathbf{k}$ is invariant only under point group 23. We understand this as follows: the Gell-Mann matrices in Eq. (5.7) belong to $T\otimes T$, which can be obtained via subduction from the $(l=1)\otimes(l=1)$ representation of $SO(3)$. Denoting the irreps of $SO(3)$ by their dimension $2l+1$, the rules of angular momentum composition give $3\otimes 3 \to 1$ (scalar) + 3 (antisymmetric rank 2 tensors) + 5 (traceless symmetric rank two tensors). Now, $\mathbf{L} = (\lambda_7, -\lambda_5, \lambda_2)$ are antisymmetric and belong to 3, the vector representation of $SO(3)$. On the other hand, $\tilde{\mathbf{L}} = (\lambda_6, \lambda_4, \lambda_2)$ are symmetric and together with the two traceless symmetric matrices (λ_3, λ_8) form a basis for the irrep 5 ($l = 2$) of SO(3). Thus $\tilde{\mathbf{L}}$ can not be promoted to a vector of $SO(3)$ and, as a consequence, $\tilde{\mathbf{L}}\cdot\mathbf{k}$ can not be invariant under $SO(3)$. Instead we have the subduction rule 5 $(\lambda_6, \lambda_4, \lambda_2, \lambda_3, \lambda_8) \to T(\lambda_6, \lambda_4, \lambda_2) + {}^1E^2E(\lambda_8, \lambda_3)$. Thus, we see directly why $\phi \neq 0$ implies a breaking of continuous rotational symmetry.

From Eq. (5.34), we see that when ϕ is small there is a gap of order t separating the spin-0 and spin-1 fermions at Γ. Thus for small ϕ and $\mathbf{k}$, transitions from the threefold to onefold degeneracies mediated by the off-diagonal elements of $f(\mathbf{k})$ are parametrically small, and we can restrict our attention to the spin-1 fermion. Furthermore, in the continuum limit $a \to 0$ with $v_F = ta$ fixed, we see that the gap becomes infinitely large. With this in mind, we focus specifically on the threefold fermion.

5.7 Stress Response

In this section we will analytically compute the stress tensor derived from both phonon and continuity methods. To compute the MHV and PHV, we employ the stress-stress form of the Kubo formula [175] (in the limit $\omega^+ \to 0$)

$$(\eta^{\mathrm{H}})^{\mu\ \lambda}_{\ \nu\ \rho} = \frac{1}{2\omega^+ V}\int_0^\infty dt e^{i\omega^+ t}\left(\langle[T^\mu_\nu(t), T^\lambda_\rho(0)] - [T^\lambda_\rho(t), T^\mu_\nu(0)]\rangle\right). \tag{5.40}$$

To do so we first must define a stress tensor

$$T_{\mu\nu} = \sum_{nm\mathbf{k}} c^\dagger_{n\mathbf{k}} T_{\mu\nu}(\mathbf{k}) c_{m\mathbf{k}}, \tag{5.41}$$

corresponding to Eq. (5.26). For the PHV, we define the stress by considering an electron-phonon coupling ansatz [185,187,220] and perturbing the background lattice, yielding the *phonon* stress tensor. The phonon stress results from microscopically perturbing the lattice via phonons, relating to atomic displacements. For the MHV, we perturb the electronic degrees of freedom directly via coupling to background geometry [175, 176], yielding the *continuity* stress tensor. This is a coarse-grained stress tensor that directly corresponds to momentum transport in the long-wavelength limit, and can be identified with the stress tensor of fluid dynamics.

5.7.1 Phonon Stress Tensor

In the phonon method, strain is introduced into the model through small displacements of the orbital positions, modifying the hopping parameters $t_{nm}^{\mathbf{r},\mathbf{r}'}$ as

$$t^{\mathbf{r},\mathbf{r}'} \to e^{-(\delta\mathbf{r})} t^{\mathbf{r},\mathbf{r}'} + O(\delta\mathbf{r}^2). \tag{5.42}$$

Above, $\delta\mathbf{r}$ is the change in distance between orbitals given by the applied (unsymmetrized) strain as $u_{\mu\nu} = \partial_\mu \delta r_\nu$ [8]. Applying this prescription to Eq. (5.26) we define the phonon stress tensor as

$$T^{(p)}_{\mu\nu} = \frac{\delta H(u_{\mu\nu})}{\delta u_{\mu\nu}} \tag{5.43}$$

Given the structure of the viscosity tensor Eq. (5.18) and the fact that antisymmetric strains enter only at higher orders in $\delta\mathbf{r}$ in Eq. (5.42), it suffices to consider "diagonal" strains (i.e. u_{xx}, u_{yy} and u_{zz}) [9]. Following Eq. (5.42) and Eq. (5.43), we get the following changes to the hopping parameters in terms of strain:

$$\begin{aligned} t_{01}, t_{23} &\to t + (u_{xx} + u_{yy})t \\ t_{02}, t_{13} &\to t + (u_{yy} + u_{zz})t \\ t_{03}, t_{12} &\to t + (u_{zz} + u_{xx})t \end{aligned} \tag{5.44}$$

Plugging this into the tight binding model of Eq. (5.28), we have that the strained Hamiltonian takes the following form:

[8] Note that we do *not* symmetrize the strain tensor, and though this object is sometimes called the distortion tensor, we choose this convention to be consistent with [175,176]

[9] off-diagonal yet symmetric strains do not contribute to η_1

$$H = 2t \begin{pmatrix} 0 & f_{ab}e^{\frac{-ik_y a}{2}}\cos\left(\frac{k_x a}{2}+\phi\right) & f_{bc}e^{\frac{-ik_z a}{2}}\cos\left(\frac{k_y a}{2}+\phi\right) & f_{ac}e^{\frac{-ik_x a}{2}}\cos\left(\frac{k_z a}{2}+\phi\right) \\ f_{ab}e^{\frac{ik_y a}{2}}\cos\left(\frac{k_x a}{2}+\phi\right) & 0 & f_{ac}e^{\frac{-ik_x a}{2}}\cos\left(\frac{k_z a}{2}-\phi\right) & f_{bc}e^{\frac{ik_z a}{2}}\cos\left(\frac{k_y a}{2}-\phi\right) \\ f_{bc}e^{\frac{ik_z a}{2}}\cos\left(\frac{k_y a}{2}+\phi\right) & f_{ac}e^{\frac{ik_x a}{2}}\cos\left(\frac{k_z a}{2}-\phi\right) & 0 & f_{ab}e^{\frac{-ik_y a}{2}}\cos\left(\frac{k_x a}{2}-\phi\right) \\ f_{ac}e^{\frac{ik_x a}{2}}\cos\left(\frac{k_z a}{2}+\phi\right) & f_{bc}e^{\frac{-ik_z a}{2}}\cos\left(\frac{k_y a}{2}-\phi\right) & f_{ab}e^{\frac{ik_y a}{2}}\cos\left(\frac{k_x a}{2}-\phi\right) & 0 \end{pmatrix}, \tag{5.45}$$

with $f_{ab} = 1+a+b$ and $(a,b,c) \equiv (u_{xx}, u_{yy}, u_{zz})$. We now transform tha Hamiltonian into the symmetry adapted coordinate basis using Eq. (5.33) and expand to first order in the product of strain and momentum. The resulting perturbed Hamiltonian is:

$$t \begin{pmatrix} 0 & -k_x(a+b)s_\phi + ik_x(a+c)c_\phi & -k_y(b+c)s_\phi + ik_y(a+b)c_\phi & -k_z(a+c)s_\phi + ik_z(b+c)c_\phi \\ -k_x(a+b)s_\phi - ik_x(a+c)c_\phi & 0 & k_z(a+c)s_\phi - ik_z(b+c)c_\phi & k_y(b+c)s_\phi + ik_y(a+b)c_\phi \\ -k_y(b+c)s_\phi - ik_y(a+b)c_\phi & k_z(a+c)s_\phi + ik_z(b+c)c_\phi & 0 & k_x(a+b)s_\phi - ik_x(a+c)c_\phi \\ -k_z(a+c)s_\phi - ik_z(b+c)c_\phi & k_y(b+c)s_\phi - ik_y(a+b)c_\phi & k_x(a+b)s_\phi + ik_x(a+c)c_\phi & 0 \end{pmatrix}, \tag{5.46}$$

with $(s_\phi, c_\phi) \equiv (\sin(\phi), \cos(\phi))$ and $(a,b,c) \equiv (u_{xx}, u_{yy}, u_{zz})$. When taking into account lab frame effects[10] [221], we get an extra term in the first row (column) of the Hamiltonian that can be expressed as a vector $\delta H = 2ic_\phi\,(0, ck_z, ak_x, bk_y)$ ($\delta H = -2ic_\phi\,(0, ck_z, ak_x, bk_y)^T$). There is no contribution to the bottom 3x3 block at this order, so the viscosity tensor for the threefold fermion remains unchanged.

When coupling to antisymmetric strain, the distances between orbitals do not change at first order in strain, so the contribution to the stress tensor is zero within our series expansion. There is a coupling, however, when considering lab-frame effects. Just as above, there is no contribution to the 3x3 or 1x1 blocks describing the low energy physics of the system, but there is a contribution to the row connecting them. In this case, this contribution reads $\delta H = 2ic_\phi\,(0, u_{13}k_x + u_{23}k_y, -u_{12}k_y - u_{13}k_z, u_{12}k_x - u_{23}k_z)$. Thus there is no coupling of the spin-1 fermion to anti-symmetric strain in the phonon method. This translates in η_2 being zero at this order of approximation.

We can now compute explicitly the phonon stress tensor as defined in 5.43. The

[10] When introducing strain into the Hamiltonian as a displacement of the lattice, there are two places in which it enters; first, the one we already described, as a change in the hopping parameter sue to the distance change. Second, in the Bloch phases $\exp(i\mathbf{k}\cdot\mathbf{q}_i)$, which depending on the frame (lab vs crystal) would get an extra term in the exponent due to the strain of the atomic positions $\mathbf{q}_i \to (1+u_{ij})\mathbf{q}_j$

diagonal phonon stress tensor restricted to the spin-1 fermions is

$$\begin{aligned} T^{(p)}_{xx}(\mathbf{k}) &= v_F \cos(\phi)\,(k_x L_x + k_y L_y) \\ &\quad + v_F \sin(\phi)\left(k_x \tilde{L}_x + k_z \tilde{L}_z\right) \qquad (5.47) \\ T^{(p)}_{yy}(\mathbf{k}) &= v_F \cos(\phi)\,(k_y L_y + k_z L_z) \\ &\quad + v_F \sin(\phi)\left(k_x \tilde{L}_x + k_y \tilde{L}_y\right). \qquad (5.48) \end{aligned}$$

$T^{(p)}_{\mu\nu}$ transforms as a tensor in the point group 23, which is the point group describing both the underlying lattice and the Γ point. Note that even when $\phi = 0$, although the Hamiltonian h is invariant under $SO(3)$, $T^{(p)}_{\mu\nu}$ is covariant only under the discrete group 23. This comes from the fact that the phonon stress is sensitive to the actual position of orbitals in the unit cell. As we will see afterwards, this is not the case for the continuity method, which is isotropic for $\phi = 0$.

5.7.2 Momentum Continuity Stress Tensor

In this section we describe the *continuity* method (corresponding to the "momentum" Hall viscosity), which is the approach to long-wavelength momentum transport and stress response for lattice systems recently formulated in Ref. [176] for two dimensional systems. First we describe the generalization of the approach in Ref. [176] to three dimensions, focusing specifically on cubic lattices. Next, we present the long-wavelength lattice stress tensor for the full four band tight binding model, which simplifies to $T^{(c)}_{\mu\nu}$ when considering the threefold fermion at the Γ point.

In this approach, the stress tensor is identified through a long-wavelength analog of a continuity equation for momentum density. In the continuum, the momentum continuity equation describes a relationship between momentum density and stress:

$$\partial_t g_\nu(\mathbf{r}) + \partial_\mu \tau_{\mu\nu}(\mathbf{r}) = f^{\text{ext}}_\mu(\mathbf{r}). \qquad (5.49)$$

Above $\mathbf{f}^{\text{ext}}$ is the density of external forces acting on the continuum system. In a system with Hamiltonian H, internal angular momentum generator L_{int}, and $\mathbf{f}^{\text{ext}} = 0$, we can write the integrated stress tensor $T_{\mu\nu} = \int d^3 r \tau_{\mu\nu}(\mathbf{r})$ in terms of strain generators $\mathcal{J}_{\mu\nu}$ as [175, 222]

$$T_{\mu\nu} = -i[H, \mathcal{J}_{\mu\nu}]. \qquad (5.50)$$

The strain generators are made up of two terms, the first below accounting for spatial deformations (which we call the "kinetic" part) and the second due to rotations of internal angular degrees of freedom:

$$\mathcal{J}_{\mu\nu} = -\frac{1}{2}\{x_\mu, p_\nu\} - \frac{1}{2}\epsilon_{\mu\nu\rho} L^\rho_{\text{int}}. \qquad (5.51)$$

On the lattice, with discrete rather than continuous translation invariance, we no longer have the continuity equation Eq. (5.49), and our notion of momentum transport outlined above must be modified.

We start by considering the lattice momentum density operator $\mathbf{g}_\mu^L$, which can be decomposed into a kinetic part and a contribution due to internal angular momentum L_{int}. The kinetic piece can be written

$$g_\mu^{\text{kin}}(\mathbf{R}) = \frac{i}{4|\mathbf{a}_\mu|}\sum_n \left(c^\dagger_{n\mathbf{R}+\mathbf{a}_\mu} c_{n\mathbf{R}} - c^\dagger_{n\mathbf{R}-\mathbf{a}_\mu} c_{n\mathbf{R}} + c^\dagger_{n\mathbf{R}} c_{n\mathbf{R}-\mathbf{a}_\mu} - c^\dagger_{n\mathbf{R}} c_{n\mathbf{R}+\mathbf{a}_\mu} \right), \quad (5.52)$$

We note the Bravais lattice vectors for this cubic lattice can be written $\mathbf{a}_\mu = a\mathbf{e}_\mu$, where $\mathbf{e}_\mu$ denote Cartesian basis vectors. The internal angular momentum contribution is given by [176, 222]

$$g_\mu^{\text{int}}(\mathbf{R}) = \sum_{nm\nu} \frac{1}{4|\mathbf{a}_\nu|}\epsilon_{\mu\nu\rho}(L_{\text{int}})^{nm}_\rho \left(c^\dagger_{n\mathbf{R}+\mathbf{a}_\nu} c_{m\mathbf{R}} - c^\dagger_{n\mathbf{R}-\mathbf{a}_\nu} c_{m\mathbf{R}} + c^\dagger_{n\mathbf{R}} c_{m\mathbf{R}+\mathbf{a}_\nu} - c^\dagger_{n\mathbf{R}} c_{m\mathbf{R}-\mathbf{a}_\nu} \right). \quad (5.53)$$

If we write the total lattice momentum density $g^L(\mathbf{R}) \equiv g^{\text{kin}}(\mathbf{R}) + g^{\text{int}}(\mathbf{R})$ in momentum space with coordinate $\mathbf{q}$, we can expand in powers of $\mathbf{q}$ in the long-wavelength limit $\mathbf{q} \to 0$, finding

$$g_\mu^{\text{L}}(\mathbf{q}) = P_\mu + i\sum_\nu q_\nu J_{\text{L},\nu\mu} + \mathcal{O}(\mathbf{q}^2). \quad (5.54)$$

We see that the momentum density in orders is given by the zeroth order contribution – the total momentum P_μ (which is identically $g_\mu^L(\mathbf{0})$) – and the first order contribution which is expressed in terms of the lattice strain generators, which generalize the continuum strain generators found in Ref. [175],

$$\mathcal{J}_{\text{L},\mu\nu} \equiv -\frac{i}{2}\sum_{\mathbf{k}nm} c^\dagger_{n\mathbf{k}} \left[\left\{ \frac{\sin \mathbf{k}\cdot\mathbf{a}_\nu}{|\mathbf{a}_\nu|}, \frac{\partial}{\partial k_\mu} \right\} \delta^{nm} + i\sum_\rho \epsilon_{\mu\nu\rho} \cos \mathbf{k}\cdot\mathbf{a}_\mu (L_{\text{int}})^{nm}_\rho \right] c_{m\mathbf{k}}. \quad (5.55)$$

The long-wavelength lattice stress can now be calculated from the strain generators Eq. (5.55) in the same way as in the continuum:

$$T_{\text{L},\mu\nu} = -i[H, \mathcal{J}_{\text{L},\mu\nu}]. \quad (5.56)$$

The continuity stress $T^{(c)}_{\mu\nu}$ is defined via a lattice analog of the momentum continuity equation (See SM) [176], resulting in:

$$T^{(\mathrm{c})}_{\mu\nu}(\mathbf{k}) = \left(k_\nu \partial_\mu f(\mathbf{k}) + \frac{i}{2}\epsilon_{\mu\nu\rho}\big[f(\mathbf{k}), L^{\mathrm{int}}_\rho\big] \right). \tag{5.57}$$

$T^{(\mathrm{c})}_{\mu\nu}$ contains contributions from "kinetic" strains (spatial deformations) and from "spin" strains due to the internal angular momentum $\mathbf{L}_{int}$. The continuity stress generalizes the Belinfante (improved) stress tesnor [176, 222, 223]

In our model, we have $\mathbf{L}^{\Gamma}_{int} = 0 \oplus \mathbf{L}$ describing the spin-0 and spin-1 fermions. Using this, we can compute the stress tensor near the Γ point restricted to the spin-1 fermion to find:

$$\begin{aligned} T^{(\mathrm{c})}_{\mu\nu} &= \frac{v_F \cos(\phi)}{2} \left(k_\mu L_\nu + k_\nu L_\mu \right) \\ &\quad + \frac{v_F \sin(\phi)}{2} \left(3k_\nu \tilde{L}_\mu - k_\mu \tilde{L}_\nu + \sum_{a\rho\lambda} \epsilon_{\mu\nu\rho} \Theta^a_{\rho\lambda} k_\lambda \epsilon^{ab} v_b \right), \end{aligned} \tag{5.58}$$

where $a, b = 1, 2$ as in Eq. (5.3).

Note that $T^{(\mathrm{c})}_{\mu\nu} \neq T^{(p)}_{\mu\nu}$. In the continuity approach, antisymmetric stress (caused by anisotropy) enters at order ϕ and $T^{(\mathrm{c})}_{\mu\nu}$ matches the symmetries of the Bloch hamiltonian at the Γ point (when $\phi = 0$ the continuity stress is $SO(3)$-covariant). By contrast, when $\phi = 0$ the phonon stress is anisotropic. The distinction between the two stress tensors stems from their different physical interpretations: the phonon stress is sensitive to the nonzero orbital positions of the $4a$ Wyckoff position, which results in anisotropy in $T^{(p)}_{\mu\nu}$ when $\phi = 0$. Contrarily, the continuity stress averages over intra-unit cell momentum transport, and so is sensitive only to the symmetries of the effective Hamiltonian. Below, we will compute the PHV with $T^{(p)}_{\mu\nu}$, and the MHV with $T^{(\mathrm{c})}_{\mu\nu}$.

5.8 Hall Viscosity

Next we compute the Hall viscosity coefficients η_1 and η_2 from Eq. (5.18), and the physical response $\eta_{tot} = \eta_1 + \eta_2$, for both the MHV and PHV.

5.8.1 PHV and MHV

Focusing on the spin-1 fermion, we can simplify the Kubo formula Eq. (5.40) in terms of eigenstates $|n\rangle$ of h as

$$\eta^{\mathrm{H}}_{ijkl} = \frac{-1}{4\pi^3} \int d^3k \sum_{n\neq m} \frac{\mathcal{O}_{nm}}{\Delta\epsilon^2_{nm}} \mathrm{Im}\left(\langle n| T_{ij} |m\rangle \langle m| T_{kl} |n\rangle \right), \tag{5.59}$$

where $\Delta\epsilon_{nm} = \epsilon_n - \epsilon_m$, and the relative occupation factor is $\mathcal{O}_{nm} = n(\epsilon_n - \mu, T) - n(\epsilon_m - \mu, T)$ with $n(\epsilon, T) = (1+e^{\epsilon/T})^{-1}$ the Fermi distribution with chemical potential μ and temperature T[11].

For the PHV, the stress tensor Eq. (5.43) is explicitly symmetric under $\mu \leftrightarrow \nu$ and therefore $\eta_2 = \eta_{1221}$ is zero. The total PHV in this case is entirely due to $\eta_1 = \eta_{1122}$, and given by (to first order in ϕ):

$$\eta_{\text{tot}}^{(p)} = \eta_1^{(p)} = \frac{v_F^2}{8\pi^3} \begin{cases} \beta_1 \left(-17\Lambda^3 + 60\mu^3\right) \phi, & \mu > 0 \\ \beta_1 \left(-17\Lambda^3 + 42\mu^3\right) \phi, & \mu < 0, \end{cases} \tag{5.60}$$

where the momentum cut-off Λ in Fig. 5.2 (c) regulates the integral in Eq. (5.59), and $\beta_1 = \frac{4\pi}{2835} \approx 0.00443$.

By contrast, for the MHV, the total viscosity to first order in ϕ is entirely due to η_2. Using the energies and eigenvectors given in Eq. (5.37) and Eq. (5.38), we find that the integrand for η_1 in Eq. (5.59) has an energy denominator that is odd in k_z at order ϕ, which suppresses the zeroth order contribution from the numerator. When the states are taken to zeroth order in ϕ, the numerator is odd in k_x and k_y, and when the states are taken to first order in ϕ the only nonvanishing matrix elements in the numerator are odd in k_z, all of which leads to $\eta_1 = 0$ [12]. The total MHV is

$$\eta_{\text{tot}}^{(c)} = \eta_2^{(c)} = \frac{v_F^2}{8\pi^3} \begin{cases} \beta_2 \left(\Lambda^3 - \mu^3\right) \phi & \mu > 0 \\ -\beta_2 \left(\Lambda^3 + \mu^3\right) \phi & \mu < 0, \end{cases} \tag{5.61}$$

where $\beta_2 = \frac{4}{405}\pi \approx 0.0310$. Around $\mu = 0$, the viscosity is discontinuous. This arises from the fact that, since the antisymmetric part of the coninuity stress is linear in ϕ, we must consider the unperturbed band structure in the energy denominators in Eq. (5.59). When $\phi = 0$, the band structure has a flat band bisecting two linealry dispersing bands. The filling of the flat band when μ passes through zero then causes the discontinuity in η_2, which we can attribute to the contribution of this band to the Hall viscosity. We plot $\eta_{\text{tot}}^{(c,p)}$ in Fig. 5.3.

Similar to the Hall viscosity for Dirac fermions in 2D [176, 185, 224], we see that both $\eta_{\text{tot}}^{(p)}$ and $\eta_{\text{tot}}^{(c)}$ consist of two terms, one of which depends explicitly on the cutoff Λ. We can interpret the cutoff-independent contribution (or, more properly, its derivative with respect to chemical potential) as the Fermi surface contribution to the Hall viscosity, while the cutoff-dependent term parametrizes unknown contributions to the viscosity from occupied states at large momenta.

[11] We introduced temperature to regularize the angular integral, and then took the $T \to 0$ limit

[12] There are no zeroth order contributions to the Hall viscosity as the model gains an effective rotational symmetry as $\phi = 0$

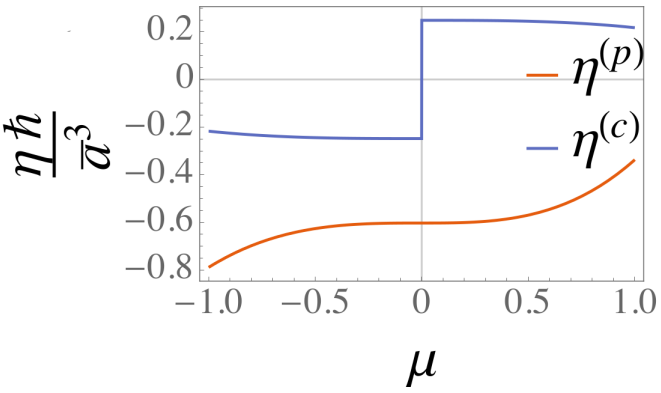

Figure 5.3: Integrated Hall viscosity as a function of chemical potential. Notice there is a jump in the MHV when $\mu = 0$.

5.8.2 Lattice Viscosity

Using the continuity stress tensor, we can go beyond this approximation to compute the MHV for the full tight-binding model numerically. The general form of the lattice stress for three dimensional cubic lattices (where we can write $\mathbf{a}_\mu = a\mathbf{e}_\mu$) is given by

$$\begin{aligned} T_{\mu\nu} &= \sum_{nm\mathbf{k}} c^\dagger_{n\mathbf{k}} \left(\partial^\mu f_{nm}(\mathbf{k}) \frac{\sin(\mathbf{k}\cdot\mathbf{a}_\nu)}{|\mathbf{a}_\nu|} + i \sum_\rho \cos(\mathbf{k}\cdot\mathbf{a}_\mu)\epsilon_{\mu\nu\rho} \left[f(\mathbf{k}), (L_{\text{int}})_\rho \right]_{nm} \right) c_{m\mathbf{k}} \\ &\equiv \sum_{\mathbf{k}} c^\dagger_{\mathbf{k}} T_{\mu\nu}(\mathbf{k}) c_{\mathbf{k}}. \end{aligned} \tag{5.62}$$

We now specify to our tight-binding model in MSG $P2_13$ (No. 198.9). In the symmetry adapted coordinates described by the transformation Eq. (5.33), the internal angular momentum generator takes a block diagonal form with a spin zero and spin one (threefold) contributions

$$\mathbf{L}_{\text{int}} = \mathbf{0} \oplus \mathbf{L}. \tag{5.63}$$

It's also possible to view the internal angular momentum generator in the non-symmetry adapted coordinates (which Eq. (5.28) is written in) where we write the internal angular momentum as $\mathbf{L}'_{\text{int}} = U\mathbf{L}_{\text{int}}U^T$. For our model in Eq. (5.28), the stress is therefore given by

$$T_{\mu\nu}(\mathbf{k}) = T^{\text{kin}}_{\mu\nu}(\mathbf{k}) + T^{\text{spin}}_{\mu\nu}(\mathbf{k}) = \frac{\sin(k_\nu a)}{a} \partial_\mu f(\mathbf{k}) + i\cos(k_\mu a)\epsilon_{\mu\nu\rho}\left[f(\mathbf{k}), L'_\rho \right]. \tag{5.64}$$

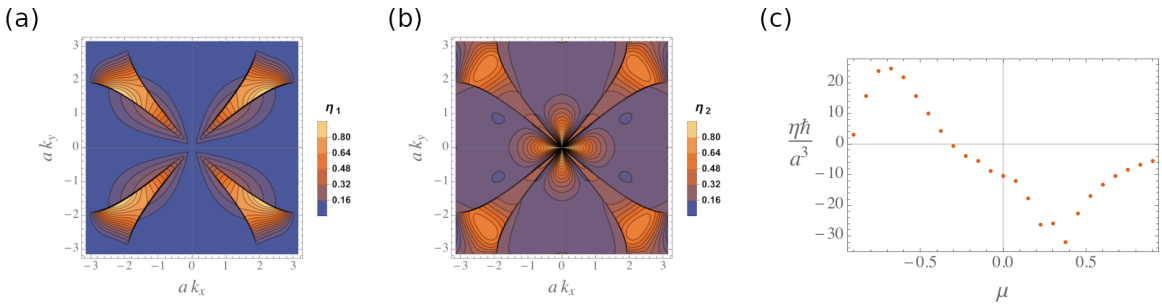

Figure 5.4: (a-b) Momentum cuts ($k_z = 0$) of lattice Hall viscosity density. Notice that it complies with the symmetries of the system. (c) Numeric integration of the lattice Hall viscosity. Notice that there is no jump at $\mu = 0$.

Equipped with a long-wavelength stress tensor we can compute the Hall viscosity on the lattice using the stress-stress Kubo formula from the main text. Unlike in the main derivations of PHV and MHV, where we consider the physics the Γ point at small ϕ and consider only the threefold fermion, we must take into account the full four band model in Eq. (5.28) to compute the viscosity. This can be seen in Fig. (5.2) (b), where at the Γ point the gap between the threefold and the fourth band is not sizable enough to neglect the fourth band.

In contrast to the result for the total viscosity in the main text, we see in Fig. 5.4 (c) that there is no discontinuity across the $\mu = 0$ point. We also plot some cuts of the Hall viscosity density, to see that it is non-zero along whole planes (in particular, $k_z = 0$) and that it complies wuth the symmetries of the system in. We show the results in Figs. 5.4 (a) and (b).

5.9 Conclusions

We have highlighted a manifestly 3D cubic Hall viscosity (MHV and PHV), which appears in systems with tetrahedral symmetry. As a proof-of-concept, we have shown that these viscosities are nonzero for a threefold fermion at the Γ point in MSG $P2_13$ (No 198.9). Using our phonon and continuity methods to examine the stress response in this model, we found that both the MHV and PHV were nonzero in this system. We also emphasize that the MHV and PHV are responses defined for distinct stress tensors. The MHV corresponds to the "continuity" stress that exactly matches the symmetries at the Γ point, while the PHV corresponds to the "phonon" stress which is intimately connected to the elastic response of the underlying lattice model.

Beyond our proof-of-principle calculation, the manifestly 3D nature of the cubic Hall viscosity suggests that viscous transport in three-dimensional magnetic materials

can be phenomenologically different than in two dimensions.

In particular, measuring the local flow profiles [196, 225] or thermoelectric transport coefficients [192] in magnets in the tetrahedral SGs (Nos. 195–206) would reveal the signatures of our 3D viscosity. For example, outside of MSG 198.9, we could consider a 3D cubic magnet with approximate Galilean symmetry at low energies. For such a system the force tensor Eq. (5.20), and therefore the MHV[13], is proportional to the wavevector dependent Hall conductivity [175, 217, 226]

$$\omega^2 \delta\sigma_{ij}^H \propto \eta_{tot}^{(c)} \Lambda^{mk\ell} q_k q_\ell \epsilon_{mij} \equiv \eta_{tot}^{(c)} V_\ell(\mathbf{q}) \epsilon_{\ell ij}, \tag{5.65}$$

where the vector $\mathbf{V}(\mathbf{q})$ highlights the structural parallel with the natural optical activity of a crystal [204].

We can decompose $\mathbf{V}$ into longitudinal and transverse components as $\mathbf{V}_\parallel = \hat{\mathbf{q}}(\hat{\mathbf{q}} \cdot \mathbf{V}) = 6\eta_{tot} q_x q_y q_z / |\mathbf{q}|$ and $\mathbf{V}_\perp = \mathbf{V} - \mathbf{V}_\parallel$. We then see that $\mathbf{V}_\parallel$ gives a $\mathbf{q}$-dependent correction to natural optical activity, while $\mathbf{V}_\perp$ leads to a Hall current proportional to the longitudinal component of the electric field. Note, crucially, that $\mathbf{V}_\parallel$ vanishes for plane waves at normal incidence. Furthermore, in tetrahedral systems without Galilean invariance, this wavevector-dependent contribution to the conductivity need not be zero; the fate of the viscosity-conductivity relation in these systems (generalizing work such as Ref. [227]) is an interesting avenue for further study. Analogous considerations for flow in narrow channels suggest that η_{tot} may play a role in interaction-dominated transport in narrow channels [177, 178]. The physical signatures of PHV proposed in spin-phonon and electron-phonon coupled systems [187, 189–191], such as contributions to thermal Hall conductance and modifications to phononic dispersion, could be probed as well in these systems to measure the cubic PHV. The frequency and disorder [228] dependence of the MHV and PHV could also yield interesting insights. As none of our results are specific to the hydrodynamic regime, we expect disorder that preserves the symmetry on average will not modify our qualitative conclusions.

Chiral magnets such as the family of Mn_3IrSi [215, 216] are promising platforms to study these effects. As shown in Ref [193], this compound has a noncollinear magnetic configuration preserving the size of the unit cell; group theory analysis showed further that the ground state magnetic order preserved all of the unitary symmetry operations consistent with MSG $P2_13$. Another interesting candidate is $MnTe_2$ in MSG $Pa\bar{3}$ (No. 205.33) [65, 229, 230]. It has a reported noncollinear magnetic structure, with the magnetic moments of the four inequivalent manganese ions pointing along the cubic body diagonals. Although naturally a semiconductor, Ag-doping could increase the carrier concentration [231].

[13] The viscosity-conductivity relation [175] applies to the MHV and not the PHV, as it relies on the continuity equation

Chapter 6

Concluding thoughts

In this thesis we study topological physics from the lens of symmetry. First, in Chapter 2, we introduce the formalism of topological quantum chemistry, which relates topological properties of filled bands to their Wannier description. As we show in depth for the particular case of graphene, we can extract the wannierizability of the bands from the symmetry properties of Bloch wavefunctions at high symmetry momenta in the BZ. Following the resulting symmetry analysis, we predict that any ordering of graphene bands is topological, either a topological insulator or a topological semimetal.

Other than predictive power, TQC can also diagnose realistic materials. In Chapter 3, we apply the formalism to PbTe, which was predicted to host Dirac fermions on a two-dimensional antiphase boundary on an "old", simplified tight binding model. Within TQC, we compute the symmetry indicators of filled bands to find a nontrivial $\nu_{\mathbb{Z}_8} = 4$ index, which could correspond to two different topological insulator states. By means of Wilson loop calculations both in the TB model and ab initio calculations, we conclude that PbTe is a mirror Chern insulator. Furthermore, we show that even if the original model lacked the symmetries of the PbTe lattice, any symmetric completion of the model is analogously topological. Thus, their findings are now well understood in the framework of topological crystalline insulators. Even though PbTe has been experimentally found to be a trivial insulator, our calculations for several values of the lattice constant show that, taken optimistically, PbTe is close to a TI transition. These results remark the importance of finding the appropriate exchange correlation functional to describe the system at hand, which is necessary to achieve a good prediction of the gap but it is crucial to determine the topology of narrow-gapped materials.

We showed the important role crystalline symmetries have on topology, both for predicting and protecting topological phases. We then study the effect symmetry breaking has on topology. In Chapter 4, we study a particular example of time reversal

symmetry breaking (magnetic) material, extensively studied metallic ferromagnetic CoS_2. We found a family of 8 Weyl nodes close to the Fermi level, which are allowed due to TRS breaking, even though inversion symmetry is present. Following the surface spectrum analysis, we also find single and double Fermi arcs connecting the projection of Weyl nodes into the (100) surface facet. Remarkably, the Fermi arcs are completely spin polarized in the direction of the majority spin. Thus, even if there is a minority spin pocket in the bulk, we expect the density of states of the majority spin to be increased due to the spin polarized Fermi arcs. We also find Nodal lines near the Fermi level, which have drumhead states in the (001) facet. One of the most remarkable results of this work is that new physics can be hidden in materials that have been extensively studied in the past. Thus, there are whole families of very well characterized materials, which are accesible either by growing or found in nature, that can host new topological phases that can be accessed experimentally.

Lastly, we analyze the symemtry breaking of crystalline symmetries by means of strain. We analyze the effect strain has on a topological multifold fermion, the 3-fold. It can be found in 3D materials with tetrahedral space groups, such as $P2_13$ (198). We found a new, purely 3 dimensional response to time-dependent strain, which we name Hall viscosity analogously to the 2D case. Following the phonon and continuity methods, we compute the value of this viscosity explicitly in a toy model, that serves as a proxy for 3D chiral magnets, such as the family of Mn_3IrSi. We expect this viscosity has measurable effects both from the phonon method as new force terms in the phonon dispersion and from the momentum coninuity method in measurements of local flow profiles or in thermoelectric transport coefficients. Our work paves the way for studying purely 3D Hall viscosity coefficients for other systems with reduced symmetry, such as the cubic chiral magnet $MnTe_2$ in MSG $Pa\bar{3}$ (205.33).

Acknowledgements

I would like to begin acknowledging the topological group in the DIPC. Thank you Fernando, Mikel, Chiara, Mikel and everyone for endless discussions about the SSH model and other topics that have helped me greatly to understand the basis of our field.

Thank you Juan Luis for your mentoring and advice, and for the long hours in your office where I went every other day asking very inquisitively about group theory and symmetries. The way in which you explain difficult subjects is the best I've known so far and I hope if I ever get to be a professor, some of it rubbed off on me and I can apply it.

Thank you Aitor for teaching me what DFT is, as it will be the basis for my whole career. Thank you for supporting me in every project we started. And a big thank you for setting the first meeting, in what it seems now a long time ago, between you, Maia and myself.

Maia, I don't really know where to start. I would like to thank your mentoring, the long hours discussing projects, discussing physics... I could go on for pages. But I want to remark that your help has been far from being your job. You have dedicated a lot of your time to teaching me in all fronts, not only on the theoretical part but on how to be a better scientist. I know that the beginning wasn't easy. I have to admit that the middle part was especially hard too. But I hope I emerge as a better scientist than I was at the beginning. Thank you for your personal implication in my life too, you have been very supporting and understanding of my personal circumstances and you have always known how and to which extent to push me to arrive where we are today, summarizing our work in this thesis. Thanks again, I would not have made it here if it weren't for you.

Cambiando de registro, me gustaría agradecer a todo mi entorno personal por el apoyo que me han dado durante todo este largo proceso. 4 años que he pasado dedicado a formarme como investigador y que al final concluye en esta tesis. Gracias a todos mis amigos de Irun/Hondarribi por aguantar las extensas charlas sobre materiales topológicos. Gracias a mi familia de Irun, Pilar, Fontxo, Isabel por acogerme y tratarme como familia. Gracias Asier por corregirme tantas veces texto que te

mandaba a horas intempestivas y por intentar entender qué es eso raro a lo que me dedico.

Gracias aita y Asi, por vuestro apoyo incondicional durante tantos años. Los últimos meses no han sido los mejores para nosotros, pero nos han unido más de lo que habíamos estado nunca y me tranquiliza saber que estamos todos pendientes los unos de los otros.

Agradecezco eternamente todo tu apoyo y cariño, Isabel. Por escucharme sobre física, por apoyarme tanto en los buenos como en los malos momentos, por esos cafés a media tarde para terminar un proyecto, por todos los años que llevamos juntos y los que nos quedan.

Por último, muchas gracias, ama. Me duele mucho que no puedas estar el día de la defensa. Igual que este momento, vas a perderte muchos otros en los que deberías haber estado. Pero no te preocupes, no ha pasado un día en que no te haya tenido presente en mi vida. Siempre vas a ser mi guía. Muchas gracias por traerme al mundo y hasta donde estamos hoy. Espero que puedas estar orgullosa.

List of Publications

Here we provide a list of publications during the thesis. The main results of our work are published in the first set of publications, while the second set accounts for collaborations in different projects.

Thesis publications

- *Band Theory Without Any Hamiltonians or "The Way Band Theory Should Be Taught"*
  Iñigo Robredo, B. A. Bernevig, J. L. Mañes
  Topological Matter: Lectures from the Topological Matter School, (2017)

- *Higher-order and crystalline topology in a phenomenological tight-binding model of lead telluride*
  Iñigo Robredo, M. G. Vergniory, B. Bradlyn
  Physical Review Materials 3, 041202 (2019)

- *Weyl fermions, Fermi arcs, and minority-spin carriers in ferromagnetic CoS2*
  N. B. M. Schröter*, **Iñigo Robredo***, S. Klemenz, R. J. Kirby, J. A. Krieger, D. Pei, T. Yu, S. Stolz, T. Schmitt, P. Dudin, T. K. Kim, C. Cacho, A. Schnyder, A. Bergara, V. N. Strocov, F. de Juan, M. G. Vergniory, L. M. Schoop
  Science Advances 6, (2020)

- *Theoretical study of topological properties of ferromagnetic pyrite CoS2*
  Iñigo Robredo, N. B. M. Schröter, A. Reyes-Serrato, A. Bergara, F. de Juan, L. M. Schoop, M. G. Vergniory
  Submitted to J. Phys. D, arxiv:2109.14665 (2021)

- *Cubic Hall viscosity in three-dimensional topological semimetals*
  Iñigo Robredo, P. Rao, F. de Juan, A. Bergara, J. L. Mañes, A. Cortijo, M.G. Vergniory, B. Bradlyn
  Physical Review Research 3, (2021)

Collaborations

- *Large Multidirectional Spin-to-Charge Conversion in Low-Symmetry Semimetal MoTe2 at Room Temperature*
  C. K. Safeer, N. Ontoso, J. Ingla-Aynés, F. Herling, V. T. Pham, A. Kurzmann, K. Ensslin, A. Chuvilin, **Iñigo Robredo**, M. G. Vergniory, F. de Juan, L. E. Hueso, M. Reyes Calvo, F. Casanova
  Nano letters 19, (2019)

- *A New Three-Dimensional Subsulfide Ir2In8S with Dirac Semimetal Behavior*
  J. F. Khoury, A. J. E. Rettie, M. A. Khan, N. J. Ghimire, **Iñigo Robredo**, J. E. Pfluger, K. Pal, C. Wolverton, A. Bergara, J. S. Jiang, L. M. Schoop, M. G. Vergniory, J. F. Mitchell, D. Y. Chung, M. G. Kanatzidis
  Journal of the American Chemical Society 141, 19130-19137 (2019)

- *The Subchalcogenides Ir2In8Q (Q = S, Se, Te): Dirac Semimetal Candidates with Re-entrant Structural Modulation*
  J. F. Khoury, A. J. E. Rettie, **Iñigo Robredo**, M. J. Krogstad, C. D. Malliakas, A. Bergara, M. G. Vergniory, R. Osborn, S. Rosenkranz, D. Y. Chung, M. G. Kanatzidis
  Journal of the American Chemical Society 142, 6312-6323 (2020)

- *Spectral and optical properties of Ag3Au (Se2, Te2) and dark matter detection*
  M.-Á. Sánchez-Martínez*, **Iñigo Robredo***, A. Bidaurrazaga, A. Bergara, F. de Juan, A. G. Grushin, M. G. Vergniory
  Journal of Physics: Materials 3, 014001 (2019)

- *Cubic 3D Chern photonic insulators with orientable large Chern vectors*
  C. Devescovi, M. García-Díez, **Iñigo Robredo**, M. B. de Paz, B. Bradlyn, J. L. Mañes, M. G. Vergniory, A. García-Etxarri
  Submitted to Nature Communications, arxiv:2105.12725, (2021)

Appendix A

Definitions

Definition 6. (Bravais lattice). A *Bravais lattice* is an infinite set of translations $\boldsymbol{t}$ generated by d linearly independent vectors $\vec{a}_i$, where d is the dimension of the crystal

$$\boldsymbol{t} = n_1\vec{a}_1 + \ldots + n_d\vec{a}_d \quad , \quad n_i \in Z \tag{A.1}$$

The Bravais lattice is thus isomorphic to Z^d.

Definition 7. (Crystal). A *crystal* is a Bravais lattice arrangement of atoms, invariant under a space group G.

Definition 8. (Group of the crystal). The *group of the crystal* is the space group G under which the crystal remains invariant. G is always an infinite group, as it includes all integer translations along the Bravais lattice. In Seitz notation the elements of a space group G are denoted

$$g = \{R|\vec{r}\} \tag{A.2}$$

where R is a point group element and $\vec{r}$ is a translation, which may or may not belong to the Bravais lattice. The action of $g \in G$ on a real space point $\vec{q}$ is given by

$$g\vec{q} = \{R|r\}\vec{q} = R\vec{q} + \vec{r} \tag{A.3}$$

The Bravais lattice is always a subgroup of the space group G. Its elements are of the form $\{E|\boldsymbol{t}\}$, where E is the identity operation.

Definition 9. (Stabilizer group/Site-symmetry group). The *stabilizer group* or *site-symmetry group* of a position q is the set of symmetry operations $g \in G$ that leave q fixed. It is denoted by $G_q = \{g|gq = q\} \subset G$. There are a couple of things to remark:

- $g \in G_q$ may include a translation, $g = \{R|\vec{r}\}$, with $\vec{r} \neq 0$

- However, since any site-symmetry group leaves a point invariant, G_q is necessarily isomorphic to one of the 32 crystallographic point groups.

Definition 10. (Wyckoff position). A general *Wyckoff position* is a position q in the unit cell of the crystal with a trivial site-symmetry group, i.e., the only element in G_q is the identity operation. A *special* Wyckoff position is a position q in the unit cell of the crystal with a non-trivial site-symmetry group, i.e., q is invariant under some symmetry operations, such as mirror planes and rotation axis.

Definition 11. (Orbit of q). The *orbit of* q is the set of all positions which are related to q by elements of the symmetry group G, i.e., $Orb_q = \{gq|g \in G\}$ *and* belong to the same unit cell.

Definition 12. (Coset representatives). The *coset representatives* of a site-symmetry group can be defined as the set of elements that generate the orbit of a Wyckoff position. Then each element q_α in the orbit of q may be written as $q_\alpha = g_\alpha q$.

Definition 13. (Coset decomposition). The *coset decomposition* of the full space group is defined by

$$G = \bigcup_\alpha g_\alpha (G_q \ltimes Z^d) \tag{A.4}$$

where G_q is the site-symmetry group and g_α are the coset representatives. The piece multiplying the coset representatives is obtained as the semi-direct product of G_q and the translation group, that in d dimensions is isomorphic to Z^d. Each term $g_\alpha(G_q \ltimes Z^d)$ in Eq. (A.4) is a (left) *coset*.

This can be understood as follows. Let us take a position q with site-symmetry group G_q.Then G_q plus the translations in the Bravais lattice creates a replica of q at every primitive cell in the crystal. Acting with each coset representative g_α creates, throughout the crystal, replicas of every position in the orbit of q.

Definition 14. (Multiplicity of a Wyckoff position). The *multiplicity of a Wyckoff position* is defined as the number of elements (positions) in the orbit of some Wyckoff position. It is obviously equal to the number of coset representatives

This is what motivates the names for the different maximal Wyckoff positions 1a, 2b, 3c... The number tells you the multiplicity of the position, while the letter labels the positions, from more to less symmetric.

Definition 15. (Maximal Wyckoff position). A Wyckoff position q is said to be *non-maximal* if there exists a group H such that $G_q \subset H \subset G$. A Wyckoff position that is not non-maximal is *maximal*.

A sufficient (although not necessary) condition for a position q to be maximal is that q is the unique point fixed by every operation in G_q. As a particular case, in 2D, any site-symmetry group that contains rotations is maximal.

Definition 16. (Little group). Two reciprocal space vectors $\mathbf{k}_1$ and $\mathbf{k}_2$ are said to be equivalent, $\mathbf{k}_1 \equiv \mathbf{k}_2$, if there exists a reciprocal *lattice* vector $\vec{K}$ such that $\mathbf{k}_2 = \mathbf{k}_1 + \vec{K}$. Then the *little group* $G_{\mathbf{k}}$ of a vector $\mathbf{k}$ in reciprocal space is the set of elements $g \in G$ such that $g\mathbf{k} \equiv \mathbf{k}$. Note that the action of space group elements on reciprocal space vectors is defined by

$$g\mathbf{k} = \{R|\boldsymbol{t}\}\mathbf{k} = R\mathbf{k} \tag{A.5}$$

Definition 17. (Small representation). A *small representation* is a representation of the little group.

Appendix B

Proof that the site symmetry groups for the 3c Wyckoff positions are isomorphic to C_{3v}

In this appendix we will proof two statements; first, that the site-symmetry group for the position $q = \left(\frac{1}{3}, \frac{1}{3}\right)$ is isomorphic to C_{3v} and second, that the site-symmetry groups for positions in the same orbit are isomorphic to each other.

B.1 Site-symmetry group of $q = \left(\frac{1}{3}, \frac{1}{3}\right)$

First, we introduce the set of relations that define the group C_{3v}:

$$\begin{aligned} &C_3^3 = 1: \\ &\qquad (x,y) \to C_3 \to (y, -x-y) \to C_3 \to (-x-y, x) \to C_3 \to (x,y) \\ &C_3 m_{1\bar{1}} = m_{1\bar{1}} C_3^{-1}: \\ &\qquad (x,y) \to m_{1\bar{1}} \to (y,x) \to C_3 \to (x, -x-y) \\ &\qquad (x,y) \to C_3^2 \to (-x-y, x) \to m_{1\bar{1}} \to (x, -x-y) \end{aligned} \tag{B.1}$$

Now, let's see if the generators of the site-symmetry group follow the same relations:

$$
\begin{aligned}
&\{C_3|01\}^3 = 1: \\
&\qquad (x,y) \to \{C_3|01\} \to (y, -x-y+1) \to \{C_3|01\} \to (-x-y+1, x) \to \{C_3|01\} \to (x,y) \\
&\{C_3|01\}\{m_{1\bar{1}}|0\} = \{m_{1\bar{1}}|0\}\{C_3|01\}^{-1}: \\
&\qquad (x,y) \to \{m_{1\bar{1}}|0\} \to (y,x) \to \{C_3|01\} \to (x, -x-y+1) \\
&\qquad (x,y) \to \{C_3|01\}^2 \to (-x-y+1, x) \to \{m_{1\bar{1}}|0\} \to (x, -x-y+1)
\end{aligned}
\tag{B.2}
$$

As we see, the group generators satisfy the same relations. Thus the groups are isomorphic.

B.2 Site-symmetry group of positions in the same orbit

We know that the positions for the different elements in the same orbit are related to each other by

$$q_\alpha = g_\alpha q \tag{B.3}$$

for some q in the orbit and g_α a coset representative. Thus, for some $h \in G_q$,

$$hq = q \to g_\alpha h g_\alpha^{-1} q_\alpha = q_\alpha \tag{B.4}$$

and we see that $g_\alpha h g_\alpha^{-1} \in G_{q_\alpha}$. This is the definition of *conjugate group*. As two conjugate groups are isomorphic, it is enough to compute the site-symmetry group for one point in each orbit.

Appendix C

Wannier function transformation properties

We will denote our Wannier functions on the unit cell by two indices: the orbital (latin) and site (greek). In the case of spinful p_z orbitals on 2b Wyckoff positions (graphene), the Wannier functions will be denoted as $W_{i\alpha}$, where i denotes spin up or down, and α denotes the site of the orbit. Wannier functions transform around each site as orbitals:

$$gW_{i1} = [\rho(g)]_{ji} W_{j1} \tag{C.1}$$

This follows from the Hamiltonian. If the Hamiltonian commutes with the symmetry operations, then its eigenstates[1] transform under representations of the symmetry group. In a unit cell we have α positions in the orbit. The Wannier functions at those points are given, in terms of the functions around one position:

$$W_{i\alpha}(\mathbf{r}) = g_\alpha W_{i1}(\mathbf{r}) = W_{i1}(g_\alpha^{-1}\mathbf{r}) \tag{C.2}$$

Let's see under which representation these transform:

$$hW_{i\alpha} = g_\alpha g g_\alpha^{-1} g_\alpha W_{i1} = g_\alpha g W_{i1} = g_\alpha [\rho(g)]_{ji} W_{j1} = [\rho(g_\alpha^{-1} h g_\alpha)]_{ji} W_{j\alpha} \tag{C.3}$$

where $h \in G_{q_\alpha}$ and $g \in G_{q_1}$.

Now, we can construct all Wannier functions on the full lattice by translating these functions along the lattice. $\{E|t_\mu\}W_{i\alpha}(\mathbf{r}) = W_{i\alpha}(\mathbf{r} - \boldsymbol{t}_\mu)$, so we have a total of $n \times n_q \times N$ Wannier functions, where n_q is the number of orbitals per position in the orbit, n the multiplicity of the Wyckoff position and N the number of cells of

[1] Or a set of states that generate the same Hilbert space.

our crystal. These functions form a *basis* for the representation of the space group induced from the representation of the site-symmetry group. Let the representation of the spatial group be ρ_G. Then, $\rho_G \equiv \rho \uparrow G$. This procedure is called *induction*. Let's proceed to see how Wannier states transform under an element $h = \{R|\boldsymbol{t}\}$:

$$\begin{aligned} hW_{i\alpha}(\mathbf{r}-\boldsymbol{t}_\mu) &= h\{E|\boldsymbol{t}_\mu\}W_{i\alpha}(\mathbf{r}) \\ &= \{E|R\boldsymbol{t}_\mu\}hW_{i\alpha}(\mathbf{r}) \\ &= \{E|R\boldsymbol{t}_\mu+\boldsymbol{t}_{\beta\alpha}\}g_\beta g g_\alpha^{-1}W_{i\alpha}(\mathbf{r}) \\ &= \{E|R\boldsymbol{t}_\mu+\boldsymbol{t}_{\beta\alpha}\}g_\beta g W_{i1}(\mathbf{r}) \\ &= \{E|R\boldsymbol{t}_\mu+\boldsymbol{t}_{\beta\alpha}\}g_\beta[\rho(g)]_{ji}W_{j1}(\mathbf{r}) \\ &= \{E|R\boldsymbol{t}_\mu+\boldsymbol{t}_{\beta\alpha}\}[\rho(g)]_{ji}W_{j\beta}(\mathbf{r}) \\ &= [\rho(g)]_{ji}W_{j\beta}(\mathbf{r}-R\boldsymbol{t}_\mu-\boldsymbol{t}_{\beta\alpha}) \end{aligned} \tag{C.4}$$

where in the third line we have used that the action of an element h on a Wyckoff position q_α is given by

$$hq_\alpha = \{E|\boldsymbol{t}_{\beta\alpha}\}q_\beta, \quad g_\beta^{-1}\{E|-\boldsymbol{t}_{\beta\alpha}\}hg_\alpha q_1 = q_1 \equiv gq_1 = q_1 \tag{C.5}$$

where the vector $\boldsymbol{t}_{\beta\alpha}$ represents the possibility of an element to take some Wyckoff away to another cell[2]. We see here that we can know how any Wannier in any position in any cell transform just by knowing how they transform around one of the positions of the orbit under an element $g \equiv g_\beta^{-1}\{E|-\boldsymbol{t}_{\beta\alpha}\}hg_\alpha \in G_{q_1}$. We can obtain from Eq. (2.19) that:

$$\boldsymbol{t}_{\beta\alpha} = hq_\alpha - q_\beta \tag{C.6}$$

[2]It can be easily seen from here that there is only one value of β for which α makes sense. As an example, let the element h take the Wyckoff position q_1 to q_3 in another cell, with a translation $\boldsymbol{a}$ being an integer Bravais lattice vector. In this notation, we will have that $\boldsymbol{t}_{31} = \boldsymbol{a}$, while the rest of $\boldsymbol{t}_{\beta 1}$ will not exist and, thus, the blocks of the full group representation that are not $\alpha = 1$, $\beta = 3$ will be 0.

Appendix D

Elementary Band Representation

In the main text we have worked out an example of elementary band representation. We will give here some more general results about them. First, let's state some facts.

We say that two band representations ρ_G and σ_G are equivalent if and only if there exists a unitary matrix-valued function $S(\mathbf{k}, t, g)$ smooth in $\mathbf{k}$ and continuous in t such that, for all $g \in G$

- $S(\mathbf{k}, t, g)$ defines a band representation according to Eq. (2.14) for all $t \in [0, 1]$
- $S(\mathbf{k}, 0, g) = \rho_G^{\mathbf{k}}(g)$
- $S(\mathbf{k}, 1, g) = \sigma_G^{\mathbf{k}}(g)$

A necessary condition is that both $\rho_G^{\mathbf{k}}(g)$ and $\sigma_G^{\mathbf{k}}(g)$ restrict to the same little group representations at all points in the Brillouin zone. However, it is not sufficient: it may happen that both representations satisfy this condition but $S(\mathbf{k}, t, g)$ is not a band representation for all t. We need a sufficient condition for equivalence:

Given two sites q, q' (not necessarily in the same Wyckoff position), and representations of their site-symmetry groups (ρ of G_q and ρ' of $G_{q'}$), the band representations $\rho \uparrow G$ and $\rho' \uparrow G$ are equivalent if and only if there exists a site q_0 and representation σ of G_{q_0} such that $\rho = \sigma \uparrow G_q$ and $\rho' = \sigma \uparrow G_{q'}$.

Now let's discuss about the compositeness of a band representation, i.e., if it is elementary or composite. We say that a band representation is composite if it can obtained as a sum of other band representations. A band representation that is not composite is called *elementary*.

All band representations admit a description in terms of localized Wannier functions. They are induced from the representations of some site-symmetry group with local orbitals. Notice that if we induce a band representation from a reducible representation of the site-symmetry group:

$$(\rho_1 \oplus \rho_2) \uparrow G = (\rho_1 \uparrow G) \oplus (\rho_2 \uparrow G) \tag{D.1}$$

where we have used the distributive property of the direct sum. So, if we are interested in elementary band representations, we only need to take care of irreducible representations of the site-symmetry group. Moreover, since $(\rho \uparrow H) \uparrow G = \rho \uparrow G$, we only need to consider maximal subgroups of the space group (hence our interest on maximal Wyckoff positions).

We have determined that all elementary band representations can be induced from irreducible representations of the maximal site-symmetry groups. But this condition is not true in the opposite way; not all irreducible representation of the maximal site-symmetry groups *induce an elementary band representation*. These last cases, when what is induced is not an elementary band representation, are called *exceptions*. This may seem annoying, but they have already been tabulated in Ref. [41] and made accesible in the BCS [67–69].

Hence (with some exceptions), band representations induced from irreducible representations of maximal site-symmetry groups give elementary band representations, whose bands are connected in the first BZ (they have no gap).

Band representations describe systems in the atomic limit, as they can be described by maximally localized Wannier orbitals. A trivial insulator is one whose bands can be obtained from maximally localized Wannier orbitals, so it does not have edge states.

Then, a set of bands that is not a band representation cannot be described in terms of localized Wannier orbitals and is, thus, topological. We call this bands, that are a solution to compatibility relations, a *quasi band representation*.

Let's analyze the following example, alike the graphene case. Suppose we have a Hamiltonian constructed from localized orbitals, whose EBR is $\rho_G = \rho \uparrow G$, and that the energy bands of this system can be divided into two disconnected sets of bands over all $\mathbf{k}$ in the first BZ, separated by a spectral gap. This means that the action of every element in the symmetry group on one of the states of one the bands *does not take it out of it*. Formally, let P_i be the projector into the band i. Then:

$$[P_i, H] = 0, \quad [P_i, g] = 0 \tag{D.2}$$

for all $g \in G$. Now suppose that the bands of projector P_i transform under a band representation ρ_G^i. Then, the full ρ_G representation could be constructed as a direct sum of the band representations of the different bands. We reached a contradiction: starting with an elementary band representation, we got a composite band representation. So, all bands that transform according to an elementary band representation *must be connected along the first BZ*, otherwise they are not a band representation

and, thus, they are topological, in the sense that there is at least one subset of them that is topological.

List of Figures

1.1 Wilson loop in the case of a single band. (a) Zak phase integration in the k_2 direction, as a function of k_1^0. (b) and (c) Wilson Loop calculation. (b) Chern number $C = 0$ Wilson Loop. (c) Chern number $C = 1$ Wilson loop. 22

1.2 Crystal structure of the SSH model. Solid points represent orbital positions and solid lines represent tight binding hopping parameters. Red points represent the location of inversion symmetry centers. . . . 23

1.3 Limit cases of the SSH model. (a) Trivial case. The crystal becomes a succession of isolated dimers. (b) Non-trivial case. The dimers connect neighboring cells, so there will be an edge state when making the model finite. Notice that a redefinition of the origin would reverse the definition of trivial and non-trivial. 24

2.1 Hexagonal lattice on the 6mm (17) wallpaper group. 28

2.2 Action of the symmetry operators on the basis vectors. 29

2.3 Maximal Wyckoff positions for the wallpaper group 17. 30

2.4 Action of the C_3 axis on Wyckoff positions. In green, the original positions. In blue, the new position after the action of the rotation. In red, the unit cells. 41

2.5 First Brillouin Zone for graphene. 45

2.6 Different connectivities allowed by compatibility relations: (a) Connected set of bands, (b) disconnected set of bands. 47

3.1 (a) PbTe crystal structure. It has the same structure as rocksalt (NaCl), in SG $Fm\bar{3}m$ (225). (b) Brillouin Zone for SG $Fm\bar{3}m$ (225) [67–69]. 51

3.2 (a) and (b) Spectrum of the iFDB Hamiltonian given in Eq. 3.8, with parameter values $t = \delta_2 = 0.5$, $\delta_1 = 0.1$. In (a) we take $m = 0.3$, while in (b) we take $m = -0.3$. (c) Wilson loop in the k_2 direction evaluated in the space of the lowest two bands of the model in Eq. 3.8 with $m < 0$, as a function of k_3, with $k_1 = 0$. We see that the Wilson loop phases Θ wind twice around the circle $(-\pi, \pi]$. This implies that the model is in a topological phase with mirror Chern number $\nu_{m_{1\bar{0}}} = 2$. (d) Spectrum for the topological phase of the iFDB model for a $\hat{z}$-normal slab. Note the mirror-symmetry protected Dirac fermion on the $\bar{\Gamma} - \bar{L}$ line. 54

3.3 Bulk band structure of PbTe, calculated using the structure reported in Reference [48]. The inset shows the small gap and band inversion at the L point. 58

3.4 Hybrid Wannier charge centers for the +i mirror subspace of the occupied bands of PbTe in the m_{110}-invariant plane. (a) Raw Wannier centers (Wilson loop eigenvalues). (b) Trace of the Hybrid Wannier charge centers matrix (see Sec. 1.5). Since the trace winds twice across the unit cell, we deduce that the mirror Chern number $\nu_{m_{110}} = 2$. . . 59

4.1 (a) Crystal and magnetic structure of CoS_2. (b) and (c) Electronic band structures near the Fermi level. (b) without and (c) with SOC interaction. Inside light green circles, effect of the SOC interaction mixing spins. Inside dark green circles, 3fold degeneracy breaking when symmetry is lowered due to the SOC interaction. Inside blue circles, symmetry enforced 4fold degeneracy. 67

4.2 (a) Brillouin zone of the MSG Pb'c'a (No. 61.436) depicting the position of unequivalent M_i points (extracted from the BCS). (b) Dispersion from Γ to the different M_i points. The red arrow indicates the gap opening in M_2, as predicted by the $\mathbf{k} \cdot \mathbf{p}$ model. 69

4.3 (a) Position of the Nodal lines in the BZ. Each red rectangle represents an integrated Berry phase of π. (b) Projection of the Nodal lines in the (001) direction. (c) and (d) Berry phase calculations on the paths depicted in (b). (e) Surface calculation in the (001) cleavage plane, computed along the red path shown in (b). Notice that the drumhead surface states gap in regions where the Berry phase is equal to 0. . . . 70

4.4 (a) Position of the Weyl nodes in the BZ. (b) Surface calculation in the (100) cleavage plane in the path depicted in (d). (c) Zoomed-in schematic depiction of the surface states in the (100) cleavage plane near the $\bar{M}_2$-$\bar{R}$ line. The location of the projection of the Weyls into the surface is shown by red and blue dots. Dots with a surrounding circle represent the projection of two Weyl nodes with equal chirality. (d) Spin polarization of Fermi arcs in the surface calculation. They are polarized in the direction of the majority spin, just like the bulk bands. 71

4.5 (a) ARPES Fermi surface on the (111) cleavage plane that cuts R. We can identify circular electron pockets centered at the R point. (b) Ab initio calculation on the same cleavage plane as (a). We observe that there is qualitative agreement between experimental and theoretical calculations. (c) Experimental band dispersion on the k path depicted in (a) (black arrow). Red arrows depict electron pockets at the R point. (d) Experimental energy distribution curve at the R point. From here we extract the value of the exchange splitting (ΔE = 0.60(3) eV). (e) Ab-initio calculation of bands in the same direciton as (c). We confirm that the electron pocket in R is polarized in the direction of the minority spin. 74

4.6 (a-d) Experimental vs ab-initio calculation of Fermi surfaces. (a-b) On the (111) cleavage plane that cuts Γ. Ab-initio calculation shows qualitative agreement. (c-d) On the (100) cleavage plane that cuts Γ. Ab-initio calculation shows qualitative agreement. (e) Line cuts of the $M - \Gamma$ path extracted from both (111) and (100) cleavage planes. We clearly see the location of the 4fold degeneracy. (f) Second derivative of the spectrum in (e), improving contrast. (g) Combined band dispersion from both cleavage planes, showing the location of the Nodal line and the Weyl node. (h-i) Ab-initio calculation of bands in two close paths. (h) Location of the Nodal line. (i) Location of the Weyl node. Notice that the separation of the two paths is smaller than experimental accuracy. 76

4.7 (a) Fermi surface calculation of surface spectrum in the (100) cleavage plane. We indicate the location of the Femri arcs experimentally observable. (b) Ab-initio Fermi surface calculation of surface spectrum in the (100) cleavage plane, showing the location of Fermi arcs. (c) Line cut of experimental band spcetrum in the direction depicted in (a) (black arrow). Red arrow shows the location of one of the Fermi arcs. (d) Ab-initio calculation showing the Fermi arcs connecting Weyl nodes. There is good agreement between experimental data and ab-initio calculations. 77

5.1 Schematic of η_1 and η_2. Dynamic strains (yellow) and viscosity give rise to stresses (orange). In response to a dynamic strain that elongates the length and width of a cubic parcel of fluid while compressing the depth, η_1 produces a diagonal shear stress. In response to a dynamic rotation of the parcel, η_2 produces an off-diagonal shear stress. 88
5.2 (a) Lattice model for SG $P2_13$ (198). In red, neraest neighbors hopping. In blue, complex phase ϕ, which is responsible for TRS breaking. The arrow shows the effective magnetic field the phase creates. (b) Tight Binding model band spectrum. We set the chemical potential to cut through the threefold at Γ. (c) Continuum dispersion of the threefold fermion close to the Γ point. Λ denotes the momentum cut-off. 89
5.3 Integrated Hall viscosity as a function of chemical potential. Notice there is a jump in the MHV when $\mu = 0$. 99
5.4 (a-b) Momentum cuts ($k_z = 0$) of lattice Hall viscosity density. Notice that it complies with the symmetries of the system. (c) Numeric integration of the lattice Hall viscosity. Notice that there is no jump at $\mu = 0$. 100

Bibliography

[1] Lev Davidovich Landau. On the theory of phase transitions. I. *Phys. Z. Sowjet.*, 11:26, 1937.

[2] K. v. Klitzing, G. Dorda, and M. Pepper. New method for high-accuracy determination of the fine-structure constant based on quantized hall resistance. *Phys. Rev. Lett.*, 45:494–497, Aug 1980.

[3] David J Thouless, Mahito Kohmoto, M Peter Nightingale, and Md den Nijs. Quantized hall conductance in a two-dimensional periodic potential. *Physical review letters*, 49(6):405, 1982.

[4] F. D. M. Haldane. Model for a quantum hall effect without landau levels: Condensed-matter realization of the "parity anomaly". *Phys. Rev. Lett.*, 61:2015–2018, Oct 1988.

[5] C. L. Kane and E. J. Mele. Quantum spin hall effect in graphene. *Phys. Rev. Lett.*, 95:226801, Nov 2005.

[6] Liang Fu and C. L. Kane. Time reversal polarization and a Z_2 adiabatic spin pump. *Phys. Rev. B*, 74:195312, Nov 2006.

[7] Liang Fu and C. L. Kane. Topological insulators with inversion symmetry. *Phys. Rev. B*, 76:045302, Jul 2007.

[8] Matthew J. Gilbert. Topological electronics. *Communications Physics*, 4(1):70, Apr 2021.

[9] Liang Fu. Topological crystalline insulators. *Phys. Rev. Lett.*, 106:106802, Mar 2011.

[10] Barry Bradlyn, L. Elcoro, Jennifer Cano, M. G. Vergniory, Zhijun Wang, C. Felser, M. I. Aroyo, and B. Andrei Bernevig. Topological quantum chemistry. *Nature*, 547(7663):298–305, Jul 2017.

[11] Jennifer Cano, Barry Bradlyn, Zhijun Wang, L. Elcoro, M. G. Vergniory, C. Felser, M. I. Aroyo, and B. Andrei Bernevig. Building blocks of topological quantum chemistry: Elementary band representations. *Phys. Rev. B*, 97:035139, Jan 2018.

[12] M. G. Vergniory, L. Elcoro, Zhijun Wang, Jennifer Cano, C. Felser, M. I. Aroyo, B. Andrei Bernevig, and Barry Bradlyn. Graph theory data for topological quantum chemistry. *Phys. Rev. E*, 96:023310, Aug 2017.

[13] Barry Bradlyn, L. Elcoro, M. G. Vergniory, Jennifer Cano, Zhijun Wang, C. Felser, M. I. Aroyo, and B. Andrei Bernevig. Band connectivity for topological quantum chemistry: Band structures as a graph theory problem. *Phys. Rev. B*, 97:035138, Jan 2018.

[14] Hoi Chun Po, Haruki Watanabe, and Ashvin Vishwanath. Fragile Topology and Wannier Obstructions. pages 1–9, 2017.

[15] Zhida Song, Tiantian Zhang, Zhong Fang, and Chen Fang. Quantitative mappings between symmetry and topology in solids. *Nature Communications*, 9(1):3530, Aug 2018.

[16] L. Michel and J. Zak. Elementary energy bands in crystals are connected. *Physics Reports*, 341(1):377 – 395, 2001. Symmetry, invariants, topology.

[17] H. Bacry, L. Michel, and J. Zak. *Symmetry and classification of energy bands in crystals*, pages 289–308. Springer Berlin Heidelberg, Berlin, Heidelberg, 1988.

[18] J. Zak. Symmetry specification of bands in solids. *Phys. Rev. Lett.*, 45:1025–1028, Sep 1980.

[19] J. Zak. Band representations and symmetry types of bands in solids. *Phys. Rev. B*, 23:2824–2835, Mar 1981.

[20] Eduardo Fradkin, Elbio Dagotto, and Daniel Boyanovsky. Physical realization of the parity anomaly in condensed matter physics. *Phys. Rev. Lett.*, 57:2967–2970, Dec 1986.

[21] Eduardo Fradkin. The parity anomaly in condensed matter physics. *Nuclear Physics B - Proceedings Supplements*, 1(1):175–183, 1987. Proceedings of the Conference on Nonperturbative Methods in Field Theory.

[22] Daniel Boyanovsky, Elbio Dagotto, and Eduardo Fradkin. Anomalous currents, induced charge and bound states on a domain wall of a semiconductor. *Nuclear Physics B*, 285:340–362, 1987.

[23] M. G. Vergniory, L. Elcoro, Claudia Felser, Nicolas Regnault, B. Andrei Bernevig, and Zhijun Wang. A complete catalogue of high-quality topological materials. *Nature*, 566(7745):480–485, Feb 2019.

[24] Yuanfeng Xu, Luis Elcoro, Zhi-Da Song, Benjamin J. Wieder, M. G. Vergniory, Nicolas Regnault, Yulin Chen, Claudia Felser, and B. Andrei Bernevig. High-throughput calculations of magnetic topological materials. *Nature*, 586(7831):702–707, Oct 2020.

[25] B. Q. Lv, H. M. Weng, B. B. Fu, X. P. Wang, H. Miao, J. Ma, P. Richard, X. C. Huang, L. X. Zhao, G. F. Chen, Z. Fang, X. Dai, T. Qian, and H. Ding. Experimental discovery of weyl semimetal taas. *Phys. Rev. X*, 5:031013, Jul 2015.

[26] L. X. Yang, Z. K. Liu, Y. Sun, H. Peng, H. F. Yang, T. Zhang, B. Zhou, Y. Zhang, Y. F. Guo, M. Rahn, D. Prabhakaran, Z. Hussain, S.-K. Mo, C. Felser, B. Yan, and Y. L. Chen. Weyl semimetal phase in the non-centrosymmetric compound taas. *Nature Physics*, 11(9):728–732, Sep 2015.

[27] Su-Yang Xu, Ilya Belopolski, Nasser Alidoust, Madhab Neupane, Guang Bian, Chenglong Zhang, Raman Sankar, Guoqing Chang, Zhujun Yuan, Chi-Cheng Lee, Shin-Ming Huang, Hao Zheng, Jie Ma, Daniel S. Sanchez, BaoKai Wang, Arun Bansil, Fangcheng Chou, Pavel P. Shibayev, Hsin Lin, Shuang Jia, and M. Zahid Hasan. Discovery of a weyl fermion semimetal and topological fermi arcs. *Science*, 349(6248):613–617, 2015.

[28] B. Q. Lv, H. M. Weng, B. B. Fu, X. P. Wang, H. Miao, J. Ma, P. Richard, X. C. Huang, L. X. Zhao, G. F. Chen, Z. Fang, X. Dai, T. Qian, and H. Ding. Experimental discovery of weyl semimetal taas. *Phys. Rev. X*, 5:031013, Jul 2015.

[29] Niels B. M. Schröter, Ding Pei, Maia G. Vergniory, Yan Sun, Kaustuv Manna, Fernando de Juan, Jonas. A. Krieger, Vicky Süss, Marcus Schmidt, Pavel Dudin, Barry Bradlyn, Timur K. Kim, Thorsten Schmitt, Cephise Cacho, Claudia Felser, Vladimir N. Strocov, and Yulin Chen. Chiral topological semimetal with multifold band crossings and long fermi arcs. *Nature Physics*, 15(8):759–765, Aug 2019.

[30] Su-Yang Xu, Ilya Belopolski, Daniel S. Sanchez, Madhab Neupane, Guoqing Chang, Koichiro Yaji, Zhujun Yuan, Chenglong Zhang, Kenta Kuroda, Guang Bian, Cheng Guo, Hong Lu, Tay-Rong Chang, Nasser Alidoust, Hao Zheng, Chi-Cheng Lee, Shin-Ming Huang, Chuang-Han Hsu, Horng-Tay Jeng, Arun

Bansil, Titus Neupert, Fumio Komori, Takeshi Kondo, Shik Shin, Hsin Lin, Shuang Jia, and M. Zahid Hasan. Spin polarization and texture of the fermi arcs in the weyl fermion semimetal taas. *Phys. Rev. Lett.*, 116:096801, Mar 2016.

[31] Zhao Huang, Christopher Lane, Chao Cao, Guo-Xiang Zhi, Yu Liu, Christian E. Matt, Brinda Kuthanazhi, Paul C. Canfield, Dmitry Yarotski, A. J. Taylor, and Jian-Xin Zhu. Prediction of spin polarized fermi arcs in quasiparticle interference in cebi. *Phys. Rev. B*, 102:235167, Dec 2020.

[32] Barry Bradlyn, Jennifer Cano, Zhijun Wang, M. G. Vergniory, C. Felser, R. J. Cava, and B. Andrei Bernevig. Beyond dirac and weyl fermions: Unconventional quasiparticles in conventional crystals. *Science*, 2016.

[33] Su-Yang Xu, Ilya Belopolski, Nasser Alidoust, Madhab Neupane, Guang Bian, Chenglong Zhang, Raman Sankar, Guoqing Chang, Zhujun Yuan, Chi-Cheng Lee, Shin-Ming Huang, Hao Zheng, Jie Ma, Daniel S. Sanchez, BaoKai Wang, Arun Bansil, Fangcheng Chou, Pavel P. Shibayev, Hsin Lin, Shuang Jia, and M. Zahid Hasan. Discovery of a weyl fermion semimetal and topological fermi arcs. *Science*, 349(6248):613–617, 2015.

[34] Binghai Yan and Claudia Felser. Topological materials: Weyl semimetals. *Annual Review of Condensed Matter Physics*, 8(1):337–354, 2017.

[35] Niels B. M. Schröter, Iñigo Robredo, Sebastian Klemenz, Robert J. Kirby, Jonas A. Krieger, Ding Pei, Tianlun Yu, Samuel Stolz, Thorsten Schmitt, Pavel Dudin, Timur K. Kim, Cephise Cacho, Andreas Schnyder, Aitor Bergara, Vladimir N. Strocov, Fernando de Juan, Maia G. Vergniory, and Leslie M. Schoop. Weyl fermions, fermi arcs, and minority-spin carriers in ferromagnetic cos2. *Science Advances*, 6(51), 2020.

[36] Shin-Ming Huang, Su-Yang Xu, Ilya Belopolski, Chi-Cheng Lee, Guoqing Chang, BaoKai Wang, Nasser Alidoust, Guang Bian, Madhab Neupane, Chenglong Zhang, Shuang Jia, Arun Bansil, Hsin Lin, and M. Zahid Hasan. A weyl fermion semimetal with surface fermi arcs in the transition metal monopnictide taas class. *Nature Communications*, 6(1):7373, Jun 2015.

[37] Noam Morali, Rajib Batabyal, Pranab Kumar Nag, Enke Liu, Qiunan Xu, Yan Sun, Binghai Yan, Claudia Felser, Nurit Avraham, and Haim Beidenkopf. Fermi-arc diversity on surface terminations of the magnetic weyl semimetal co3sn2s2. *Science*, 365(6459):1286–1291, 2019.

[38] R. D. Y. Hills, A. Kusmartseva, and F. V. Kusmartsev. Current-voltage characteristics of weyl semimetal semiconducting devices, veselago lenses, and hyperbolic dirac phase. *Phys. Rev. B*, 95:214103, Jun 2017.

[39] Bing Zhao, Bogdan Karpiak, Dmitrii Khokhriakov, Annika Johansson, Anamul Md. Hoque, Xiaoguang Xu, Yong Jiang, Ingrid Mertig, and Saroj P. Dash. Unconventional charge–spin conversion in weyl-semimetal wte2. *Advanced Materials*, 32(38):2000818, 2020.

[40] Dylan Rees et al. Helicity-dependent photocurrents in the chiral weyl semimetal rhsi. *Science Advances*, 6(29), Jul 2020.

[41] Barry Bradlyn, L. Elcoro, Jennifer Cano, M. G. Vergniory, Zhijun Wang, C. Felser, M. I. Aroyo, and B. Andrei Bernevig. Topological quantum chemistry. *Nature*, 547:298–305, 2017.

[42] M. Born and R. Oppenheimer. Zur quantentheorie der molekeln. *Annalen der Physik*, 389(20):457–484, 1927.

[43] C.J. Bradley and A.P. Cracknell. *The mathematical theory of symmetry in solids: representation theory for point groups and space groups*. Clarendon Press, 1972.

[44] Neil W Ashcroft and N David Mermin. Solid state physics (holt, rinehart and winston, new york, 1976). *Google Scholar*, 403, 2005.

[45] P. Hohenberg and W. Kohn. Inhomogeneous electron gas. *Phys. Rev.*, 136:B864–B871, Nov 1964.

[46] W. Kohn and L. J. Sham. Self-consistent equations including exchange and correlation effects. *Phys. Rev.*, 140:A1133–A1138, Nov 1965.

[47] J. P. Perdew and Alex Zunger. Self-interaction correction to density-functional approximations for many-electron systems. *Phys. Rev. B*, 23:5048–5079, May 1981.

[48] Fabien Tran and Peter Blaha. Accurate band gaps of semiconductors and insulators with a semilocal exchange-correlation potential. *Phys. Rev. Lett.*, 102:226401, Jun 2009.

[49] G. Kresse and J. Hafner. Ab initio molecular dynamics for liquid metals. *Phys. Rev. B*, 47:558–561, Jan 1993.

[50] G. Kresse and J. Hafner. Ab initio molecular-dynamics simulation of the liquid-metal–amorphous-semiconductor transition in germanium. *Phys. Rev. B*, 49:14251–14269, May 1994.

[51] G. Kresse and J. Furthmüller. Efficiency of ab-initio total energy calculations for metals and semiconductors using a plane-wave basis set. *Computational Materials Science*, 6(1):15–50, 1996.

[52] G. Kresse and J. Furthmüller. Efficient iterative schemes for ab initio total-energy calculations using a plane-wave basis set. *Phys. Rev. B*, 54:11169–11186, Oct 1996.

[53] P Giannozzi, O Andreussi, T Brumme, O Bunau, M Buongiorno Nardelli, M Calandra, R Car, C Cavazzoni, D Ceresoli, M Cococcioni, N Colonna, I Carnimeo, A Dal Corso, S de Gironcoli, P Delugas, R A DiStasio Jr, A Ferretti, A Floris, G Fratesi, G Fugallo, R Gebauer, U Gerstmann, F Giustino, T Gorni, J Jia, M Kawamura, H-Y Ko, A Kokalj, E Küçükbenli, M Lazzeri, M Marsili, N Marzari, F Mauri, N L Nguyen, H-V Nguyen, A Otero de-la Roza, L Paulatto, S Poncé, D Rocca, R Sabatini, B Santra, M Schlipf, A P Seitsonen, A Smogunov, I Timrov, T Thonhauser, P Umari, N Vast, X Wu, and S Baroni. Advanced capabilities for materials modelling with quantum espresso. *Journal of Physics: Condensed Matter*, 29(46):465901, 2017.

[54] Paolo Giannozzi, Stefano Baroni, Nicola Bonini, Matteo Calandra, Roberto Car, Carlo Cavazzoni, Davide Ceresoli, Guido L Chiarotti, Matteo Cococcioni, Ismaila Dabo, Andrea Dal Corso, Stefano de Gironcoli, Stefano Fabris, Guido Fratesi, Ralph Gebauer, Uwe Gerstmann, Christos Gougoussis, Anton Kokalj, Michele Lazzeri, Layla Martin-Samos, Nicola Marzari, Francesco Mauri, Riccardo Mazzarello, Stefano Paolini, Alfredo Pasquarello, Lorenzo Paulatto, Carlo Sbraccia, Sandro Scandolo, Gabriele Sclauzero, Ari P Seitsonen, Alexander Smogunov, Paolo Umari, and Renata M Wentzcovitch. Quantum espresso: a modular and open-source software project for quantum simulations of materials. *Journal of Physics: Condensed Matter*, 21(39):395502 (19pp), 2009.

[55] Paolo Giannozzi, Oscar Baseggio, Pietro Bonfà, Davide Brunato, Roberto Car, Ivan Carnimeo, Carlo Cavazzoni, Stefano de Gironcoli, Pietro Delugas, Fabrizio Ferrari Ruffino, Andrea Ferretti, Nicola Marzari, Iurii Timrov, Andrea Urru, and Stefano Baroni. Quantum espresso toward the exascale. *The Journal of Chemical Physics*, 152(15):154105, 2020.

[56] Giovanni Pizzi, Valerio Vitale, Ryotaro Arita, Stefan Blügel, Frank Freimuth, Guillaume Géranton, Marco Gibertini, Dominik Gresch, Charles Johnson,

Takashi Koretsune, Julen Ibañez-Azpiroz, Hyungjun Lee, Jae-Mo Lihm, Daniel Marchand, Antimo Marrazzo, Yuriy Mokrousov, Jamal I Mustafa, Yoshiro Nohara, Yusuke Nomura, Lorenzo Paulatto, Samuel Poncé, Thomas Ponweiser, Junfeng Qiao, Florian Thöle, Stepan S Tsirkin, Małgorzata Wierzbowska, Nicola Marzari, David Vanderbilt, Ivo Souza, Arash A Mostofi, and Jonathan R Yates. Wannier90 as a community code: new features and applications. *Journal of Physics: Condensed Matter*, 32(16):165902, jan 2020.

[57] J. Zak. Band representations of space groups. *Physical Review B*, 26(6):3010–3023, 1982.

[58] L. Michel and J. Zak. Connectivity of energy bands in crystals. *Phys. Rev. B*, 59:5998–6001, Mar 1999.

[59] Alexey A. Soluyanov and David Vanderbilt. Computing topological invariants without inversion symmetry. *Physical Review B - Condensed Matter and Materials Physics*, 83(23), 2011.

[60] Nicola Marzari, Arash A. Mostofi, Jonathan R. Yates, Ivo Souza, and David Vanderbilt. Maximally localized wannier functions: Theory and applications. *Rev. Mod. Phys.*, 84:1419–1475, Oct 2012.

[61] C. L. Kane and E. J. Mele. Quantum Spin Hall Effect in Graphene. *Physical Review Letters*, 95(22):226801, November 2005.

[62] Jennifer Cano, Barry Bradlyn, Zhijun Wang, L. Elcoro, M. G. Vergniory, C. Felser, M. I. Aroyo, and B. Andrei Bernevig. Building blocks of topological quantum chemistry: Elementary band representations. *Phys. Rev. B*, 97:035139, Jan 2018.

[63] Barry Bradlyn, Jennifer Cano, Zhijun Wang, M. G. Vergniory, C. Felser, R. J. Cava, and B. Andrei Bernevig. Beyond dirac and weyl fermions: Unconventional quasiparticles in conventional crystals. *Science*, 353(6299), 2016.

[64] Luis Elcoro, Barry Bradlyn, Zhijun Wang, Maia G. Vergniory, Jennifer Cano, Claudia Felser, B. Andrei Bernevig, Danel Orobengoa, Gemma de la Flor, and Mois I. Aroyo. Double crystallographic groups and their representations on the Bilbao Crystallographic Server. *Journal of Applied Crystallography*, 50(5):1457–1477, Oct 2017.

[65] Luis Elcoro, Benjamin J. Wieder, Zhida Song, Yuanfeng Xu, Barry Bradlyn, and B. Andrei Bernevig. Magnetic Topological Quantum Chemistry. *arXiv e-prints*, page arXiv:2010.00598, October 2020.

[66] M.I. Aroyo, J.M. Perez-Mato, D. Orobengoa, E. Tasci, G. De La Flor, and A. Kirov. Crystallography online: Bilbao crystallographic server. *Bulgarian Chemical Communications*, 43(2):183–197, 2011. cited By 145.

[67] J. Perez-Mato, D Orobengoa, Emre Tasci, Gemma De la Flor Martin, and A Kirov. Crystallography online: Bilbao crystallographic server. *Bulgarian Chemical Communications*, 43:183–197, 01 2011.

[68] M. Aroyo, J. Perez-Mato, C. Capillas, and et al. Computing topological invariants without inversion symmetry. *Zeitschrift für Kristallographie - Crystalline Materials*, 221(1), pp. 15-27, 2018.

[69] Mois I. Aroyo, Asen Kirov, Cesar Capillas, J. M. Perez-Mato, and Hans Wondratschek. Bilbao Crystallographic Server. II. Representations of crystallographic point groups and space groups. *Acta Crystallographica Section A*, 62(2):115–128, Mar 2006.

[70] Hoi Chun Po, Ashvin Vishwanath, and Haruki Watanabe. Symmetry-based indicators of band topology in the 230 space groups. *Nature Communications*, 8(1):50, Jun 2017.

[71] Eslam Khalaf, Hoi Chun Po, Ashvin Vishwanath, and Haruki Watanabe. Symmetry indicators and anomalous surface states of topological crystalline insulators. *Phys. Rev. X*, 8:031070, Sep 2018.

[72] Tiantian Zhang, Yi Jiang, Zhida Song, He Huang, Yuqing He, Zhong Fang, Hongming Weng, and Chen Fang. Catalogue of topological electronic materials. *Nature*, 566(7745):475–479, Feb 2019.

[73] Feng Tang, Hoi Chun Po, Ashvin Vishwanath, and Xiangang Wan. Comprehensive search for topological materials using symmetry indicators. *Nature*, 566(7745):486–489, Feb 2019.

[74] D. Vanderbilt. *Berry Phases in Electronic Structure Theory: Electric Polarization, Orbital Magnetization and Topological Insulators*. Cambridge University Press, 2018.

[75] T. L. Hughes B. A. Bernevig and S. C. Zhang. Quantum spin hall effect and topological phase transition in hgte quantum wells. *Science*, 314, 1937.

[76] B. A. Bernevig and T. L. Hughes. *Topological Insulators and Topological Superconductors*. Princeton University Press, 2013.

[77] Timothy H. Hsieh, Hsin Lin, Junwei Liu, Wenhui Duan, Arun Bansil, and Liang Fu. Topological crystalline insulators in the snte material class. *Nature Communications*, 3(1):982, Jul 2012.

[78] Maryam Taherinejad, Kevin F. Garrity, and David Vanderbilt. Wannier center sheets in topological insulators. *Phys. Rev. B*, 89:115102, Mar 2014.

[79] D. Gresch, G. Autès, O. V. Yazyev, M. Troyer, D. Vanderbilt, B. A. Bernevig, and A. A. Soluyanov. Z2Pack: Numerical implementation of hybrid Wannier centers for identifying topological materials. *Phys. Rev. B*, 95(7):075146, February 2017.

[80] Rui Yu, Xiao Liang Qi, Andrei Bernevig, Zhong Fang, and Xi Dai. Equivalent expression of F_2 topological invariant for band insulators using the non-abelian berry connection. *Phys. Rev. B*, 84:075119, Aug 2011.

[81] A. Alexandradinata, Chen Fang, Matthew J. Gilbert, and B. Andrei Bernevig. Spin-orbit-free topological insulators without time-reversal symmetry. *Phys. Rev. Lett.*, 113:116403, Sep 2014.

[82] A. Alexandradinata, Zhijun Wang, and B. Andrei Bernevig. Topological insulators from group cohomology. *Phys. Rev. X*, 6:021008, Apr 2016.

[83] F. Schindler, A. M. Cook, M. G. Vergniory, Z. Wang, S. Parkin, B. A. Bernevig, and T. Neupert. Higher-order topological insulators. *Science Advances*, 4, Jun 2018.

[84] Y. Noda, K. Masumoto, S. Ohba, Y. Saito, K. Toriumi, Y. Iwata, and I. Shibuya. Temperature dependence of atomic thermal parameters of lead chalcogenides, pbs, pbse and pbte. *Acta Crystallographica Section C*, 43(8):1443–1445, 1987.

[85] D. Hobbs, G. Kresse, and J. Hafner. Fully unconstrained noncollinear magnetism within the projector augmented-wave method. *Phys. Rev. B*, 62:11556–11570, Nov 2000.

[86] Igor Levin. Nist inorganic crystal structure database (icsd). *NIST*, 2018.

[87] Y. Sternberg, N. Yellin, S. Cohen, and L.Ben Dor. Lattice matching and thermal expansion in the pbsnte system. *Journal of Solid State Chemistry*, 43(3):364–367, 1982.

[88] Kerstin Hummer, Andreas Grüneis, and Georg Kresse. Structural and electronic properties of lead chalcogenides from first principles. *Phys. Rev. B*, 75:195211, May 2007.

[89] Robert-Jan Slager, Louk Rademaker, Jan Zaanen, and Leon Balents. Impurity-bound states and green's function zeros as local signatures of topology. *Phys. Rev. B*, 92:085126, Aug 2015.

[90] Raquel Queiroz, Ion Cosma Fulga, Nurit Avraham, Haim Beidenkopf, and Jennifer Cano. Partial lattice defects in higher-order topological insulators. *Phys. Rev. Lett.*, 123:266802, Dec 2019.

[91] Wladimir A. Benalcazar, Tianhe Li, and Taylor L. Hughes. Quantization of fractional corner charge in C_n-symmetric higher-order topological crystalline insulators. *Phys. Rev. B*, 99:245151, Jun 2019.

[92] Ching-Kai Chiu, Jeffrey C. Y. Teo, Andreas P. Schnyder, and Shinsei Ryu. Classification of topological quantum matter with symmetries. *Rev. Mod. Phys.*, 88:035005, Aug 2016.

[93] N. P. Armitage, E. J. Mele, and Ashvin Vishwanath. Weyl and dirac semimetals in three-dimensional solids. *Rev. Mod. Phys.*, 90:015001, Jan 2018.

[94] A.A. Burkov. Weyl metals. *Annual Review of Condensed Matter Physics*, 9(1):359–378, 2018.

[95] Hongming Weng, Chen Fang, Zhong Fang, B. Andrei Bernevig, and Xi Dai. Weyl semimetal phase in noncentrosymmetric transition-metal monophosphides. *Phys. Rev. X*, 5:011029, Mar 2015.

[96] Yan Sun, Shu-Chun Wu, Mazhar N. Ali, Claudia Felser, and Binghai Yan. Prediction of weyl semimetal in orthorhombic $mote_2$. *Phys. Rev. B*, 92:161107, Oct 2015.

[97] Xiangang Wan, Ari M. Turner, Ashvin Vishwanath, and Sergey Y. Savrasov. Topological semimetal and fermi-arc surface states in the electronic structure of pyrochlore iridates. *Phys. Rev. B*, 83:205101, May 2011.

[98] Gang Xu, Hongming Weng, Zhijun Wang, Xi Dai, and Zhong Fang. Chern semimetal and the quantized anomalous hall effect in $hgcr_2se_4$. *Phys. Rev. Lett.*, 107:186806, Oct 2011.

[99] Zhijun Wang, M. G. Vergniory, S. Kushwaha, Max Hirschberger, E. V. Chulkov, A. Ernst, N. P. Ong, Robert J. Cava, and B. Andrei Bernevig. Time-reversal-breaking weyl fermions in magnetic heusler alloys. *Phys. Rev. Lett.*, 117:236401, Nov 2016.

[100] J.-R. Soh, F. de Juan, M. G. Vergniory, N. B. M. Schröter, M. C. Rahn, D. Y. Yan, J. Jiang, M. Bristow, P. Reiss, J. N. Blandy, Y. F. Guo, Y. G. Shi, T. K. Kim, A. McCollam, S. H. Simon, Y. Chen, A. I. Coldea, and A. T. Boothroyd. Ideal weyl semimetal induced by magnetic exchange. *Phys. Rev. B*, 100:201102, Nov 2019.

[101] D. F. Liu, A. J. Liang, E. K. Liu, Q. N. Xu, Y. W. Li, C. Chen, D. Pei, W. J. Shi, S. K. Mo, P. Dudin, T. Kim, C. Cacho, G. Li, Y. Sun, L. X. Yang, Z. K. Liu, S. S. P. Parkin, C. Felser, and Y. L. Chen. Magnetic weyl semimetal phase in a kagomé crystal. *Science*, 365(6459):1282–1285, 2019.

[102] Ilya Belopolski, Kaustuv Manna, Daniel S. Sanchez, Guoqing Chang, Benedikt Ernst, Jiaxin Yin, Songtian S. Zhang, Tyler Cochran, Nana Shumiya, Hao Zheng, Bahadur Singh, Guang Bian, Daniel Multer, Maksim Litskevich, Xiaoting Zhou, Shin-Ming Huang, Baokai Wang, Tay-Rong Chang, Su-Yang Xu, Arun Bansil, Claudia Felser, Hsin Lin, and M. Zahid Hasan. Discovery of topological weyl fermion lines and drumhead surface states in a room temperature magnet. *Science*, 365(6459):1278–1281, 2019.

[103] Chao-Xing Liu, Shou-Cheng Zhang, and Xiao-Liang Qi. The quantum anomalous hall effect: Theory and experiment. *Annual Review of Condensed Matter Physics*, 7(1):301–321, 2016.

[104] Stephen L. Adler. Axial-vector vertex in spinor electrodynamics. *Phys. Rev.*, 177:2426–2438, Jan 1969.

[105] Niels B. M. Schröter, Ding Pei, Maia G. Vergniory, Yan Sun, Kaustuv Manna, Fernando de Juan, Jonas. A. Krieger, Vicky Süss, Marcus Schmidt, Pavel Dudin, Barry Bradlyn, Timur K. Kim, Thorsten Schmitt, Cephise Cacho, Claudia Felser, Vladimir N. Strocov, and Yulin Chen. Chiral topological semimetal with multifold band crossings and long fermi arcs. *Nature Physics*, 15(8):759–765, Aug 2019.

[106] Xitong Xu, Xirui Wang, Tyler A. Cochran, Daniel S. Sanchez, Guoqing Chang, Ilya Belopolski, Guangqiang Wang, Yiyuan Liu, Hung-Ju Tien, Xin Gui, Weiwei Xie, M. Zahid Hasan, Tay-Rong Chang, and Shuang Jia. Crystal growth and quantum oscillations in the topological chiral semimetal cosi. *Phys. Rev. B*, 100:045104, Jul 2019.

[107] Daniel S. Sanchez, Ilya Belopolski, Tyler A. Cochran, Xitong Xu, Jia-Xin Yin, Guoqing Chang, Weiwei Xie, Kaustuv Manna, Vicky Süß, Cheng-Yi Huang, Nasser Alidoust, Daniel Multer, Songtian S. Zhang, Nana Shumiya, Xirui Wang, Guang-Qiang Wang, Tay-Rong Chang, Claudia Felser, Su-Yang Xu, Shuang Jia, Hsin Lin, and M. Zahid Hasan. Topological chiral crystals with helicoid-arc quantum states. *Nature*, 567(7749):500–505, Mar 2019.

[108] Daichi Takane, Zhiwei Wang, Seigo Souma, Kosuke Nakayama, Takechika Nakamura, Hikaru Oinuma, Yuki Nakata, Hideaki Iwasawa, Cephise Cacho, Timur Kim, Koji Horiba, Hiroshi Kumigashira, Takashi Takahashi, Yoichi Ando, and Takafumi Sato. Observation of chiral fermions with a large topological charge and associated fermi-arc surface states in cosi. *Phys. Rev. Lett.*, 122:076402, Feb 2019.

[109] Nitesh Kumar, Mengyu Yao, Jayita Nayak, Maia G. Vergniory, Jörn Bannies, Zhijun Wang, Niels B. M. Schröter, Vladimir N. Strocov, Lukas Müchler, Wujun Shi, Emile D. L. Rienks, J. L. Mañes, Chandra Shekhar, Stuart S. P. Parkin, Jörg Fink, Gerhard H. Fecher, Yan Sun, B. Andrei Bernevig, and Claudia Felser. Signatures of sixfold degenerate exotic fermions in a superconducting metal pdsb2. *Advanced Materials*, 32(11):1906046, 2020.

[110] Niels B. M. Schröter, Samuel Stolz, Kaustuv Manna, Fernando de Juan, Maia G. Vergniory, Jonas A. Krieger, Ding Pei, Thorsten Schmitt, Pavel Dudin, Timur K. Kim, and et al. Observation and control of maximal chern numbers in a chiral topological semimetal. *Science*, 369(6500):179–183, Jul 2020.

[111] Maia G. Vergniory, Luis Elcoro, Fabio Orlandi, Benjamin Balke, Yang-Hao Chan, Juergen Nuss, Andreas P. Schnyder, and Leslie M. Schoop. On the possibility of magnetic weyl fermions in non-symmorphic compound ptfesb. *The European Physical Journal B*, 91(10):213, Oct 2018.

[112] Leslie M. Schoop, Andreas Topp, Judith Lippmann, Fabio Orlandi, Lukas Müchler, Maia G. Vergniory, Yan Sun, Andreas W. Rost, Viola Duppel, Maxim Krivenkov, Shweta Sheoran, Pascal Manuel, Andrei Varykhalov, Binghai Yan, Reinhard K. Kremer, Christian R. Ast, and Bettina V. Lotsch. Tunable weyl and dirac states in the nonsymmorphic compound cesbte. *Science Advances*, 4(2):eaar2317, 2018.

[113] Ching-Kai Chiu and Andreas P. Schnyder. Classification of reflection-symmetry-protected topological semimetals and nodal superconductors. *Phys. Rev. B*, 90:205136, Nov 2014.

[114] Bohm-Jung Yang, Troels Arnfred Bojesen, Takahiro Morimoto, and Akira Furusaki. Topological semimetals protected by off-centered symmetries in nonsymmorphic crystals. *Phys. Rev. B*, 95:075135, Feb 2017.

[115] Guang Bian, Tay-Rong Chang, Raman Sankar, Su-Yang Xu, Hao Zheng, Titus Neupert, Ching-Kai Chiu, Shin-Ming Huang, Guoqing Chang, Ilya Belopolski, Daniel S. Sanchez, Madhab Neupane, Nasser Alidoust, Chang Liu, BaoKai Wang, Chi-Cheng Lee, Horng-Tay Jeng, Arun Bansil, Fangcheng Chou, Hsin Lin, and M. Zahid Hasan. Topological Nodal-Line Fermions in the Non-Centrosymmetric Superconductor Compound PbTaSe2. *arXiv e-prints*, page arXiv:1505.03069, May 2015.

[116] Ai Yamakage, Youichi Yamakawa, Yukio Tanaka, and Yoshihiko Okamoto. Line-node dirac semimetal and topological insulating phase in noncentrosymmetric pnictides caagx (x = p, as). *Journal of the Physical Society of Japan*, 85(1):013708, 2016.

[117] Lilia S. Xie, Leslie M. Schoop, Elizabeth M. Seibel, Quinn D. Gibson, Weiwei Xie, and Robert J. Cava. A new form of ca3p2 with a ring of dirac nodes. *APL Materials*, 3(8):083602, 2015.

[118] Youngkuk Kim, Benjamin J. Wieder, C. L. Kane, and Andrew M. Rappe. Dirac line nodes in inversion-symmetric crystals. *Phys. Rev. Lett.*, 115:036806, Jul 2015.

[119] Minggang Zeng, Chen Fang, Guoqing Chang, Yu-An Chen, Timothy Hsieh, Arun Bansil, Hsin Lin, and Liang Fu. Topological semimetals and topological insulators in rare earth monopnictides. *arXiv e-prints*, page arXiv:1504.03492, April 2015.

[120] Huaqing Huang, Jianpeng Liu, David Vanderbilt, and Wenhui Duan. Topological nodal-line semimetals in alkaline-earth stannides, germanides, and silicides. *Phys. Rev. B*, 93:201114, May 2016.

[121] Chen Fang, Yige Chen, Hae-Young Kee, and Liang Fu. Topological nodal line semimetals with and without spin-orbital coupling. *Phys. Rev. B*, 92:081201, Aug 2015.

[122] Guang Bian, Tay-Rong Chang, Hao Zheng, Saavanth Velury, Su-Yang Xu, Titus Neupert, Ching-Kai Chiu, Shin-Ming Huang, Daniel S. Sanchez, Ilya Belopolski, Nasser Alidoust, Peng-Jen Chen, Guoqing Chang, Arun Bansil, Horng-Tay Jeng, Hsin Lin, and M. Zahid Hasan. Drumhead surface states and topological nodal-line fermions in $TlTaSe_2$. *PRB*, 93(12):121113, March 2016.

[123] Hongming Weng, Yunye Liang, Qiunan Xu, Rui Yu, Zhong Fang, Xi Dai, and Yoshiyuki Kawazoe. Topological node-line semimetal in three-dimensional graphene networks. *Phys. Rev. B*, 92:045108, Jul 2015.

[124] Rui Yu, Hongming Weng, Zhong Fang, Xi Dai, and Xiao Hu. Topological node-line semimetal and dirac semimetal state in antiperovskite cu_3PdN. *Phys. Rev. Lett.*, 115:036807, Jul 2015.

[125] Lukas Muechler, Andreas Topp, Raquel Queiroz, Maxim Krivenkov, Andrei Varykhalov, Jennifer Cano, Christian R. Ast, and Leslie M. Schoop. Modular arithmetic with nodal lines: Drumhead surface states in zrsite. *Phys. Rev. X*, 10:011026, Feb 2020.

[126] Guang Bian, Tay-Rong Chang, Raman Sankar, Su-Yang Xu, Hao Zheng, Titus Neupert, Ching-Kai Chiu, Shin-Ming Huang, Guoqing Chang, Ilya Belopolski, Daniel S. Sanchez, Madhab Neupane, Nasser Alidoust, Chang Liu, BaoKai Wang, Chi-Cheng Lee, Horng-Tay Jeng, Chenglong Zhang, Zhujun Yuan, Shuang Jia, Arun Bansil, Fangcheng Chou, Hsin Lin, and M. Zahid Hasan. Topological nodal-line fermions in spin-orbit metal pbtase2. *Nature Communications*, 7(1):10556, Feb 2016.

[127] Wenjie Hou, Jian Liu, Xi Zuo, Jian Xu, Xueying Zhang, Desheng Liu, Mingwen Zhao, Zhen-Gang Zhu, Hong-Gang Luo, and Weisheng Zhao. Prediction of crossing nodal-lines and large intrinsic spin hall conductivity in topological dirac semimetal ta3as family. *npj Computational Materials*, 7(1):37, Mar 2021.

[128] Marc A. Wilde, Matthias Dodenhöft, Arthur Niedermayr, Andreas Bauer, Moritz M. Hirschmann, Kirill Alpin, Andreas P. Schnyder, and Christian Pfleiderer. Symmetry-enforced topological nodal planes at the fermi surface of a chiral magnet. *Nature*, 594(7863):374–379, Jun 2021.

[129] Meng Xiao, Liping Ye, Chunyin Qiu, Hailong He, Zhengyou Liu, and Shanhui Fan. Experimental demonstration of acoustic semimetal with topologically charged nodal surface. *Science Advances*, 6(8), 2020.

[130] Po-Feng Wu, jen-Bin Shi, Bo Cheng, Hsien Lin, and Hsuan Lee. Preparation of large-scale cos2 nanowires and their raman study. *Materials Science Forum*, 947:91–95, 03 2019.

[131] F. Paul. Cattierite and vaesite: New co-ni minerals from the belgian congo. *American Mineralogist*, 30:483–497, 1945.

[132] BT Matthias, AM Clogston, HJ Williams, E Corenzwit, and RC Sherwood. Ferromagnetism in solid solutions of scandium and indium. *Physical Review Letters*, 7(1):7, 1961.

[133] BT Matthias and RM Bozorth. Ferromagnetism of a zirconium-zinc compound. *Physical Review*, 109(2):604, 1958.

[134] S. K. Kwon, S. J. Youn, and B. I. Min. Itinerant ferromagnetism in half-metallic cos2. *Phys. Rev. B*, 62:357–360, Jul 2000.

[135] Peng Li, Weikang Wu, Yan Wen, Chenhui Zhang, Junwei Zhang, Senfu Zhang, Zhiming Yu, Shengyuan A. Yang, A. Manchon, and Xi-xiang Zhang. Spin-momentum locking and spin-orbit torques in magnetic nano-heterojunctions composed of weyl semimetal wte2. *Nature Communications*, 9(1):3990, Sep 2018.

[136] Z. K. Liu, J. Jiang, B. Zhou, Z. J. Wang, Y. Zhang, H. M. Weng, D. Prabhakaran, S.-K. Mo, H. Peng, P. Dudin, T. Kim, M. Hoesch, Z. Fang, X. Dai, Z. X. Shen, D. L. Feng, Z. Hussain, and Y. L. Chen. A stable three-dimensional topological dirac semimetal cd3as2. *Nature Materials*, 13(7):677–681, Jul 2014.

[137] Jason F. Khoury, Alexander J. E. Rettie, Iñigo Robredo, Matthew J. Krogstad, Christos D. Malliakas, Aitor Bergara, Maia G. Vergniory, Raymond Osborn, Stephan Rosenkranz, Duck Young Chung, and Mercouri G. Kanatzidis. The subchalcogenides ir2in8q (q = s, se, te): Dirac semimetal candidates with re-entrant structural modulation. *Journal of the American Chemical Society*, 142(13):6312–6323, Apr 2020.

[138] Z. K. Liu, B. Zhou, Y. Zhang, Z. J. Wang, H. M. Weng, D. Prabhakaran, S.-K. Mo, Z. X. Shen, Z. Fang, X. Dai, Z. Hussain, and Y. L. Chen. Discovery of a three-dimensional topological dirac semimetal, na3bi. *Science*, 343(6173):864–867, 2014.

[139] Gang Xu, Hongming Weng, Zhijun Wang, Xi Dai, and Zhong Fang. Chern semimetal and the quantized anomalous hall effect in $hgcr_2se_4$. *Phys. Rev. Lett.*, 107:186806, Oct 2011.

[140] Hongming Weng, Chen Fang, Zhong Fang, and Xi Dai. Coexistence of weyl fermion and massless triply degenerate nodal points. *Phys. Rev. B*, 94:165201, Oct 2016.

[141] Binghai Yan and Claudia Felser. Topological materials: Weyl semimetals. *Annual Review of Condensed Matter Physics*, 8(1):337–354, 2017.

[142] Su-Yang Xu, Ilya Belopolski, Nasser Alidoust, Madhab Neupane, Guang Bian, Chenglong Zhang, Raman Sankar, Guoqing Chang, Zhujun Yuan, Chi-Cheng Lee, Shin-Ming Huang, Hao Zheng, Jie Ma, Daniel S. Sanchez, BaoKai Wang, Arun Bansil, Fangcheng Chou, Pavel P. Shibayev, Hsin Lin, Shuang Jia, and M. Zahid Hasan. Discovery of a weyl fermion semimetal and topological fermi arcs. *Science*, 349(6248):613–617, 2015.

[143] B. Q. Lv, H. M. Weng, B. B. Fu, X. P. Wang, H. Miao, J. Ma, P. Richard, X. C. Huang, L. X. Zhao, G. F. Chen, Z. Fang, X. Dai, T. Qian, and H. Ding. Experimental discovery of weyl semimetal taas. *Phys. Rev. X*, 5:031013, Jul 2015.

[144] Hongming Weng, Chen Fang, Zhong Fang, B. Andrei Bernevig, and Xi Dai. Weyl semimetal phase in noncentrosymmetric transition-metal monophosphides. *Phys. Rev. X*, 5:011029, Mar 2015.

[145] Xiangang Wan, Ari M. Turner, Ashvin Vishwanath, and Sergey Y. Savrasov. Topological semimetal and fermi-arc surface states in the electronic structure of pyrochlore iridates. *Phys. Rev. B*, 83:205101, May 2011.

[146] Qi-Feng Liang, Jian Zhou, Rui Yu, Zhi Wang, and Hongming Weng. Node-surface and node-line fermions from nonsymmorphic lattice symmetries. *Phys. Rev. B*, 93:085427, Feb 2016.

[147] Tomáš Bzdušek, QuanSheng Wu, Andreas Rüegg, Manfred Sigrist, and Alexey A. Soluyanov. Nodal-chain metals. *Nature*, 538(7623):75–78, Oct 2016.

[148] Qiunan Xu, Rui Yu, Zhong Fang, Xi Dai, and Hongming Weng. Topological nodal line semimetals in the cap3 family of materials. *Phys. Rev. B*, 95:045136, Jan 2017.

[149] Chen Fang, Hongming Weng, Xi Dai, and Zhong Fang. Topological nodal line semimetals. *Chinese Physics B*, 25(11):117106, nov 2016.

[150] Jianzhou Zhao, Rui Yu, Hongming Weng, and Zhong Fang. Topological node-line semimetal in compressed black phosphorus. *PRB*, 94(19):195104, November 2016.

[151] Y.-H. Chan, Ching-Kai Chiu, M. Y. Chou, and Andreas P. Schnyder. ca_3p_2 and other topological semimetals with line nodes and drumhead surface states. *Phys. Rev. B*, 93:205132, May 2016.

[152] Ronghan Li, Hui Ma, Xiyue Cheng, Shoulong Wang, Dianzhong Li, Zhengyu Zhang, Yiyi Li, and Xing-Qiu Chen. Dirac node lines in pure alkali earth metals. *Phys. Rev. Lett.*, 117:096401, Aug 2016.

[153] Motoaki Hirayama, Ryo Okugawa, Takashi Miyake, and Shuichi Murakami. Topological dirac nodal lines and surface charges in fcc alkaline earth metals. *Nature Communications*, 8(1):14022, Jan 2017.

[154] Chen Fang, Yige Chen, Hae-Young Kee, and Liang Fu. Topological nodal line semimetals with and without spin-orbital coupling. *Phys. Rev. B*, 92:081201, Aug 2015.

[155] Syôhei Miyahara and Teruo Teranishi. Magnetic properties of fes2 and cos2. *Journal of Applied Physics*, 39(2):896–897, 1968.

[156] A Teruya, F Suzuki, D Aoki, F Honda, A Nakamura, M Nakashima, Y Amako, H Harima, K Uchima, M Hedo, T Nakama, and Y Ōnuki. Fermi surface and magnetic properties in ferromagnet CoS2and paramagnet CoSe2with the pyrite-type cubic structure. *Journal of Physics: Conference Series*, 807:012001, apr 2017.

[157] P J Brown, K-U Neumann, A Simon, F Ueno, and K R A Ziebeck. Magnetization distribution in CoS2 is it a half metallic ferromagnet? *Journal of Physics: Condensed Matter*, 17(10):1583–1592, feb 2005.

[158] QuanSheng Wu, ShengNan Zhang, Hai-Feng Song, Matthias Troyer, and Alexey A. Soluyanov. Wanniertools : An open-source software package for novel topological materials. *Computer Physics Communications*, 224:405 – 416, 2018.

[159] Ivan I. Naumov and Russell J. Hemley. Topological surface states in dense solid hydrogen. *Phys. Rev. Lett.*, 117:206403, Nov 2016.

[160] M P Lopez Sancho, J M Lopez Sancho, J M L Sancho, and J Rubio. Highly convergent schemes for the calculation of bulk and surface green functions. *Journal of Physics F: Metal Physics*, 15(4):851–858, apr 1985.

[161] Fernando de Juan, Adolfo G. Grushin, Takahiro Morimoto, and Joel E. Moore. Quantized circular photogalvanic effect in weyl semimetals. *Nature Communications*, 8(1):15995, Jul 2017.

[162] Qun Yang, Guowei Li, Kaustuv Manna, Fengren Fan, Claudia Felser, and Yan Sun. Topological engineering of pt-group-metal-based chiral crystals

toward high-efficiency hydrogen evolution catalysts. *Advanced Materials*, 32(14):1908518, 2020.

[163] Guowei Li and Claudia Felser. Heterogeneous catalysis at the surface of topological materials. *Applied Physics Letters*, 116(7):070501, 2020.

[164] Iñigo Robredo, Pranav Rao, Fernando de Juan, Aitor Bergara, Juan L. Mañes, Alberto Cortijo, M. G. Vergniory, and Barry Bradlyn. A new cubic hall viscosity in three-dimensional topological semimetals, 2021.

[165] F Delahaye and B Jeckelmann. Revised technical guidelines for reliable dc measurements of the quantized hall resistance. *Metrologia*, 40(5):217–223, sep 2003.

[166] F. Schopfer and W. Poirier. Testing universality of the quantum hall effect by means of the wheatstone bridge. *Journal of Applied Physics*, 102(5):054903, 2007.

[167] Taylor L. Hughes, Robert G. Leigh, and Onkar Parrikar. Torsional anomalies, hall viscosity, and bulk-boundary correspondence in topological states. *Phys. Rev. D*, 88:025040, Jul 2013.

[168] N Read. Non-abelian adiabatic statistics and hall viscosity in quantum hall states and p x+ i p y paired superfluids. *Physical Review B*, 79(4):045308, 2009.

[169] N Read and EH Rezayi. Hall viscosity, orbital spin, and geometry: paired superfluids and quantum hall systems. *Physical Review B*, 84(8):085316, 2011.

[170] J E Avron, R Seiler, and P G Zograf. Viscosity of quantum hall fluids. *Phys Rev Lett*, 75(4):697–700, Jan 1995.

[171] Péter Lévay. Berry phases for Landau Hamiltonians on deformed tori. *J. Math. Phys.*, 36(6):2792, 1995.

[172] I. V Tokatly and G Vignale. Lorentz shear modulus of a two-dimensional electron gas at high magnetic field. *Phys Rev B*, 76(16):161305, Jan 2007.

[173] F. D. M. Haldane. " hall viscosity" and intrinsic metric of incompressible fractional hall fluids. *arXiv preprint arXiv:0906.1854*, 2009.

[174] F. D. M. Haldane. Geometrical description of the fractional quantum hall effect. *Physical review letters*, 107(11):116801, 2011.

[175] Barry Bradlyn, Moshe Goldstein, and N Read. Kubo formulas for viscosity: Hall viscosity, ward identities, and the relation with conductivity. *Physical Review B*, 86(24):245309, 2012.

[176] Pranav Rao and Barry Bradlyn. Hall viscosity in quantum systems with discrete symmetry: point group and lattice anisotropy. *Physical Review X*, 10(2):021005, 2020.

[177] Luca V Delacrétaz and Andrey Gromov. Transport signatures of the hall viscosity. *Physical review letters*, 119(22):226602, 2017.

[178] Thomas Scaffidi, Nabhanila Nandi, Burkhard Schmidt, Andrew P Mackenzie, and Joel E Moore. Hydrodynamic electron flow and hall viscosity. *Physical review letters*, 118(22):226601, 2017.

[179] Tobias Holder, Raquel Queiroz, and Ady Stern. Unified description of the classical hall viscosity. *arXiv preprint arXiv:1903.05541*, 2019.

[180] Francesco MD Pellegrino, Iacopo Torre, and Marco Polini. Nonlocal transport and the hall viscosity of two-dimensional hydrodynamic electron liquids. *Physical Review B*, 96(19):195401, 2017.

[181] Alexey I Berdyugin, SG Xu, FMD Pellegrino, R Krishna Kumar, Alessandro Principi, Iacopo Torre, M Ben Shalom, Takashi Taniguchi, Kenji Watanabe, IV Grigorieva, et al. Measuring hall viscosity of graphene's electron fluid. *Science*, 364(6436):162–165, 2019.

[182] Debarghya Banerjee, Anton Souslov, Alexander G Abanov, and Vincenzo Vitelli. Odd viscosity in chiral active fluids. *Nature Communications*, 8(1):1573, 2017.

[183] Vishal Soni, Ephraim S Bililign, Sofia Magkiriadou, Stefano Sacanna, Denis Bartolo, Michael J Shelley, and William TM Irvine. The odd free surface flows of a colloidal chiral fluid. *Nature Physics*, 15(11):1188–1194, 2019.

[184] J E Avron. Odd viscosity. *J Stat Phys*, 92(3-4):543–557, Jan 1998.

[185] Hassan Shapourian, Taylor L Hughes, and Shinsei Ryu. Viscoelastic response of topological tight-binding models in two and three dimensions. *Physical Review B*, 92(16):165131, 2015.

[186] Andrey Gromov, Scott D Geraedts, and Barry Bradlyn. Investigating anisotropic quantum hall states with bimetric geometry. *Physical review letters*, 119(14):146602, 2017.

[187] Maissam Barkeshli, Suk Bum Chung, and Xiao-Liang Qi. Dissipationless phonon hall viscosity. *Physical Review B*, 85(24):245107, 2012.

[188] Yunchao Zhang, Yanting Teng, Rhine Samajdar, Subir Sachdev, and Mathias S Scheurer. Phonon hall viscosity from phonon-spinon interactions. *arXiv preprint arXiv:2103.05650*, 2021.

[189] Haoyu Guo and Subir Sachdev. Extrinsic phonon thermal hall transport from hall viscosity. *Physical Review B*, 103(20):205115, 2021.

[190] Mengxing Ye, Rafael M Fernandes, and Natalia B Perkins. Phonon dynamics in the kitaev spin liquid. *Physical Review Research*, 2(3):033180, 2020.

[191] Mengxing Ye, Lucile Savary, and Leon Balents. Phonon hall viscosity in magnetic insulators. *arXiv preprint arXiv:2103.04223*, 2021.

[192] J Gooth, F Menges, N Kumar, V Süβ, C Shekhar, Y Sun, U Drechsler, R Zierold, C Felser, and B Gotsmann. Thermal and electrical signatures of a hydrodynamic electron fluid in tungsten diphosphide. *Nature communications*, 9(1):1–8, 2018.

[193] Jennifer Cano, Barry Bradlyn, and MG Vergniory. Multifold nodal points in magnetic materials. *APL Materials*, 7(10):101125, 2019.

[194] Bendeguz Offertaler and Barry Bradlyn. Viscoelastic response of quantum hall fluids in a tilted field. *Physical Review B*, 99(3):035427, 2019.

[195] Christian Copetti and Karl Landsteiner. Anomalous hall viscosity at the weyl-semimetal–insulator transition. *Physical Review B*, 99(19):195146, 2019.

[196] Georgios Varnavides, Adam S Jermyn, Polina Anikeeva, Claudia Felser, and Prineha Narang. Electron hydrodynamics in anisotropic materials. *Nature communications*, 11(1):1–6, 2020.

[197] Vicente Arjona and María A. H. Vozmediano. Rotational strain in weyl semimetals: A continuum approach. *Phys. Rev. B*, 97:201404, May 2018.

[198] Karl Landsteiner, Yan Liu, and Ya-Wen Sun. Odd viscosity in the quantum critical region of a holographic weyl semimetal. *Phys. Rev. Lett.*, 117:081604, Aug 2016.

[199] Alberto Cortijo, Yago Ferreirós, Karl Landsteiner, and María AH Vozmediano. Elastic gauge fields in weyl semimetals. *Physical review letters*, 115(17):177202, 2015.

[200] Tomer Markovich and Tom C Lubensky. Odd viscosity in active matter: microscopic origin and 3d effects. *arXiv preprint arXiv:2006.05662*, 2020.

[201] Onkar Parrikar, Taylor L Hughes, and Robert G Leigh. Torsion, parity-odd response, and anomalies in topological states. *Physical Review D*, 90(10):105004, 2014.

[202] Juan L Manes. Existence of bulk chiral fermions and crystal symmetry. *Physical Review B*, 85(15):155118, 2012.

[203] Guoqing Chang, Benjamin J Wieder, Frank Schindler, Daniel S Sanchez, Ilya Belopolski, Shin-Ming Huang, Bahadur Singh, Di Wu, Tay-Rong Chang, Titus Neupert, et al. Topological quantum properties of chiral crystals. *Nature materials*, 17(11):978–985, 2018.

[204] Felix Flicker, Fernando De Juan, Barry Bradlyn, Takahiro Morimoto, Maia G Vergniory, and Adolfo G Grushin. Chiral optical response of multifold fermions. *Physical Review B*, 98(15):155145, 2018.

[205] Guoqing Chang, Su-Yang Xu, Benjamin J Wieder, Daniel S Sanchez, Shin-Ming Huang, Ilya Belopolski, Tay-Rong Chang, Songtian Zhang, Arun Bansil, Hsin Lin, et al. Unconventional chiral fermions and large topological fermi arcs in rhsi. *Physical review letters*, 119(20):206401, 2017.

[206] Daniel S Sanchez, Ilya Belopolski, Tyler A Cochran, Xitong Xu, Jia-Xin Yin, Guoqing Chang, Weiwei Xie, Kaustuv Manna, Vicky Süß, Cheng-Yi Huang, et al. Topological chiral crystals with helicoid-arc quantum states. *Nature*, 567(7749):500–505, 2019.

[207] Zhicheng Rao, Hang Li, Tiantian Zhang, Shangjie Tian, Chenghe Li, Binbin Fu, Cenyao Tang, Le Wang, Zhilin Li, Wenhui Fan, et al. Observation of unconventional chiral fermions with long fermi arcs in cosi. *Nature*, 567(7749):496–499, 2019.

[208] Niels BM Schröter, Ding Pei, Maia G Vergniory, Yan Sun, Kaustuv Manna, Fernando De Juan, Jonas A Krieger, Vicky Süss, Marcus Schmidt, Pavel Dudin, et al. Chiral topological semimetal with multifold band crossings and long fermi arcs. *Nature Physics*, 15(8):759–765, 2019.

[209] Niels BM Schröter, Samuel Stolz, Kaustuv Manna, Fernando De Juan, Maia G Vergniory, Jonas A Krieger, Ding Pei, Thorsten Schmitt, Pavel Dudin, Timur K Kim, et al. Observation and control of maximal chern numbers in a chiral topological semimetal. *Science*, 369(6500):179–183, 2020.

[210] Dylan Rees, Kaustuv Manna, Baozhu Lu, Takahiro Morimoto, Horst Borrmann, Claudia Felser, JE Moore, Darius H Torchinsky, and J Orenstein. Observation of topological photocurrents in the chiral weyl semimetal rhsi. *arXiv preprint arXiv:1902.03230*, 2019.

[211] Zhuoliang Ni, B. Xu, M.-A. Sánchez-Martínez, Y. Zhang, K. Manna, C. Bernhard, J. W. F. Venderbos, F. de Juan, C. Felser, A. G. Grushin, and et al. Linear and nonlinear optical responses in the chiral multifold semimetal rhsi. *npj Quantum Materials*, 5(1), Dec 2020.

[212] Zhuoliang Ni, K. Wang, Y. Zhang, O. Pozo, B. Xu, X. Han, K. Manna, J. Paglione, C. Felser, A. G. Grushin, and et al. Giant topological longitudinal circular photo-galvanic effect in the chiral multifold semimetal cosi. *Nature Communications*, 12(1), Jan 2021.

[213] Shiva Heidari, Alberto Cortijo, and Reza Asgari. Hall viscosity for optical phonons. *Physical Review B*, 100(16):165427, 2019.

[214] Alberto Cortijo, Yago Ferreirós, Karl Landsteiner, and María AH Vozmediano. Visco elasticity in 2d materials. *2D Materials*, 3(1):011002, 2016.

[215] Therese Eriksson, Solveig Felton, Raquel Lizárraga, Olle Eriksson, Per Nordblad, and Yvonne Andersson. Crystal structure and magnetic properties of the new phase mn3irsi. *Journal of Magnetism and Magnetic Materials*, 272-276:823 – 825, 2004. Proceedings of the International Conference on Magnetism (ICM 2003).

[216] T. Eriksson, R. Lizárraga, S. Felton, L. Bergqvist, Y. Andersson, P. Nordblad, and O. Eriksson. Crystal and magnetic structure of mn_3IrSi. *Phys. Rev. B*, 69:054422, Feb 2004.

[217] A. Abanov and A. Gromov. *Phys. Rev. B*, 90:014435, 2014.

[218] Dieter Forster. Hydrodynamic fluctuations, broken symmetry, and correlation functions. In *Reading, Mass., WA Benjamin, Inc.(Frontiers in Physics. Volume 47), 1975. 343 p.*, volume 47, 1975.

[219] Alexander G Abanov and Gustavo M Monteiro. Free-surface variational principle for an incompressible fluid with odd viscosity. *Physical review letters*, 122(15):154501, 2019.

[220] Taiki Matsushita, Satoshi Fujimoto, and Andreas P Schnyder. Topological piezoelectric effect and parity anomaly in nodal line semimetals. *arXiv preprint arXiv:2002.11666*, 2020.

[221] J. L. Mañes, F. de Juan, M. Sturla, and M. A. H. Vozmediano. Generalized effective Hamiltonian for graphene under nonuniform strain. *Phys. Rev. B*, 88(15):155405, October 2013.

[222] Julia M Link, Daniel E Sheehy, Boris N Narozhny, and Jörg Schmalian. Elastic response of the electron fluid in intrinsic graphene: The collisionless regime. *Physical Review B*, 98(19):195103, 2018.

[223] Frederik J Belinfante. On the current and the density of the electric charge, the energy, the linear momentum and the angular momentum of arbitrary fields. *Physica*, 7(5):449–474, 1940.

[224] Taylor L Hughes, Robert G Leigh, and Eduardo Fradkin. Torsional response and dissipationless viscosity in topological insulators. *Physical review letters*, 107(7):075502, 2011.

[225] Joseph A Sulpizio, Lior Ella, Asaf Rozen, John Birkbeck, David J Perello, Debarghya Dutta, Moshe Ben-Shalom, Takashi Taniguchi, Kenji Watanabe, Tobias Holder, et al. Visualizing poiseuille flow of hydrodynamic electrons. *Nature*, 576(7785):75–79, 2019.

[226] C. Hoyos and D. T. Son. *Phys. Rev. Lett.*, 108:066805, 2012.

[227] Vladyslav Kozii, Alexander Avdoshkin, Shudan Zhong, and Joel E. Moore. Intrinsic anomalous hall conductivity in a nonuniform electric field. *Phys. Rev. Lett.*, 126:156602, Apr 2021.

[228] Igor S Burmistrov, Moshe Goldstein, Mordecai Kot, Vladislav D Kurilovich, and Pavel D Kurilovich. Dissipative and hall viscosity of a disordered 2d electron gas. *Physical review letters*, 123(2):026804, 2019.

[229] Yuanfeng Xu, Luis Elcoro, Zhi-Da Song, Benjamin J. Wieder, M. G. Vergniory, Nicolas Regnault, Yulin Chen, Claudia Felser, and B. Andrei Bernevig. High-throughput calculations of magnetic topological materials. *Nature*, 586(7831):702–707, Oct 2020.

[230] P. Burlet, E. Ressouche, B. Malaman, R. Welter, J. P. Sanchez, and P. Vulliet. Noncollinear magnetic structure of $mnte_2$. *Phys. Rev. B*, 56:14013–14018, Dec 1997.

[231] Yidong Xu, Wen Li, Chen Wang, Zhiwei Chen, Yixuan Wu, Xinyue Zhang, Juan Li, Siqi Lin, Yue Chen, and Yanzhong Pei. Mnte2 as a novel promising thermoelectric material. *Journal of Materiomics*, 4(3):215 – 220, 2018.